Quantum Computation in Large Ion Crystals

by

Yukai Wu

A dissertation submitted in partial fulfillment
of the requirements for the degree of
Doctor of Philosophy
(Physics)
in the University of Michigan
2019

Doctoral Committee:

Associate Professor Hui Deng, Co-Chair
Professor Luming Duan, Co-Chair
Professor Alex Kuzmich
Professor John Carl Schotland
Associate Professor Kai Sun

Yukai Wu

wyukai@umich.edu

ORCID iD: 0000-0003-2184-7553

To my family

ACKNOWLEDGMENTS

When writing this thesis to summarize my graduate studies, I could not help but recalling my experience over the past four years. Many people have helped me in my research, directly or indirectly, without whom the work presented here would never be possible. Here I would like to take this opportunity to thank everyone.

First of all, I want to thank my advisor, Luming Duan. I first heard Luming's name in the news and from my classmates during my undergrad study at Tsinghua University, where Luming held an honorary professorship. I still remember when I was admitted to University of Michigan and first met with Luming before I came here, he asked me what I was interested in for the graduate study, and I said I wanted to learn as much as I could about quantum computing and its physical implementation. This ambition clearly sounds unrealistic, but thanks to Luming, I got the chance to at least try to pursue it. Although this thesis will focus on ion trap quantum computing, I also got involved in other projects about superconducting circuits, NV centers and ultra-cold atoms through Luming's connections. What surprises me the most about Luming during these years is his deep understanding in all these fields, among others, both theoretically and experimentally.

I want to thank all the students in Luming's group at Michigan. Sheng-Tao Wang is the one who guided me through the basics about ion trap quantum computing. He also helped me

to revise my first paper over and over again to improve my academic writing. Even after his graduation, he is still willing to answer my questions and share his experience in preparing the thesis. I am also grateful to the helpful discussions with Tanvi Gujarati, Zhengyu Zhang and Ceren Burcak Dag. Although Luming does not hold regular group meeting here because every student is working on different fields, we have our informal group meeting (and group lunch) where we introduce to each other the basics of our projects or other interesting topics.

Since Luming is constantly travelling between Michigan and Tsinghua, I also get the chance to visit Institute for Interdisciplinary Information Sciences (IIIS), Tsinghua University every summer, not only to continue my friendship with my undergrad classmates but also to develop new collaborations with the students and the professors there. I benefitted a lot from my discussion with Xun Gao on complexity theory, machine learning and other topics beyond physics, with Dong-Ling Deng on quantum machine learning, and with Yong Xu on ultra-cold atoms and topological condensed matter; I also enjoyed the time when we played table tennis together at the FIT building. I would like to thank Kihwan Kim for showing me around his ion trap lab and many helpful discussions on various kinds of experimental noise, Sirui Lu on random unitaries, Xiang Zhang on the numerical calculation of the electric potentials in a real trap and the ions' motions in it, and Zidu Liu and Wending Zhao for testing and verifying many of my programme codes. I am also grateful to Yunfei Pu for discussions on ultra-cold atoms, Yuanyuan Huang and Wengang Zhang on NV centers, Hongyi Zhang on P1 centers and superconducting qubits, and Luyan Sun and Weiting Wang on superconducting qubits and cavities. Besides, I am very thankful to Liyuan Qiu for inviting me to many of the group activities like the meals, badminton and billiards. Finally I want to thank Yuying Chang and Yu Fang for arranging the accommodation and all the administrative work for my visit.

Also through Luming's connections, I got in touch with many researchers in the field of ion trap and quantum computing. I would like to thank Yaoyun Shi and his students, Kevin J. Sung, Cupjin Huang and Michael Newman for sharing their expertise in quantum algorithms and error corrections; I also want to thank Jiehang Zhang, Guido Pagano and Kevin Landsman from Chris Monroe's group for many useful discussions on ion trap experiments. My collaboration with Kenneth R. Brown and his student Colin J. Trout also started in this way, and then as Mike joined his group in Duke as a postdoc, I was lucky to be invited for a visit. I enjoyed my discussions with Pak Hong (James) Leung, Leonardo Andreta de Castro and Jungsang Kim during my stay and was surprised by how closely our research topics are related. I would also like to thank the visitors to our group at Michigan, Yong Wan and Mingxing Luo, for many helpful discussions.

Much work covered in this thesis is supported by the IARPA Logic Qubit program. I also want to thank the organizers and all the participants of the Boulder Summer School 2018 where I met many researchers in the field of quantum computation and quantum information, made new friends, and benefitted from the lectures and discussions.

Last but not least, I would like to thank my family. I could not have done any of this work without their constant and unconditional love and support. They are the best thing in my life.

TABLE OF CONTENTS

LIST OF FIGURES

LIST OF TABLES

ABSTRACT

Ion trap is one of the most promising candidates for quantum computing. High-fidelity gates have been demonstrated in small ion crystals and schemes like ion shuttling have been proposed for larger systems. This thesis discusses the possibility of direct quantum computing on a large ion crystal in a Paul trap, without any shuttling of the ions. We first review a scheme to entangle two ions in a small ion crystal mediated by the collective phonon modes and analyze the gate errors. The generalization to larger systems is divided into three parts. (1) We present numerical methods to solve all the normal modes of the ion crystal, including the micromotion, up to arbitrary precision. The stability of the crystal under infinitesimal perturbation is ensured when all the normal modes have real frequencies. For finite disturbance, direct molecular dynamics simulation will be needed; after discussing some potential problems in the simulation, we give a rule of thumb for the ion crystal to be stable at a given temperature. (2) We show that when designing an entangling gate between two nearby ions, all the ions far away can be neglected, so that only a small number of normal modes are relevant. Similarly, distant entangling gates can be applied in parallel and the crosstalk is shown to decay cubically with the distance between these gates. (3) Then we present numerical methods to include the solved micromotion into the design of the entangling gates efficiently, again up to arbitrary precision. Thus we conclude that the

design and the implementing of entangling gates are scalable in a large ion crystal. Finally we consider a near-term application to simulate an all-to-all coupled Ising model in a small to medium-sized ion crystal.

Chapter 1

Introduction

Since its birth in the early 20th century, quantum mechanics has dramatically changed various fields of natural science: from interactions of elementary particles in the microscopic level with extraordinary precision, to a wide range of phases of matter and their transitions in the macroscopic level. While deepening our understanding of nature, quantum mechanics has also contributed significantly to the human society. It is the foundation of new materials such as semiconductors and superconductors, and new technologies like laser and nuclear magnetic resonance. Besides, quantum mechanics is fundamentally different in its conception from classical mechanics, through the phenomena such as superposition and entanglement. It is widely believed, although not proven yet, that this fact alone can bring out computational power beyond any machines and protocols based on classical physics. This leads us to the study of quantum computation.

In order to implement quantum computation, we need a physical system which supports some basic quantum operations. These operations include [3, 4]:

1. A high-fidelity universal gate set. A common choice of the universal gate set consists

of single-qubit gates H, S and T, and two-qubit controlled-NOT (CNOT) gate. (See Sec. 1.1 for more details about these gates.)

2. High-fidelity initialization of the qubits to a certain state, say $|0\rangle$.

3. High-fidelity measurement of the qubits in a certain basis, say the computational basis of $|0\rangle$ and $|1\rangle$.

Besides, the qubits must have long coherence time such that multiple quantum operations can be performed before the information is lost. Last but not least, the realization of the qubit register and these operations must be scalable because for realistic problems we will need thousands to millions of high-fidelity logical qubits, each of which may require tens of thousands of faulty physical qubits through the quantum error correction (QEC) process (see e.g. Ref. [5]).

There are many possible candidates as the platform of quantum computing, like trapped ions [6, 7], superconducting circuits [8], NV centers [9], quantum dots [10], anyons in topological systems [11], etc. Each system has its own advantages and disadvantages. For example, superconducting qubits benefit from the mature micro-fabrication technology of chips for classical computers, and they can be designed to have strong coupling with each other and hence short gate time; in comparison, trapped ions have much longer coherence time and gates can be realized at higher fidelity, but also much more slowly. On the other hand, qubits based on anyons, a.k.a. topological qubits, are far more difficult to build; but once it is done, it will have much higher fidelity and hence require much less overhead for error correction.

In this thesis we will focus on the ion trap system, describing the way to realize high-fidelity quantum gates, the scalability, and its potential near-term applications. In particular, we consider the possibility of quantum computing on a large ion crystal using direct laser

control. We will review a scheme for high-fidelity entangling gates in small ion crystals in Chapter 2, and then generalize it to large crystals in Chapter 3. This generalization will be divided into the following three parts. (1) The equilibrium configuration and all the normal modes of the ion crystal, including the micromotion, will be solved up to arbitrary precision. Once we find an equilibrium configuration with all the normal mode frequencies being real, its stability under infinitesimal perturbation is guaranteed; for finite disturbance, direct molecular dynamics simulation will be needed, and we give a rule of thumb for the ion crystal to be stable at a given temperature. (2) We will show that the design of an entangling gate between two nearby ions is insensitive to all the ions far away, so that we only need to consider a small number of normal modes and thus the gate fidelity can be optimized efficiently. Similarly, distant entangling gates can be applied in parallel and the crosstalk is shown to decay cubically with the distance between these gates. (3) Finally numerical methods will be presented to include the solved micromotion into the design of the entangling gates efficiently, again up to arbitrary precision. After discussing the scalability of the scheme, we will go back to small to medium-sized ion crystals in Chapter 4 for a potential near-term application in quantum simulation, using many of the techniques developed in the previous chapters.

In the remaining of this chapter, some background knowledge will be reviewed about quantum computing and about the ion trap.

1.1 Basics about Quantum Computing

The contents of this section and more details can be found in many textbooks, e.g. Ref. [4].

The basic computational unit of a classical computer is a bit, a system consisting of two

distinct states which are often labelled as 0 and 1. Its counterpart in quantum computing is a two-level system called quantum bit (qubit). Mathematically, the (pure) state of a qubit can be represented by a normalized vector in $\mathbb{C}^2$, while that of n qubits by a vector in the tensor-product space $\mathbb{C}^{2n}$. It is often convenient to use Dirac notation to represent a quantum state. For example, a qubit state can be denoted as $|\psi\rangle = \alpha|0\rangle + \beta|1\rangle$, where $|0\rangle$ and $|1\rangle$ are the two basis vectors of $\mathbb{C}^2$ (which is called the computational basis). The Hermitian conjugate of a state vector $|\psi\rangle$ is represented by reversing the bracket $\langle\psi|$; and putting the two notations together we get the regular matrix multiplication, in this case the inner product, $\langle\phi|\psi\rangle$, which is a c-number describing the projection of one state on the other. The tensor product of two qubit states is denoted as $|\psi\rangle_A \otimes |\phi\rangle_B$, where the subscripts A and B label the two qubits; often we omit the $\otimes$ symbol and the subscripts as $|\psi\rangle|\phi\rangle$ while the labels of the qubits can be inferred from their order.

Coherent evolution of the qubit system, a.k.a. quantum gate, is described by unitary operators on the state vectors. In Dirac notation, the effect of a unitary operator U on a state $|\psi\rangle$ is simply denoted by $U|\psi\rangle$. Given a basis, the unitary operator U can be represented in the matrix form, which is often denoted by the same symbol U. Here we show some commonly used unitary operators. For single-qubit gates, we have three Pauli operators

$$\sigma_x = \begin{pmatrix} 0 & 1 \\ 1 & 0 \end{pmatrix}, \qquad \sigma_y = \begin{pmatrix} 0 & -i \\ i & 0 \end{pmatrix}, \qquad \sigma_z = \begin{pmatrix} 1 & 0 \\ 0 & -1 \end{pmatrix}, \tag{1.1}$$

Hadamard gate

$$H = \frac{1}{\sqrt{2}} \begin{pmatrix} 1 & 1 \\ 1 & -1 \end{pmatrix}, \tag{1.2}$$

phase gate

$$S = \begin{pmatrix} 1 & 0 \\ 0 & i \end{pmatrix}, \tag{1.3}$$

and $\pi/8$ gate

$$T = \begin{pmatrix} 1 & 0 \\ 0 & e^{i\pi/4} \end{pmatrix}. \tag{1.4}$$

For two-qubit gates, we have the controlled-NOT (CNOT)

$$\text{CNOT} = \begin{pmatrix} 1 & 0 & 0 & 0 \\ 0 & 1 & 0 & 0 \\ 0 & 0 & 0 & 1 \\ 0 & 0 & 1 & 0 \end{pmatrix}. \tag{1.5}$$

As is mentioned earlier, H, S, T and CNOT form a universal gate set, which means that an arbitrary (multi-qubit) gate can be approximated to arbitrary precision using just these four types of gates (assuming we can apply these gates on any single qubit or any pair of two qubits). For example, we have $\sigma_z = S^2$ and $\sigma_x = H\sigma_z H$. Actually we have $S = T^2$ so we only need H, T and CNOT for the universal gate set. The reason why we include S in the set is that it is relatively easy to implement H, S and CNOT fault-tolerantly, but much more difficult for T gate. (See e.g. Ref. [4] for more details about fault-tolerant quantum computing.) Hence it is preferred to compile the desired gate into H, S and CNOT, and use T gate only when necessary.

In quantum mechanics, observables are represented by Hermitian operators A ($A = A^\dagger$). The possible values of this observable is given by the eigenvalue λ of A: $A|\psi_\lambda\rangle = \lambda|\psi_\lambda\rangle$,

where the corresponding eigenvector $|\psi_\lambda\rangle$ describes the state of the system after the measurement. For quantum computing, usually we consider measurements in the computational basis. Measurements in the other bases can be converted to the computational basis through suitable unitary transformations. For an n-qubit state the probability to measure $|x\rangle \equiv |x_1\rangle|x_2\rangle \cdots |x_n\rangle$ ($x = 0, 1, \cdots, 2^n - 1$ and $x_1 \cdots x_n$ is its binary representation) is given by $|\langle x|\psi\rangle|^2$, and the classical outcome of this measurement is simply the binary string x.

One special and extremely useful example of Hermitian operators is the Hamiltonian H of a system. The eigenvalues of a time-independent Hamiltonian give the possible energy levels; and the evolution of the system over time t is governed by a unitary $U = e^{-iHt}$ if we choose suitable units. For a time-dependent Hamiltonian $H(t)$, the unitary evolution becomes more complex; and usually this is how we implement a quantum gate on the system. We will see some examples in the later chapters.

In reality however, the qubit system is unavoidably interacting with the environment and thus will gradually lose its coherence. Then the state of the system can in general be represented by a density operator (density matrix) $\rho = \sum_i p_i |\psi_i\rangle\langle\psi_i|$, which is a mixture of several pure states (hence it is also called a mixed state) according to a classical probability distribution $\{p_i\}$ with $\sum_i p_i = 1$. By definition, a density matrix is Hermitian and positive semi-definite, and has a trace of 1. Accordingly, the evolution of the system is generally described by a quantum channel, a linear map which converts one density matrix to another. A quantum channel can always be written in the Kraus form $\mathcal{C}(\rho) = \sum_k c_k \rho c_k^\dagger$ where $\{c_k\}$ are linear operators satisfying a normalization condition $\sum_k c_k^\dagger c_k = I$. The probability to find the state ρ in the computational basis state $|x\rangle$ is now $\langle x|\rho|x\rangle$.

Since there are unavoidably errors in the preparation and the evolution of the quantum system, it is desired to have some quantities characterizing the distance between the real

and the ideal state. One common choice in the experiment is fidelity. Suppose the ideal state is a pure state $|\psi\rangle$ and the actual state we get is described by a density matrix ρ, then the fidelity is defined as $F = \langle\psi|\rho|\psi\rangle$, the probability to find ρ in $|\psi\rangle$ in a projection measurement. More generally, for two mixed states ρ and σ, the fidelity is defined as

$$F(\rho, \sigma) = \left(\mathrm{tr}\sqrt{\sqrt{\rho}\sigma\sqrt{\rho}}\right)^2. \tag{1.6}$$

Note that our definition here is different from that in Ref. [4] by a square. Strictly speaking, fidelity is not a distance measure, because it approaches 1 rather than 0 as the two states get closer, but it is widely used in the experiments because of its clear meaning of a probability.

We can also use fidelity to characterize the difference between two quantum channels: given an initial state $|\psi\rangle$, the similarity between two channels $\mathcal{C}_1$ and $\mathcal{C}_2$ can be described by $F(\mathcal{C}_1(|\psi\rangle\langle\psi|), \mathcal{C}_2(|\psi\rangle\langle\psi|))$. This quantity, however, depends on the choice of the initial state. For a state-independent measure, we can average over all possible pure states

$$\overline{F}(\mathcal{C}_1, \mathcal{C}_2) = \int d\psi F(\mathcal{C}_1(|\psi\rangle\langle\psi|), \mathcal{C}_2(|\psi\rangle\langle\psi|)), \tag{1.7}$$

where the integration is over the Fubini-Study measure [12]. For the purpose of quantum computing, we are mainly interested in the closeness between a quantum channel $\mathcal{C}$ and an ideal unitary operator U. In this case we have [13]

$$\overline{F}(\mathcal{C}, U) = \frac{\sum_j \mathrm{tr}[UU_j^\dagger U^\dagger \mathcal{C}(U_j)] + d^2}{d^2(d+1)}, \tag{1.8}$$

where d is the dimension of the system and $\{U_j\}$ is an orthogonal basis for unitary operators of dimension d with the normalization $\mathrm{tr}[U_j^\dagger U_k] = \delta_{jk} d$. For example, if we have n qubits,

then $d = 2^n$ and $\{U_j\}$ can be chosen as the Pauli basis $\{I, \sigma_x, \sigma_y, \sigma_z\}^{\otimes n}$.

As a method to characterize the gate errors, fidelity has the advantage that it is relatively easy to measure in the experiment and also to calculate analytically. However, it underestimates the effects of coherent errors, such as an over-rotation [14]. In this sense another measure, diamond norm, is preferred to describe the distance between two channels [15]:

$$\|\mathcal{C}_1 - \mathcal{C}_2\|_\diamond \equiv \max_{\substack{|\psi\rangle \in \mathcal{H}_S \otimes \mathcal{H}_A \\ \langle\psi|\psi\rangle = 1}} \|(\Delta_S \otimes \mathcal{I}_A)(|\psi\rangle\langle\psi|)\|_1 \tag{1.9}$$

where $\mathcal{H}_S$ is the system Hilbert space which the two channels act on and $\mathcal{H}_A$ is an ancilla Hilbert space which has the same dimension as $\mathcal{H}_S$; $\Delta \equiv \mathcal{C}_1 - \mathcal{C}_2$ is the difference of the two channels and $\mathcal{I}$ is the identity channel on the ancilla A; $\|\cdot\|_1$ is the trace norm, which is defined as the sum of all the singular values of the input argument, i.e. the 1-norm of the eigenvalues. What is special for the diamond norm is that it makes use of entanglement between the system and the ancilla. It is usually difficult to derive an analytical expression for the diamond norm, but given the quantum channels, it can still be computed efficiently through semi-definite programming [16].

1.2 Ion Trap

Ions are charged microscopic particles. Ions of the same species are identical and usually have well-studied level structures. The transitions between these levels can be controlled by laser at very high precision. In order to realize the individual control of the ions as is required for quantum computing, we want to confine and separate the ions in space. This is usually done with a confining electromagnetic field; the ions will then naturally form a

crystal (Wigner crystal) at low temperature due to their Coulomb repulsion. Paul trap is one such method to capture ions with radio-frequency (RF) electric field [17]. It is popular for quantum computing because it can produce a static crystal (with possibly small oscillations around the equilibrium positions which will be specified below) as compared to the Penning trap where ions are constantly rotating [18].

1.2.1 Trapping Potential and Equation of Motion

Earnshaw's theorem tells us that a static electric field in vacuum cannot confine a charged particle in all three directions in space (see e.g. Ref. [19]). Paul trap comes from the idea that if the electric field is oscillating in its directions such that the ions feel alternating focusing and defocusing forces, on average there can be a confining field in all directions.

Near the center of the trap, we can expand the electric potential to the quadratic terms [20]

$$\Phi = \frac{1}{2}\left(\alpha x^2 + \beta y^2 + \gamma z^2\right) U + \frac{1}{2}\left(\alpha' x^2 + \beta' y^2 + \gamma' z^2\right) \tilde{U} \cos \omega_{\mathrm{rf}} t, \tag{1.10}$$

where we assume that the static and the RF fields have their principle axes aligned in the same directions.

Suppose we have N identical ions inside the trap, and the ion has electric charge Ze where $e > 0$ is the elementary charge. Let us define dimensionless parameters

$$a_x = \frac{4ZeU\alpha}{m\omega_{\mathrm{rf}}^2}, \tag{1.11}$$

$$q_x = -\frac{2Ze\tilde{U}\alpha'}{m\omega_{\mathrm{rf}}^2}. \tag{1.12}$$

We further use dimensionless time and spatial coordinates with time unit $T = 2/\omega_{\rm rf}$ and length unit $L = (Z^2e^2/4\pi\epsilon_0 m\omega_{\rm rf}^2)^{1/3}$. Then we get the dimensionless equation of motion (EOM):

$$\frac{d^2x_i}{dt^2} + (a_x - 2q_x\cos 2t)x_i - 4\sum_{j\neq i}\frac{x_i - x_j}{[(x_i-x_j)^2 + (y_i-y_j)^2 + (z_i-z_j)^2]^{\frac{3}{2}}} = 0, \tag{1.13}$$

and similar expressions for y and z directions. Here $i = 1, 2, \cdots, N$ corresponds to each ion. For convenience, we can write these trapping parameters into vector forms: $\boldsymbol{a} = (a_1, a_2, a_3)$ and $\boldsymbol{q} = (q_1, q_2, q_3)$, with the subscript 1, 2, 3 corresponding to the x, y and z directions. Note that the divergence of the trapping electric field is zero, so $\sum_i a_i = 0$ and $\sum_i q_i = 0$.

If $N = 1$ the Coulomb interaction term in the above equation is omitted and we recover the standard form of Mathieu equation [21]. For certain values of a_i and q_i, Mathieu equation has quasi-periodic solutions, which means the trapping in this direction is stable. These conditions together give the stability region of a single ion in the Paul trap. As an example we consider a linear Paul trap with trapping parameters $\boldsymbol{a} = (-a, -a, 2a)$ and $\boldsymbol{q} = (q, -q, 0)$. Its stability region is shown in Fig. 1.1

In the limit of small a and q, the alternating field can be approximated by a static pseudo-potential [22], which has the form of a harmonic trap with trapping frequencies ω_x, ω_y and ω_z. To the lowest order, we have $\omega_i \approx \sqrt{a_i + q_i^2/2}$ [20] with the frequency unit $\omega_{\rm rf}/2$. The equilibrium positions of the ions can then be computed by minimizing the potential energy using for example the Newton's method [23]. When q is not a small parameter, there will be non-negligible oscillations in ions' equilibrium configuration at the RF frequency, a.k.a. micromotion. We will describe how to compute these periodic trajectories as well as the small oscillations around them in Chapter 3.

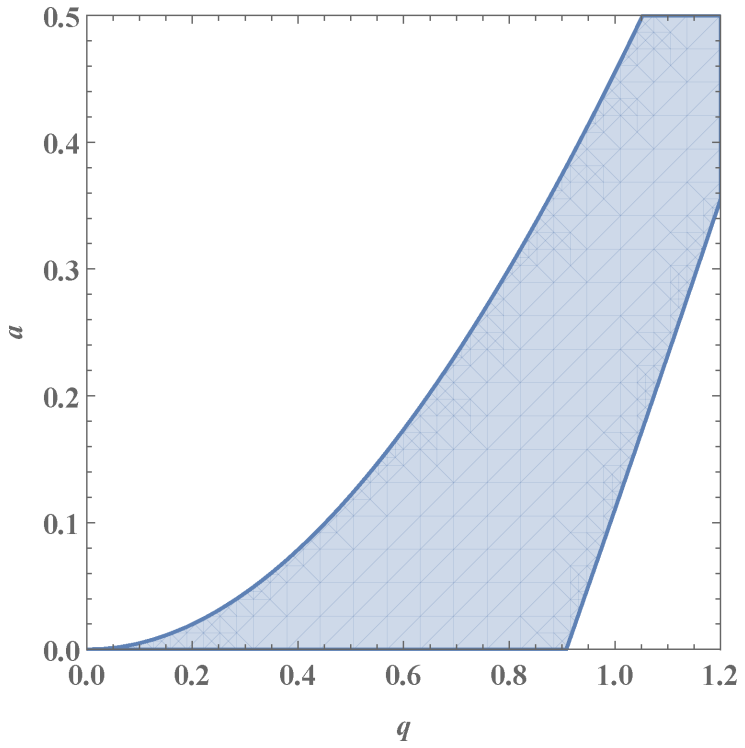

Figure 1.1: Stability region of a single ion in the Paul trap with trapping parameters $\boldsymbol{a} = (-a, -a, 2a)$ and $\boldsymbol{q} = (q, -q, 0)$. The stability region extends to the upper right direction, but for ion trap quantum computing we are mainly interested in the region of $q \ll 1$. Another symmetric region exists for negative q, but a must be positive.

1.2.2 Cooling and Heating

A realistic ion trap has a finite potential depth, hence some cooling mechanism is needed to reduce the kinetic energy of the ions such that they can be held in the trap. It is usually realized by Doppler cooling through a red-detuned laser beam to a cyclic transition of the ion [20]. Consider two levels $|g\rangle$ and $|e\rangle$ of the ion (not necessarily the qubit levels) with a transition frequency $\omega_0 = (E_e - E_g)/\hbar$ and a laser beam with frequency ω and wave vector $\boldsymbol{k}$ in the lab frame. If the ion is moving at the velocity of $\boldsymbol{v}$, the frequency of the laser will be $\omega - \boldsymbol{k} \cdot \boldsymbol{v}$ in the frame of the ion due to the Doppler effect. The Hamiltonian of the ion (in a rotating frame) can be written as [24]

$$H = \hbar \frac{\Delta - \boldsymbol{k} \cdot \boldsymbol{v}}{2} \sigma_z + \hbar \frac{\Omega}{2} \sigma_x, \tag{1.14}$$

where $\Delta \equiv \omega - \omega_0$ is the detuning of the laser and Ω is the Rabi frequency.

Next we include the spontaneous emission of the excited state. The evolution of the density matrix of the ion is now governed by a master equation [25]

$$\dot{\rho} = -\frac{i}{\hbar}[H, \rho] + \frac{\Gamma}{2} \left(2\sigma_- \rho \sigma_+ - \sigma_+ \sigma_- \rho - \rho \sigma_+ \sigma_- \right), \tag{1.15}$$

where Γ describe the spontaneous emission rate, σ_+ converts $|g\rangle$ to $|e\rangle$ and σ_- from $|e\rangle$ to $|g\rangle$. Strictly speaking, each transition between the two levels is accompanied with the absorption or emission of a photon and hence an exchange of momentum between the ion and the electromagnetic field. However, here we will assume that the Doppler cooling is a slow process such that the internal levels of the ion can reach a stable state at each velocity, and then the occupation of the excited state gives the rate of exchange of momentum, which

in turn tells us how the velocity of the ion changes. Note that this assumption is no longer true when we consider the micromotion, which is at a frequency comparable to the absorption and emission of the photons.

Written in the component form, the evolution of the density matrix is governed by

$$\dot{\rho}_{gg} = i\frac{\Omega}{2}\rho_{ge} - i\frac{\Omega}{2}\rho_{eg} + \Gamma\rho_{ee}, \tag{1.16}$$

$$\dot{\rho}_{ee} = -i\frac{\Omega}{2}\rho_{ge} + i\frac{\Omega}{2}\rho_{eg} - \Gamma\rho_{ee}, \tag{1.17}$$

$$\dot{\rho}_{ge} = \left[-\frac{\Gamma}{2} - i(\Delta - \boldsymbol{k}\cdot\boldsymbol{v})\right]\rho_{ge} + i\frac{\Omega}{2}\rho_{gg} - i\frac{\Omega}{2}\rho_{ee}, \tag{1.18}$$

$$\dot{\rho}_{eg} = \left[-\frac{\Gamma}{2} + i(\Delta - \boldsymbol{k}\cdot\boldsymbol{v})\right]\rho_{ge} - i\frac{\Omega}{2}\rho_{gg} + i\frac{\Omega}{2}\rho_{ee}. \tag{1.19}$$

As is mentioned above, we solve the stable solution for a slowly varying velocity $\boldsymbol{v}$ by setting all the time derivatives to zero. Then we recover the Eq. (99) of Ref. [20]:

$$\rho_{ee} = \frac{s/2}{1 + s + 4(\Delta - \boldsymbol{k}\cdot\boldsymbol{v})^2/\Gamma^2}, \tag{1.20}$$

where $s = 2\Omega^2/\Gamma^2$. The number of scattered photons per unit time is given by $\Gamma\rho_{ee}$. During one cycle of absorption and emission of photons, the average momentum change of the ion is simply $\hbar\boldsymbol{k}$ because the spontaneous emission is random in its direction; thus we get an effective force of $\hbar\Gamma\rho_{ee}\boldsymbol{k}$ on the ion. In the limit of small velocity, this force can be linearized as [20]

$$\boldsymbol{F}(\boldsymbol{v}) = \boldsymbol{F}_0(1 + \kappa\boldsymbol{k}\cdot\boldsymbol{v}/\Gamma), \tag{1.21}$$

where

$$\boldsymbol{F}_0 = \hbar\boldsymbol{k}\Gamma\frac{s/2}{1 + s + 4\Delta^2/\Gamma^2} \tag{1.22}$$

and

$$\kappa = \frac{8\Delta/\Gamma}{1 + s + 4\Delta^2/\Gamma^2}. \tag{1.23}$$

$\boldsymbol{F}_0$ simply shifts the equilibrium position of the ion in the trap, while the additional velocity-dependent term gives the damping of the ion along the direction of the laser beam (assume $\Delta < 0$). In the experiment, the direction of the laser is chosen to be at an angle to all the three principle axes of the trap, thus the motion in all these directions can be cooled.

Doppler cooling, however, cannot lead to arbitrarily low temperature, due to the randomness in the absorption and emission of the photons. It can be shown that the minimum temperature is of the order $k_B T \sim \hbar\Gamma$ [20]. To further lower the temperature, other techniques such as sideband cooling are needed. However, as we will see in the following chapters, ground-state cooling is not necessary for quantum gates in ion trap, although low temperature will definitely improve the gate fidelity.

As is mentioned, the above arguments no longer hold if the micromotion is included. This effect was studied in Refs. [25, 26], and it can be understood qualitatively as follows: the micromotion produces an additional sideband structure at the shifted frequencies of $n\omega_{\mathrm{rf}}$ ($n = 0, \pm 1, \pm 2, \cdots$), thus if the laser frequency is close to one sideband, the detuning Δ in the above equations should be replaced by the detuning to that sideband. Therefore a blue-detuned laser beam can still lead to cooling if it is closely red-detuned to a higher sideband, and vice versa for a red-detuned laser beam. In Chapter 3 we will consider the simulation of the classical motion of the ions. There we will take a different approach by modelling the scattering of the photons semiclassically using the quantum trajectory method (see Sec. 3.1.4).

Once we get an ion crystal at low temperature, we need to turn off the cooling lasers to

apply the gates. During this process, however, the ions are subjected to the heating from their environment. Typical heating sources are the electric noise on the electrodes and the collision with background neutral atoms. Usually the electric noise is at a long wavelength compared with the ion separations and hence it mainly heats the center-of-mass mode of the crystal. This knowledge can help us to estimate the effect of heating on the gate performance in Chapter 2.

The collision rate of the ions with the background gases is proportional to the pressure of the gases, and the kinetic energy of these atoms or molecules are proportional to the environmental temperature. Thus this heating rate can be reduced by improving the quality of the vacuum chamber or by placing the chamber into a refrigerator: it is not a fundamental limit for ion trap. Besides, remaining gases in the vacuum chamber are dominated by light molecules such as hydrogen [27]. Therefore only a small fraction of their kinetic energies can be transferred to the heavy ions (suppose we use $^{171}Yb^{+}$ ions) in an elastic collision. Actually, Ref. [27] computes the elastic collision rate to be $\gamma_{\text{elastic}} = 0.132/\text{s}$ at the pressure of 5 nPa and the temperature of 300 K, and the inelastic Langevin collision rate $\gamma_{\text{Langevin}} = 0.006/\text{s}$. Ref. [28] observes an average lifetime of about 5 min for a 53-ion chain and in rare cases even up to 30 min. Therefore this heating source shall not be a significant problem during the operation of the entangling gates, which is typically of the order 10^{-4} s (see Chapter 2). However, note that the collision rate is also proportional to the number of ions, so as we use more and more ions it may finally become an important source of error.

1.2.3 Raman Transition

For some ions commonly used for quantum computing such as $^{171}Yb^+$, $^9Be^+$ and $^{43}Ca^+$, the qubit levels are chosen to be two hyperfine ground states [29–32]. The advantage is a very long lifetime of the qubit, but these two levels are not directly coupled by an electric dipole transition and furthermore the transition is not at a typical laser frequency. To control the qubit states, we need two laser beams on the ion with a third ancilla level: this process is known as Raman transition [24].

Let us denote the two qubit levels as $|0\rangle$ and $|1\rangle$, and the ancilla level as $|e\rangle$ (see Fig. 1.2). Define the transition frequency between $|0\rangle$ and $|1\rangle$ as $\omega_{01} = (E_1 - E_0)/\hbar$ and similarly for ω_{0e} and ω_{1e}. These levels are coupled by two off-resonant laser beams at the frequencies of ω_1 and ω_2 with the Rabi frequencies Ω_1 and Ω_2.

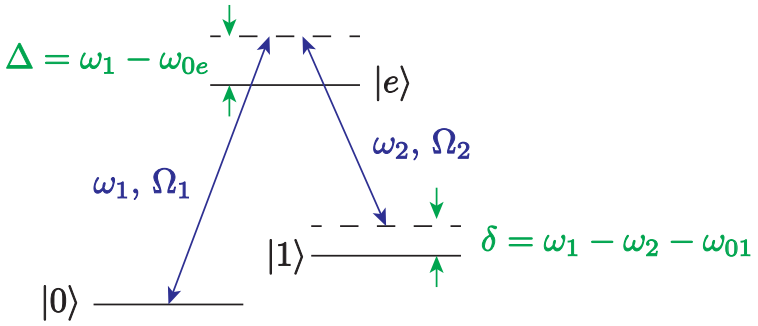

Figure 1.2: Schematic diagram of the three levels and the two Raman beams. (From Ref. [1], ©2018 American Physical Society.)

The Hamiltonian of the system (after rotating wave approximation) is

$$\begin{aligned} H =& \hbar\omega_{01}|1\rangle\langle 1| + \hbar\omega_{0e}|e\rangle\langle e| + \hbar\left(\frac{\Omega_1}{2}e^{-i\omega_1 t}|e\rangle\langle 0| + \frac{\Omega_1^*}{2}e^{i\omega_1 t}|0\rangle\langle e|\right) \\ &+ \hbar\left(\frac{\Omega_2}{2}e^{-i\omega_2 t}|e\rangle\langle 1| + \frac{\Omega_2^*}{2}e^{i\omega_2 t}|1\rangle\langle e|\right). \end{aligned} \tag{1.24}$$

Define $\Delta \equiv \omega_1 - \omega_{0e}$, $\delta \equiv \omega_1 - \omega_2 - \omega_{01}$. Now we move to an interaction picture [33] with

$$H_0 = \hbar(\omega_1 - \omega_2)|1\rangle\langle 1| + \hbar\omega_{0e}|e\rangle\langle e| \tag{1.25}$$

and get the interaction Hamiltonian

$$H_I = -\hbar\delta|1\rangle\langle 1| + \hbar\left(\frac{\Omega_1}{2}|e\rangle\langle 0|e^{-i\Delta t} + h.c.\right) + \hbar\left(\frac{\Omega_2}{2}|e\rangle\langle 1|e^{-i\Delta t} + h.c.\right). \tag{1.26}$$

This Hamiltonian fits exactly into the framework of Ref. [34], and we can get an effective time-independent Hamiltonian

$$\begin{aligned} H_{\text{eff}} = &-\hbar\delta|1\rangle\langle 1| + \hbar\frac{|\Omega_1|^2}{4\Delta}\left(|0\rangle\langle 0| - |e\rangle\langle e|\right) + \hbar\frac{|\Omega_2|^2}{4(\Delta-\delta)}\left(|1\rangle\langle 1| - |e\rangle\langle e|\right) \\ &+ \hbar\frac{1}{4(\Delta-\delta/2)}\left(\Omega_1\Omega_2^*|1\rangle\langle 0| + \Omega_1^*\Omega_2|0\rangle\langle 1|\right), \end{aligned} \tag{1.27}$$

with the relative error of the order $O(\delta^2/\Delta^2)$, and a time-dependent modulation of the order $O(|\Omega_{1(2)}|/|\Delta|)$:

$$K(t) = \frac{i}{2\Delta}\left(\Omega_1|e\rangle\langle 0|e^{-i\Delta t} - \Omega_1^*|0\rangle\langle e|e^{i\Delta t}\right) + \frac{i}{2(\Delta-\delta)}\left(\Omega_2|e\rangle\langle 1|e^{-i\Delta t} - \Omega_2^*|1\rangle\langle e|e^{i\Delta t}\right). \tag{1.28}$$

The complete time evolution from t_1 to t_2 is governed by

$$U(t_2, t_1) = e^{-iK(t_2)}e^{-iH_{\text{eff}}(t_2-t_1)}e^{iK(t_1)}. \tag{1.29}$$

Assuming $|\Delta| \gg |\Omega_1|, |\Omega_2|, \delta$, the error terms and the time-dependent modulation can be neglected. The second and third terms of the above effective Hamiltonian give the AC Stark

shift of the levels due to the off-resonant driving [24, 30]; while the first and the last terms describe the effective coupling between the two qubit levels $|0\rangle$ and $|1\rangle$. Specifically, it is a coupling term with detuning δ (and small corrections due to the level shifts) and effective Rabi frequency $\Omega_{\text{eff}} = \Omega_1\Omega_2^*/2(\Delta - \delta/2) \approx \Omega_1\Omega_2^*/2\Delta$.

Chapter 2

Entangling Gates in Ion Trap

In this chapter we will study how the entangling gates can be realized in ion trap with high fidelity. It is mainly based on the author's published paper [1]. In Sec. 2.1 we review a commonly used scheme to realize the XX entangling gate between any pair of ions in a small to medium-sized ion crystal. We will describe the scheme for a 1D ion chain, but the generalization to 2D or 3D is not difficult and will be discussed further in Chapter 3. Then in Sec. 2.2 we discuss the robustness of the gate under fluctuation in gate parameters and estimate the errors from the approximations in the formulation and the neglected physical effects. To give a concrete example, we optimize the gate design for several ion pairs in a linear chain of 19 $^{171}Yb^{+}$ ions, which is about the size of the current experimental platform for the demonstration of a logic qubit.

2.1 Entanglement through Collective Phonon Modes

For a small number of ions, one scheme to realize the entangling gate, known as the Molmer-Sorensen (MS) gate, has been proposed for two decades [35]. It utilizes a single phonon

mode of the ion crystal, typically the center-of-mass mode, to mediate a coupling between two ions' internal states, which is insensitive to the phonon number. However, as the number of ions increases, the motion of the ion crystal becomes progressively more complex and the crosstalk among different collective modes can lead to errors in the quantum gate [36]. A straightforward approach to suppress this crosstalk is to weaken the laser driving, but at the cost of increasing the gate time with the number of ions. One possible solution is to use an architecture called the quantum charge-coupled device [37–39], where entanglements are first generated in individual zones and are then distributed to other regions by a classical ion shuttling technique. Such a shuttling, however, demands exquisite control of ion positions. Here we will focus on a different approach, where all the collective modes are utilized to perform optimized entangling gates [40]. In this way, the existence of multiple phonon modes is no longer a source of error. One can then use amplitude or frequency modulations to optimize the gate performance.

In this chapter we will consider a linear ion chain and utilize the normal modes in the transverse direction. The formulation also holds for a 2D ion crystal with small correction due to the micromotion [41]. We will consider 3D crystals in the next chapter, where the role of micromotion is more important.

2.1.1 Equilibrium Positions and Transverse Modes

Consider N ions in a linear Paul trap along the z axis. A suitable quartic potential can be applied in the z direction through external electrodes, making the spacings of ions nearly uniform [42]. This can make the ion structure more stable against the zigzag shape and it will also produce a narrower transverse phonon spectrum, allowing more efficient cooling and

control. For typical experimental parameters, the micromotion is small and can be neglected for 1D ion chain in a linear Paul trap. Then we can calculate the equilibrium configuration as well as the collective oscillation modes by effectively treating the trap as a static pseudo-potential. An estimation for the introduced error can be found in Sec. 2.2.2 and a more general consideration of micromotion can be found in Chapter 3.

Therefore we consider the following potential energy

$$U = \sum_i \left(-\frac{1}{2}\alpha_2 z_i^2 + \frac{1}{4}\alpha_4 z_i^4 \right) + \sum_{i<j} \frac{e^2}{4\pi\epsilon_0 \left| z_i - z_j \right|} \tag{2.1}$$

with $\alpha_2, \alpha_4 > 0$. By defining the length unit $l_0 \equiv (e^2/4\pi\epsilon_0\alpha_2)^{1/3}$, dimensionless coordinate $u_i \equiv z_i/l_0$ and dimensionless potential energy $V \equiv 4\pi\epsilon_0 l_0 U/e^2$, we get

$$V = \sum_i \left(-\frac{1}{2}u_i^2 + \frac{1}{4}\gamma_4 u_i^4 \right) + \frac{1}{2}\sum_{i\neq j} \frac{1}{|u_i - u_j|}, \tag{2.2}$$

where $\gamma_4 \equiv \alpha_4 l_0^2/\alpha_2$ is a dimensionless constant which completely determines the shape of the equilibrium configuration. For a given number of ions and γ_4, we can minimize the potential energy to find the equilibrium positions using Newton's method [23], with the gradient and the Hessian matrix of the potential energy given by

$$\frac{\partial V}{\partial u_m} = -u_m + \gamma_4 u_m^3 - \sum_{j\neq m} \frac{u_m - u_j}{|u_m - u_j|^3}, \tag{2.3}$$

$$\frac{\partial^2 V}{\partial u_m^2} = -1 + 3\gamma_4 u_m^2 + \sum_{j\neq m} \frac{2}{|u_m - u_j|^3}, \tag{2.4}$$

$$\frac{\partial^2 V}{\partial u_m \partial u_n} = -\frac{2}{|u_m - u_n|^3} \qquad (m \neq n). \tag{2.5}$$

For the example we use in Sec. 2.2 (17 ions for computation and 2 auxiliary ions at the ends), we adjust γ_4 to minimize the relative standard deviation (RSD) for the spacings of the 17 computing ions. $\gamma_4 = 4.3$ is found to give a minimal RSD of only 2.3%; in comparison, a harmonic trap gives rise to an RSD of 11.2% (see Fig. 2.1).

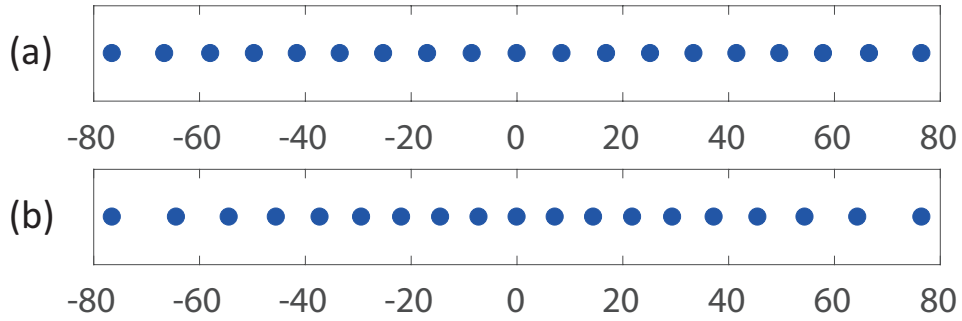

Figure 2.1: (a) Equilibrium positions for an anharmonic trap potential with $\gamma_4 = 4.3$ and $l_0 = 40$ (arbitrary unit). (b) Equilibrium positions for a harmonic trap potential that can produce the same average ion spacing. (From Ref. [1], ©2018 American Physical Society.)

After finding the equilibrium positions $\{u_i^{(0)}\}$ along the axial z direction, we further consider the normal modes by expanding the complete expression of the potential energy

$$U = \sum_i \left(-\frac{1}{2}\alpha_2 z_i^2 + \frac{1}{4}\alpha_4 z_i^4 + \frac{1}{2}m\omega_x^2 x_i^2 + \frac{1}{2}m\omega_y^2 y_i^2 \right) + \frac{e^2}{4\pi\epsilon_0} \sum_{i<j} \frac{1}{|\boldsymbol{r}_i - \boldsymbol{r}_j|} \tag{2.6}$$

around the equilibrium positions $x_i^{(0)} = y_i^{(0)} = 0$, $z_i^{(0)} = l_0 u_i^{(0)}$. The Taylor series up to the second order is given by:

$$U = U_0 + \frac{1}{2} \sum_{i,j,\alpha,\beta} \left. \frac{\partial^2 U}{\partial r_{i,\alpha} \partial r_{j,\beta}} \right|_{r_{i,\alpha} = r_{i,\alpha}^{(0)}} \times \left(r_{i,\alpha} - r_{i,\alpha}^{(0)} \right) \left(r_{j,\beta} - r_{j,\beta}^{(0)} \right) + \cdots \tag{2.7}$$

where α, $\beta = 1, 2, 3$ correspond to the three Cartesian coordinates, while i, $j = 1, 2, \cdots, N$ correspond to each ion. Since we are only interested in small oscillations around the equi-

librium configuration, the quadratic term in the expansion suffices to describe the motion, which is separable in the x, y and z directions. The nonlinear effect of the higher order interaction is briefly discussed in Sec. 2.2.2. Here we only consider the transverse motion in the x direction, while the modes in the y and z directions can be obtained in a similar way. Define $z_{ij} \equiv |z_i^{(0)} - z_j^{(0)}|$. At the equilibrium positions we have

$$\frac{\partial^2 U}{\partial x_m^2} = m\omega_x^2 - \frac{e^2}{4\pi\epsilon_0}\sum_{j\neq m}\frac{1}{z_{mj}^3}, \tag{2.8}$$

$$\frac{\partial^2 U}{\partial x_m \partial x_n} = \frac{e^2}{4\pi\epsilon_0}\frac{1}{z_{mn}^3} \qquad (m \neq n). \tag{2.9}$$

We can then diagonalize this matrix to find the normal modes of the transverse motion, with the k-th normalized mode vector denoted by b_j^k ($j = 1, 2, \cdots, N$). These modes can be quantized to give the phonon Hamiltonian.

2.1.2 Hamiltonian and Time Evolution Operator

We start from a three-level approximation of the ion's level structure (Fig. 1.2). Later we will adiabatically eliminate the excited state to attain the two-level approximation. The free Hamiltonian of this system is

$$H = \hbar\sum_{i=1}^{N}(\omega_{01}|1\rangle_i\langle 1| + \omega_{0e}|e\rangle_i\langle e|) + \hbar\sum_k \omega_k a_k^\dagger a_k, \tag{2.10}$$

where $\hbar\omega_{01} \equiv E_1 - E_0$ is the energy difference between $|0\rangle$ and $|1\rangle$ (typically two hyperfine "clock" states of the ion [29–32]) and $\hbar\omega_{0e} \equiv E_e - E_0$ is the energy splitting between $|0\rangle$ and an excited state $|e\rangle$. ω_k is the frequency of the k-th phonon mode, with the corresponding

annihilation (creation) operator a_k ($a_k^\dagger$).

For simplicity, let us first consider one ion, say ion j, in the chain of N ions. Suppose two beams of laser (with frequencies and wave vectors ω_i, $\boldsymbol{k}_i$, $i = 1, 2$) are shined on the ion to off-resonantly couple states $|0\rangle$ and $|e\rangle$, and $|1\rangle$ and $|e\rangle$, with Rabi frequencies $\Omega_1(t)$ and $\Omega_2(t)$ respectively (see Fig. 1.2). This corresponds to the following coupling Hamiltonian

$$\begin{aligned} H' =& \hbar\Omega_1 \cos\left(\boldsymbol{k}_1 \cdot \boldsymbol{r}_j - \omega_1 t - \varphi_1\right)\left(|0\rangle_j\langle e| + |e\rangle_j\langle 0|\right) \\ &+ \hbar\Omega_2 \cos\left(\boldsymbol{k}_2 \cdot \boldsymbol{r}_j - \omega_2 t - \varphi_2\right)\left(|1\rangle_j\langle e| + |e\rangle_j\langle 1|\right), \end{aligned} \tag{2.11}$$

where Ω_1 and Ω_2 are chosen to be real. The time dependence of the Rabi frequency has been omitted for convenience. Following the step of Sec. 1.2.3 we define $\Delta \equiv \omega_1 - \omega_{0e}$ as the single-photon detuning and $\delta \equiv \omega_1 - \omega_2 - \omega_{01}$ as the two-photon detuning. Here we assume $|\delta| \ll \omega_{01}$ so that we can neglect other two-photon processes between $|0\rangle$ and $|1\rangle$.

Now we perform a unitary transformation characterized by $U = \exp(-iH_0 t/\hbar)$ with

$$H_0 = \hbar \sum_{i \neq j} \left(\omega_{01}|1\rangle_i\langle 1| + \omega_{0e}|e\rangle_i\langle e|\right) + \hbar \sum_k \omega_k a_k^\dagger a_k + \hbar\left(\omega_{01}|1\rangle_j\langle 1| + \omega_1|e\rangle_j\langle e|\right). \tag{2.12}$$

Then the Hamiltonian in the transformed frame, a.k.a. the Hamiltonian in the interaction picture [33], is given by

$$\begin{aligned} H_I =& U^\dagger H U + i\frac{\partial U^\dagger}{\partial t} U \\ =& -\hbar\Delta|e\rangle_j\langle e| + \frac{\hbar\Omega_1}{2}\Big\{|e\rangle_j\langle 0| e^{i[\boldsymbol{k}_1 \cdot \boldsymbol{r}_j(t) - \varphi_1]} + h.c.\Big\} \\ &+ \frac{\hbar\Omega_2}{2}\Big\{|e\rangle_j\langle 1| e^{i[\boldsymbol{k}_2 \cdot \boldsymbol{r}_j(t) - \varphi_2 + \delta \cdot t]} + h.c.\Big\}, \end{aligned} \tag{2.13}$$

where $\boldsymbol{r}_j(t)$ is the position operator of ion j at time t, under the free evolution of the collective phonon modes. Here we have made the rotating wave approximation (RWA) with the requirement $|\delta|$, $|\Omega_1|$, $|\Omega_2| \ll \omega_1$, ω_2.

Assume $|\Delta| \gg |\delta|$, $|\Omega_1|$, $|\Omega_2|$, γ_e so that the excited state can be adiabatically eliminated, where γ_e is the spontaneous emission rate of the excited state. This describes a Raman transition between the state $|0\rangle_j$ and $|1\rangle_j$ (see Sec. 1.2.3). The effective coupling is given by

$$H_I^{(\text{eff})} = \hbar \frac{\Omega_1 \Omega_2}{4\Delta} e^{-i[\boldsymbol{\Delta k} \cdot \boldsymbol{r}_j(t) - \delta \cdot t - \Delta\varphi]} |0\rangle_j \langle 1| + h.c. \tag{2.14}$$

where $\boldsymbol{\Delta k} \equiv \boldsymbol{k}_1 - \boldsymbol{k}_2$, $\Delta\varphi \equiv \varphi_1 - \varphi_2$. The states $|0\rangle$ and $|1\rangle$ are coupled by an effective Rabi frequency $\Omega_j^{(\text{eff})} \equiv \Omega_1\Omega_2/2\Delta$. Later, for simplicity, we drop the superscript and denote the effective Rabi frequency on ion j by Ω_j.

The laser also produces AC Stark shift on the two levels. By suitably choosing the relative intensity of the two laser beams and the detuning Δ with respect to the excited states, we can make the shifts on the two levels nearly the same [7, 43]. We will discuss more about this effect in Sec. 2.2.

This effective coupling depends on the relative phase of the two laser beams and therefore the fluctuation on their paths. This problem can be solved by adding a third laser beam to form two pairs of Raman transitions, with detuning $\delta = \pm\mu$ and wave vector difference $\pm\Delta k$ along the x direction (see Fig. 2.2). This is known as the phase-insensitive geometry [44]. We will also briefly discuss the relevance to the phase-sensitive geometry at the end of this subsection.

The effective Rabi frequencies of both pairs are chosen to be Ω_j. Here we assume $\omega_{01} \ll \omega_1$, ω_2, ω_3, so that Δk is nearly the same for both pairs, with a relative error of the order

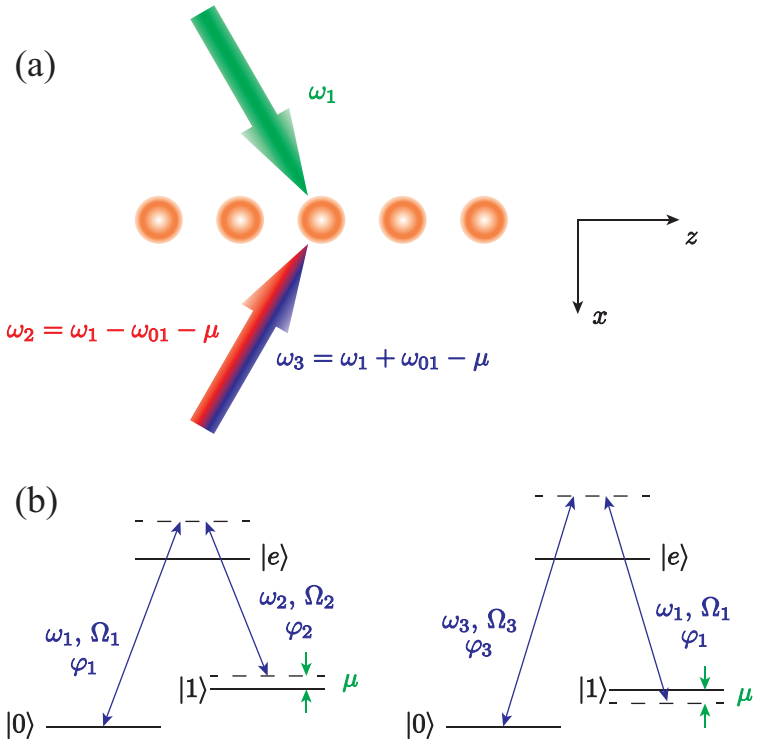

Figure 2.2: (a) Schematic experimental setup. Three beams are shined on the ion, with one beam in the direction of $\boldsymbol{k}_1$ and the other two red- and blue-detuned beams in the direction of $\boldsymbol{k}_2$. (b) Schematic energy levels and the two pairs of Raman transitions. (From Ref. [1], ©2018 American Physical Society.)

ω_{01}/ω_1. Suppose the initial phase differences for the two pairs are $\Delta\varphi_b \equiv \varphi_1 - \varphi_2$ and $\Delta\varphi_r \equiv \varphi_3 - \varphi_1$. Then the total interaction Hamiltonian can be written as

$$\begin{aligned}
H_I^{(\text{eff})} &= \frac{\hbar\Omega_j}{2}\left[e^{-i\Delta k\cdot x_j(t)}e^{i\mu t}e^{i\Delta\varphi_b} + e^{i\Delta k\cdot x_j(t)}e^{-i\mu t}e^{i\Delta\varphi_r}\right]|0\rangle_j\langle 1| + h.c. \\
&= \frac{\hbar\Omega_j}{2}\left[e^{-i\Delta k\cdot x_j(t)}e^{i\mu t}e^{i\varphi_j^{(m)}}e^{i\varphi_j^{(s)}} + e^{i\Delta k\cdot x_j(t)}e^{-i\mu t}e^{-i\varphi_j^{(m)}}e^{i\varphi_j^{(s)}}\right]|0\rangle_j\langle 1| + h.c. \\
&= \hbar\Omega_j\cos\left[\mu t + \varphi_j^{(m)} - \Delta k\cdot x_j(t)\right]\left(e^{i\varphi_j^{(s)}}|0\rangle_j\langle 1| + e^{-i\varphi_j^{(s)}}|1\rangle_j\langle 0|\right) \\
&= \hbar\Omega_j\cos\left[\mu t + \varphi_j^{(m)} - \Delta k\cdot x_j(t)\right]\left(\sigma_j^x\cos\varphi_j^{(s)} - \sigma_j^y\sin\varphi_j^{(s)}\right), \qquad (2.15)
\end{aligned}$$

where $\varphi_j^{(m)} \equiv (\Delta\varphi_b - \Delta\varphi_r)/2$ and $\varphi_j^{(s)} \equiv (\Delta\varphi_b + \Delta\varphi_r)/2$ are called the motional phase and the spin phase [44]. The subscript j is used to show that these phases pertain to ion j. Small fluctuation in beams' paths causes opposite changes in $\Delta\varphi_b$ and $\Delta\varphi_r$, so $\varphi_j^{(s)}$ is robust against fluctuation. On the other hand, $\varphi_j^{(m)}$ does change, but it can be quite stable during one gate time. As we will show later, the gate fidelity is not sensitive to a constant $\varphi_j^{(m)}$ so long as the phase is the same for both ions. Finally we will choose $\varphi_j^{(m)} = 0$ and $\varphi_j^{(s)} = 0$, but for the moment let us keep them in the formulae for completeness.

We further define $\sigma_j^n \equiv \sigma_j^x \cos\varphi_j^{(s)} - \sigma_j^y \sin\varphi_j^{(s)}$ to simplify and drop the superscript on $H_I^{(\text{eff})}$:

$$H_I = \hbar\Omega_j(t) \cos\left[\mu t + \varphi_j^{(m)} - \Delta k \cdot x_j(t)\right] \sigma_j^n. \tag{2.16}$$

As we have seen in Sec. 2.1.1, for the linear ion chain the small oscillations along x, y, z directions are separable and the transverse motion of ion j can be quantized as

$$x_j(t) = \sum_k b_j^k \sqrt{\frac{\hbar}{2m\omega_k}} \left(a_k e^{-i\omega_k t} + a_k^\dagger e^{i\omega_k t}\right), \tag{2.17}$$

where b_j^k ($j = 1, 2, \cdots, N$) characterizes the k-th normalized mode vector of the collective oscillation. The summation over k is limited to the transverse modes along the x direction. (In Chapter 3 we will consider general 3D ion crystal, where the motions are no longer separable in the three spatial directions. Then we need to sum over all the $3N$ normal modes and project them onto the direction of $\boldsymbol{\Delta k}$.)

With the Lamb-Dicke parameter $\eta_k \equiv \Delta k\sqrt{\hbar/2m\omega_k}$, we get

$$H_I = \hbar\Omega_j\sigma_j^n \cos\left[\mu t + \varphi_j^{(m)} - \sum_k \eta_k b_j^k \left(a_k e^{-i\omega_k t} + a_k^\dagger e^{i\omega_k t}\right)\right]. \tag{2.18}$$

We can expand this expression according to the power of η_k:

$$\begin{aligned} H_I =& \hbar\Omega_j \Bigg[\cos\left(\mu t + \varphi_j^{(m)}\right) + \sin\left(\mu t + \varphi_j^{(m)}\right) \sum_k \eta_k b_j^k \left(a_k e^{-i\omega_k t} + a_k^\dagger e^{i\omega_k t}\right) \\ & - \frac{1}{2}\cos\left(\mu t + \varphi_j^{(m)}\right) \\ & \times \sum_k \sum_l \eta_k \eta_l b_j^k b_j^l \left(a_k e^{-i\omega_k t} + a_k^\dagger e^{i\omega_k t}\right)\left(a_l e^{-i\omega_l t} + a_l^\dagger e^{i\omega_l t}\right) \Bigg] \sigma_j^n + O(\eta_k^3). \end{aligned} \tag{2.19}$$

The zeroth order term is a single-qubit operation and commutes with other terms. So we can drop it now and apply a single-qubit rotation after the entangling gate to compensate its effect. Actually for the examples considered in Sec. 2.2, we will show that such a compensation is unnecessary. Here we keep terms up to the second order, but we will show later that the error in the fidelity is of the order $O(\eta_k^4)$.

When the lasers are shined on two ions, we get the interaction-picture Hamiltonian

$$\begin{aligned} H_I =& \sum_{j=j_1,j_2} \sum_k \chi_j(t)\eta_k b_j^k \left(a_k e^{-i\omega_k t} + a_k^\dagger e^{i\omega_k t}\right)\sigma_j^n \\ & - \frac{1}{2}\sum_{j=j_1,j_2} \sum_k \sum_l \theta_j(t)\eta_k\eta_l b_j^k b_j^l \left(a_k e^{-i\omega_k t} + a_k^\dagger e^{i\omega_k t}\right)\left(a_l e^{-i\omega_l t} + a_l^\dagger e^{i\omega_l t}\right)\sigma_j^n, \end{aligned} \tag{2.20}$$

where the summation of j is over the two ions and

$$\chi_j(t) \equiv \hbar\Omega_j \sin\left(\mu t + \varphi_j^{(m)}\right), \tag{2.21}$$

$$\theta_j(t) \equiv \hbar\Omega_j \cos\left(\mu t + \varphi_j^{(m)}\right). \tag{2.22}$$

Unitary evolution in the interaction picture is obtained by the Magnus expansion [45]

$$U_I(\tau) \approx \exp\left(i \sum_j \left[\phi_j(\tau) + \psi_j(\tau)\right] \sigma_j^n + i \sum_{i<j} \Theta_{ij}(\tau) \sigma_i^n \sigma_j^n \right), \tag{2.23}$$

where

$$\phi_j(\tau) = -i \sum_k \left[\alpha_j^k(\tau) a_k^\dagger - \alpha_j^{k*}(\tau) a_k \right], \tag{2.24}$$

$$\alpha_j^k(\tau) = -\frac{i}{\hbar} \eta_k b_j^k \int_0^\tau \chi_j(t) e^{i\omega_k t} dt, \tag{2.25}$$

and

$$\psi_j(\tau) = \sum_k \lambda_j^k(\tau) \left(a_k^\dagger a_k + \frac{1}{2} \right), \tag{2.26}$$

$$\lambda_j^k(\tau) = \frac{1}{\hbar} \left(\eta_k b_j^k \right)^2 \int_0^\tau \theta_j(t) dt \tag{2.27}$$

describe the coupling between the spin and phonon modes, and

$$\Theta_{ij}(\tau) = \frac{1}{\hbar^2} \sum_k \eta_k^2 b_i^k b_j^k \int_0^\tau dt_1 \int_0^{t_1} dt_2 \left[\chi_i(t_1)\chi_j(t_2) + \chi_j(t_1)\chi_i(t_2) \right] \sin\left[\omega_k(t_1 - t_2)\right] \tag{2.28}$$

is the coupling between the two spins. Roughly speaking, the ϕ_j terms are displacement operations on the phonon modes conditioned on the spin state of each ion, and the ψ_j terms are single-spin rotations conditioned on the phonon numbers of each mode. We need to suppress these terms while maintain a large spin-spin coupling to realize the entangling gate. Here again we keep terms up to the second order in η_k and retain only diagonal terms in $\psi_j(\tau)$ [Eq. (2.26)]. An error analysis will be performed in Sec. 2.2.2. In the above derivation we have also dropped a global phase, which has no effect on the entangling gate.

If the effective Rabi frequencies of the laser beams on the two ions are always proportional,

e.g. when the lasers come from a single beam through a beam splitter, the expression of Θ_{ij} can be simplified as

$$\Theta_{ij}(\tau) = \frac{2}{\hbar^2}\sum_k \eta_k^2 b_i^k b_j^k \int_0^\tau dt_1 \int_0^{t_1} dt_2 \chi_i(t_1)\chi_j(t_2)\sin\left[\omega_k(t_1-t_2)\right]. \tag{2.29}$$

In this way we recover Eq. (2) of Ref. [40].

In the above derivation we assumed a phase-insensitive laser configuration. It is also possible to use the phase-sensitive geometry for the entangling gate with the spin phase being cancelled by a Ramsey-like gate design [32, 44]. In this case, we choose $\boldsymbol{\Delta k}$ to be the same for the two Raman transitions, then instead of Eq. (2.19) we get

$$\begin{aligned} H_I' =& \hbar\Omega_j \cos\left(\mu t + \varphi_j^{(m)}\right)\left[\sigma_j^n - \sigma_j^\perp \sum_k \eta_k b_j^k \left(a_k e^{-i\omega_k t} + a_k^\dagger e^{i\omega_k t}\right)\right. \\ & \left. - \frac{1}{2}\sigma_j^n \sum_k \sum_l \eta_k \eta_l b_j^k b_j^l \left(a_k e^{-i\omega_k t} + a_k^\dagger e^{i\omega_k t}\right)\left(a_l e^{-i\omega_l t} + a_l^\dagger e^{i\omega_l t}\right)\right] + O(\eta_k^3) \end{aligned} \tag{2.30}$$

where $\sigma_j^\perp \equiv \sigma_j^x \sin\varphi_j^{(s)} + \sigma_j^y \cos\varphi_j^{(s)}$ is orthogonal to $\sigma_j^n \equiv \sigma_j^x \cos\varphi_j^{(s)} - \sigma_j^y \sin\varphi_j^{(s)}$. Also note that here $\varphi_j^{(s)}$ is sensitive to fluctuation in the paths of the laser beams while $\varphi_j^{(m)}$ is not.

Because $\sigma_j^\perp$ anti-commutes with σ_j^n, a direct Magnus expansion as before will give us infinitely many terms even if we truncate at the first order of η_k due to the carrier term. Instead, we can move into a new interaction picture with $H_0' = \hbar\Omega_j \cos(\mu t + \varphi_j^{(m)})\sigma_j^n$, which will leave the second order σ_j^n term unchanged but turn the first order $\sigma_j^\perp$ term into a combination of $\sigma_j^\perp$ and σ_z. Then similar derivation can be made, although the expressions are more complex. Note that for previous experiments with only a few ions, usually $\Omega_j \ll \mu$ is satisfied [32] so that the correction term of σ_z will be small. However, for a larger ion crystal we may want to increase the laser intensity to shorten the gate time. Actually for the example we consider

in Sec. 2.2, Ω_j is only about a factor of 3 smaller than μ, so the correction term may not be negligible. Nevertheless, many other error analyses in Sec. 2.2 should still work for the phase-sensitive setup.

2.1.3 XX Entangling Gate and Fidelity

If $\alpha_j^k(\tau) = 0$ [Eq. (2.25)] and $\lambda_j^k(\tau) = 0$ [Eq. (2.27)] for all the modes and both of the ions, $\varphi_j^{(s)} = 0$ for both ions, and $\Theta_{ij} = \pi/4$ for the ion pair of interest, i and j, the time evolution operator will be an ideal XX entangling gate. In the basis of $|+\rangle_i|+\rangle_j$, $|+\rangle_i|-\rangle_j$, $|-\rangle_i|+\rangle_j$ and $|-\rangle_i|-\rangle_j$ where $|\pm\rangle = \frac{1}{\sqrt{2}}(|0\rangle \pm |1\rangle)$, we have

$$U_{\text{ideal}} = e^{i\pi\sigma_i^x\sigma_j^x/4} = \begin{pmatrix} e^{i\pi/4} & 0 & 0 & 0 \\ 0 & e^{-i\pi/4} & 0 & 0 \\ 0 & 0 & e^{-i\pi/4} & 0 \\ 0 & 0 & 0 & e^{i\pi/4} \end{pmatrix}. \tag{2.31}$$

The subscript ij and the dependence on τ have been dropped. This gate is equivalent to the CNOT gate described in Sec. 1.1 up to single qubit gates, e.g.

$$\text{CNOT} = (I_1 \otimes H_2)(S_1 \otimes S_2)(H_1 \otimes H_2)e^{i\pi\sigma_i^x\sigma_j^x/4}(H_1 \otimes I_2) \tag{2.32}$$

where we have thrown away an irrelevant global phase. Note that to compare these two gates we need to use the same basis, say, the computational basis.

If the initial internal state is $|\Psi_0\rangle$ and the vibrational modes are in the thermal state ρ_{th} with a temperature T, the ideal final state is $U_{\text{ideal}}|\Psi_0\rangle$, while the actual state we get is

$\rho = \mathrm{tr}_m[U|\Psi_0\rangle\langle\Psi_0| \otimes \rho_{\mathrm{th}} U^\dagger]$ (neglecting all the other decoherence during the gate), where U is given by Eq. (2.23) and tr_m means the partial trace over all the motional modes. Then we can use average gate fidelity to characterize the similarity between U and U_{ideal} (see Sec. 1.1).

For the moment we assume the spin phases $\varphi_j^{(s)} = 0$ for the two ions, i.e. $\hat{n} = \hat{x}$, $\sigma_j^n = \sigma_j^x$. Later we will discuss the effects of nonzero spin phases in Sec. 2.2.1.

Let us express U in the above basis:

$$U = \begin{pmatrix} e^{i\Phi_{00}} & 0 & 0 & 0 \\ 0 & e^{i\Phi_{01}} & 0 & 0 \\ 0 & 0 & e^{i\Phi_{10}} & 0 \\ 0 & 0 & 0 & e^{i\Phi_{11}} \end{pmatrix}, \tag{2.33}$$

where $\Phi_{00} = \phi_i + \psi_i + \phi_j + \psi_j + \Theta_{ij}$, $\Phi_{01} = \phi_i + \psi_i - \phi_j - \psi_j - \Theta_{ij}$, $\Phi_{10} = -\phi_i - \psi_i + \phi_j + \psi_j - \Theta_{ij}$, $\Phi_{11} = -\phi_i - \psi_i - \phi_j - \psi_j + \Theta_{ij}$ [see Eq. (2.23) for their definitions] are the phases gained by the $|+\rangle_i|+\rangle_j$, $|+\rangle_i|-\rangle_j$, $|-\rangle_i|+\rangle_j$, $|-\rangle_i|-\rangle_j$ states, respectively. Note that they are actually operators in the subspace of phonon modes.

Accurate up to second order diagonal terms in η_k, we have

$$e^{i\Phi_{00}} \approx e^{i\Theta_{ij}} \prod_k D_k\left(\alpha_i^k(\tau) + \alpha_j^k(\tau)\right) \left\{1 + i\sum_l \left[\lambda_i^l(\tau) + \lambda_j^l(\tau)\right]\left(a_l^\dagger a_l + \frac{1}{2}\right)\right\}, \tag{2.34}$$

$$e^{i\Phi_{01}} \approx e^{-i\Theta_{ij}} \prod_k D_k\left(\alpha_i^k(\tau) - \alpha_j^k(\tau)\right) \left\{1 + i\sum_l \left[\lambda_i^l(\tau) - \lambda_j^l(\tau)\right]\left(a_l^\dagger a_l + \frac{1}{2}\right)\right\}, \tag{2.35}$$

$$e^{i\Phi_{10}} \approx e^{-i\Theta_{ij}} \prod_k D_k\left(-\alpha_i^k(\tau) + \alpha_j^k(\tau)\right) \left\{1 - i\sum_l \left[\lambda_i^l(\tau) - \lambda_j^l(\tau)\right]\left(a_l^\dagger a_l + \frac{1}{2}\right)\right\}, \tag{2.36}$$

$$e^{i\Phi_{11}} \approx e^{i\Theta_{ij}} \prod_k D_k\left(-\alpha_i^k(\tau) - \alpha_j^k(\tau)\right) \left\{1 - i\sum_l \left[\lambda_i^l(\tau) + \lambda_j^l(\tau)\right]\left(a_l^\dagger a_l + \frac{1}{2}\right)\right\}, \tag{2.37}$$

where $D_k(\alpha) \equiv \exp(\alpha a_k^\dagger - \alpha^* a_k)$ is the displacement operator of the k-th mode.

For an arbitrary operator ρ_0 (not necessarily Hermitian)

$$\rho_0 = \begin{pmatrix} \rho_{00,00} & \rho_{00,01} & \rho_{00,10} & \rho_{00,11} \\ \rho_{01,00} & \rho_{01,01} & \rho_{01,10} & \rho_{01,11} \\ \rho_{10,00} & \rho_{10,01} & \rho_{10,10} & \rho_{10,11} \\ \rho_{11,00} & \rho_{11,01} & \rho_{11,10} & \rho_{11,11} \end{pmatrix}, \tag{2.38}$$

lengthy but straightforward calculation shows that

$$\begin{aligned} \rho &= \mathrm{tr}_m[U\rho_0 \otimes \rho_{\mathrm{th}} U^\dagger] \\ &\approx \begin{pmatrix} \rho_{00,00} & \Gamma_j\Lambda_j e^{2i\Theta_{ij}-i\epsilon}\rho_{00,01} & \Gamma_i\Lambda_i e^{2i\Theta_{ij}+i\epsilon}\rho_{00,10} & \Gamma_+\Lambda_+\rho_{00,11} \\ \Gamma_j\Lambda_j^* e^{-2i\Theta_{ij}+i\epsilon}\rho_{01,00} & \rho_{01,01} & \Gamma_-\Lambda_-\rho_{01,10} & \Gamma_i\Lambda_i e^{-2i\Theta_{ij}-i\epsilon}\rho_{01,11} \\ \Gamma_i\Lambda_i^* e^{-2i\Theta_{ij}-i\epsilon}\rho_{10,00} & \Gamma_-\Lambda_-^*\rho_{10,01} & \rho_{10,10} & \Gamma_j\Lambda_j e^{-2i\Theta_{ij}+i\epsilon}\rho_{10,11} \\ \Gamma_+\Lambda_+^*\rho_{11,00} & \Gamma_i\Lambda_i^* e^{2i\Theta_{ij}+i\epsilon}\rho_{11,01} & \Gamma_j\Lambda_j^* e^{2i\Theta_{ij}-i\epsilon}\rho_{11,10} & \rho_{11,11} \end{pmatrix}, \end{aligned} \tag{2.39}$$

where $\epsilon = 2\sum_k \mathrm{Im}(\alpha_i^k \alpha_j^{k*})$,

$$\Gamma_{i(j)} = \exp\left[-2\sum_k \left|\alpha_{i(j)}^k\right|^2 \coth\left(\frac{\hbar\omega_k}{2k_BT}\right)\right], \tag{2.40}$$

$$\Gamma_\pm = \exp\left[-2\sum_k \left|\alpha_i^k \pm \alpha_j^k\right|^2 \coth\left(\frac{\hbar\omega_k}{2k_BT}\right)\right], \tag{2.41}$$

$$\Lambda_{i(j)} = 1 + i\sum_k \lambda_{i(j)}^k \coth\frac{\hbar\omega_k}{2k_BT}, \tag{2.42}$$

$$\Lambda_{\pm} = 1 + i \sum_k \left(\lambda_i^k \pm \lambda_j^k\right) \coth \frac{\hbar\omega_k}{2k_B T}. \tag{2.43}$$

We have used the following formulae in the derivation:

$$D(\alpha)D(\beta) = e^{(\alpha\beta^* - \alpha^*\beta)/2} D(\alpha+\beta), \tag{2.44}$$

$$\mathrm{tr}\left[D(\alpha)\rho_{\mathrm{th}}\right] = \exp\left[-\frac{|\alpha|^2}{2}\coth\left(\frac{\hbar\omega}{2k_B T}\right)\right], \tag{2.45}$$

$$\mathrm{tr}\left[\left(a^\dagger a + \frac{1}{2}\right)\rho_{\mathrm{th}}\right] = \frac{1}{2}\coth\left(\frac{\hbar\omega}{2k_B T}\right). \tag{2.46}$$

Now we plug Eq. (2.39) into Eq. (1.8) of average gate fidelity and we finally obtain

$$\overline{F} \approx \frac{1}{10}\big[4 + 2\Gamma_i \sin(2\Theta_{ij} + \epsilon) + 2\Gamma_j \sin(2\Theta_{ij} - \epsilon) + \Gamma_+ + \Gamma_-\big]. \tag{2.47}$$

λ_j^k terms [Eq. (2.27)] appear quadratically in the fidelity, hence its contribution is $O(\eta_k^4)$ and is neglected. If $\Omega \lesssim \mu$, ω_k and the average phonon number for a typical mode is $\bar{n}$, the error from neglecting higher order terms is of the order $\eta_k^4(2\bar{n}+1)^2$. The fact that there are N independent transverse modes has already been included because the coefficient for each mode is also modulated by the b_j^k vectors, which are normalized to 1.

Suppose the laser intensities on the two ions are always proportional and that their phases are locked such that $\varphi_i^{(m)} = \varphi_j^{(m)} = 0$, then we get $\epsilon = 0$. The above expression can be simplified as

$$\overline{F} = \frac{1}{10}\left[4 + 2(\Gamma_i + \Gamma_j)\sin 2\Theta_{ij} + \Gamma_+ + \Gamma_-\right]. \tag{2.48}$$

This average gate fidelity is slightly higher than Eq. (3) of Ref. [40], where a special initial state is used.

Also notice that if $\Theta_{ij} = -\pi/4$, the gate is close to another ideal entangling gate $\exp(-i\pi\sigma_i^x\sigma_j^x/4)$, which is different from U_{ideal} only by single-qubit operations. In this case the gate fidelity can be calculated in a similar way and the final result is

$$\overline{F} = \frac{1}{10}\left[4 - 2(\Gamma_i + \Gamma_j)\sin 2\Theta_{ij} + \Gamma_+ + \Gamma_-\right]. \tag{2.49}$$

From now on, by fidelity we mean the average gate fidelity if not specifically mentioned. We will drop the overline on F for convenience.

Up to this point, our derivations are general: any methods can be used to optimize the pulse sequence such as amplitude, frequency or phase modulations [40, 46, 47] and our target is a high gate fidelity given by Eq. (2.48) or Eq. (2.49). In the following, we will focus on the amplitude modulation method, which gives a simple analytic formula for the gate design.

In the experiment, we can set the laser beams on the two ions to be the same. We can divide the laser sequence into n_{seg} equal segments and in each segment let the Rabi frequency be a constant. Define a real column vector $\boldsymbol{\Omega} = (\Omega_1, \Omega_2, \cdots, \Omega_{n_{\text{seg}}})^T$ corresponding to the Rabi frequency of each segment, and we get

$$\alpha_j^k(\tau) = \boldsymbol{A}_j^k\boldsymbol{\Omega}, \quad \Theta_{ij} = \boldsymbol{\Omega}^T\boldsymbol{\gamma}'\boldsymbol{\Omega}, \tag{2.50}$$

where $\boldsymbol{A}_j^k$ is a row vector whose n-th component is

$$\boldsymbol{A}_j^k(n) = -i\eta_k b_j^k \int_{(n-1)\tau/n_{\text{seg}}}^{n\tau/n_{\text{seg}}} \sin\mu t \cdot e^{i\omega_k t} dt, \tag{2.51}$$

and $\boldsymbol{\gamma}'$ is an $n_{\rm seg}$ by $n_{\rm seg}$ matrix whose (p,q) component is

$$\boldsymbol{\gamma}'(p,q) = \begin{cases} 2\sum_k \eta_k^2 b_i^k b_j^k \int_{(p-1)\tau/n_{\rm seg}}^{p\tau/n_{\rm seg}} dt_1 \int_{(q-1)\tau/n_{\rm seg}}^{q\tau/n_{\rm seg}} dt_2 \sin\mu t_1 \sin\mu t_2 \sin[\omega_k(t_1-t_2)] & (p>q) \\ 2\sum_k \eta_k^2 b_i^k b_j^k \int_{(p-1)\tau/n_{\rm seg}}^{p\tau/n_{\rm seg}} dt_1 \int_{(p-1)\tau/n_{\rm seg}}^{t_1} dt_2 \sin\mu t_1 \sin\mu t_2 \sin[\omega_k(t_1-t_2)] & (p=q) \\ 0 & (p<q) \end{cases} . \tag{2.52}$$

We can further define a symmetric matrix $\boldsymbol{\gamma} \equiv (\boldsymbol{\gamma}' + \boldsymbol{\gamma}'^T)/2$ such that $\Theta_{ij} = \boldsymbol{\Omega}^T \boldsymbol{\gamma}' \boldsymbol{\Omega} = \boldsymbol{\Omega}^T \boldsymbol{\gamma} \boldsymbol{\Omega}$. By suitably scaling $\boldsymbol{\Omega}$, we can always set $\Theta_{ij} = \pm\pi/4$. Then in the limit of small $|\alpha_j^k|$ (high fidelity), the fidelity can be approximated as

$$\begin{aligned} F &\approx 1 - \frac{4}{5}\sum_k \left(|\alpha_i^k|^2 + |\alpha_j^k|^2\right) \coth\frac{\hbar\omega_k}{2k_BT} \\ &= 1 - \frac{4}{5}\boldsymbol{\Omega}^T \left[\sum_k \left(\boldsymbol{A}_i^{k\dagger}\boldsymbol{A}_i^k + \boldsymbol{A}_j^{k\dagger}\boldsymbol{A}_j^k\right) \coth\frac{\hbar\omega_k}{2k_BT}\right] \boldsymbol{\Omega} \\ &\equiv 1 - \frac{4}{5}\boldsymbol{\Omega}^T \boldsymbol{M} \boldsymbol{\Omega}. \end{aligned} \tag{2.53}$$

By definition, $\boldsymbol{M}$ is a Hermitian matrix, but actually we can express it in a real symmetric form:

$$\begin{aligned} \boldsymbol{\Omega}^T\boldsymbol{M}\boldsymbol{\Omega} &= \frac{1}{2}\left(\boldsymbol{\Omega}^T\boldsymbol{M}\boldsymbol{\Omega} + \boldsymbol{\Omega}^T\boldsymbol{M}^T\boldsymbol{\Omega}\right) \\ &= \frac{1}{2}\left(\boldsymbol{\Omega}^T\boldsymbol{M}\boldsymbol{\Omega} + \boldsymbol{\Omega}^T\boldsymbol{M}^*\boldsymbol{\Omega}\right) \\ &= \boldsymbol{\Omega}^T \mathrm{Re}[\boldsymbol{M}]\boldsymbol{\Omega}. \end{aligned} \tag{2.54}$$

Now we want to minimize $\boldsymbol{\Omega}^T\boldsymbol{M}\boldsymbol{\Omega}$ under the constraint $\boldsymbol{\Omega}^T\boldsymbol{\gamma}\boldsymbol{\Omega} = \pm\pi/4$. For this purpose, we use the method of Lagrange multiplier and consider the optimization of $f(\boldsymbol{\Omega},\lambda) = \boldsymbol{\Omega}^T\boldsymbol{M}\boldsymbol{\Omega} -$

$\lambda(\boldsymbol{\Omega}^T\boldsymbol{\gamma}\boldsymbol{\Omega} \mp \pi/4)$:

$$\begin{cases} \boldsymbol{M}\boldsymbol{\Omega} - \lambda\boldsymbol{\gamma}\boldsymbol{\Omega} = 0 \\ \boldsymbol{\Omega}^T\boldsymbol{\gamma}\boldsymbol{\Omega} = \pm\pi/4 \end{cases} . \tag{2.55}$$

We only need to solve this generalized eigenvalue problem and find the eigenvalue with the smallest absolute value. The corresponding eigenvector, with suitable normalization, gives us the optimal $\boldsymbol{\Omega}$. (See also Appendix A of Ref. [48].)

We remark that for realistic experimental parameters, the effective Rabi frequency cannot be too large. This means that the above optimization should be performed under another inequality constraint. This problem is generally hard to solve, so instead we use the method described above and then discard solutions with unrealistic $|\boldsymbol{\Omega}|$.

2.2 Error Analysis for the Entangling Gate

The gate fidelity realized in the experiment is always less than 1. This is due to the approximations in the formulation, imperfections in the gate design, as well as noise and errors in the experiment. In this section we analyze these sources of errors in detail.

In order to estimate the influence of each error term, we consider a specific example of mapping a 17-qubit surface code for quantum error correction into a linear chain of $^{171}\mathrm{Yb}^+$ ions [2, 49] (see Fig. 2.3 for the mapping). For this purpose, diamond norm may be a better measure of the gate performance, but we focus on average gate fidelity here as it is easier to treat theoretically. We will discuss their difference in Sec. 2.2.3. For realistic parameters, we choose $\omega_x = \omega_y = 2\pi \times 3\,\mathrm{MHz}$, and consider a chain of 19 ions with the two ions at the ends only used for cooling [42]. An anharmonic potential is applied along the z axis, which is specified by $l_0 = 40\,\mu\mathrm{m}$ and $\gamma_4 = 4.3$ (see Sec 2.1.1 for the definition). In this way the

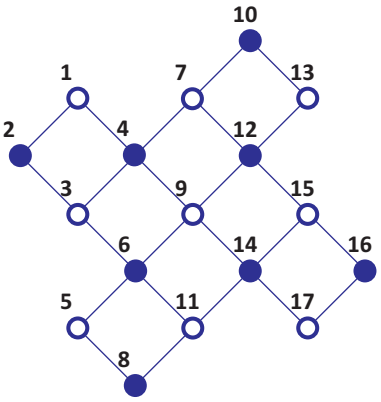

Figure 2.3: A 17-qubit surface code layout. The open circles represent the data qubits and the filled circles represent the syndrome qubits. Labels 1-17 corresponds to the real order of qubits in the 1D chain. (From Ref. [1], ©2018 American Physical Society.)

central 17 ions will have a nearly uniform spacing with an average of $d_{\text{av}} = 8.3\,\mu\text{m}$ and a relative standard deviation of 2.3%.

Under these conditions, the spectrum of the transverse normal modes is very narrow (within 0.9% of ω_x). Hence it is possible to use sideband cooling method to cool the transverse motion down to about 0.5 phonon per mode or less: $k_B T = (\bar{n} + 1/2)\hbar\omega_x = \hbar\omega_x$. Doppler cooling can also be used if the trapping can be stronger. For counter-propagating laser beams along the $\pm x$ directions with $\lambda = 355\,\text{nm}$ [43], we have a detuning $\Delta \approx 2\pi \times 33\,\text{THz}$ and $\Delta k = 2k$. (Actually there are two excited states with a fine-structure splitting of $2\pi \times 100\,\text{THz}$, and the laser detuning is specially chosen to minimize the differential AC Stark shift. We will come back to this point when discussing the AC Stark shift; but otherwise we will just use one value of Δ to estimate the order of magnitude for the other error terms.) The Lamb-Dicke parameter is then $\eta_k \approx 0.11$ for all the transverse modes.

2.2.1 Optimized Gate Design and Sensitivity to Tunable Parameters

In order to perform the stabilizer measurement in the surface code, we need to achieve two-qubit entangling gates between nearest neighbor qubits in Fig. 2.3, that is, ion pairs with one, three and five ion separations in the linear chain. To find the optimal parameters for a high-fidelity gate, we use Eqs. (2.53) and (2.55) to estimate the gate fidelity and to solve the optimal pulse sequence. We then scan the gate time τ, detuning μ and number of segments n_{seg} to find a combination with the desired fidelity.

For example, Fig. 2.4 shows the gate infidelity ($\delta F \equiv 1 - F$) for the entangling gate between ion 1 and ion 4 as a function of detuning μ for a fixed gate time $\tau = 300\,\mu$s and three possible segment numbers $n_{\text{seg}} = 10, 12, 14$. As we can see, increasing the number of segments

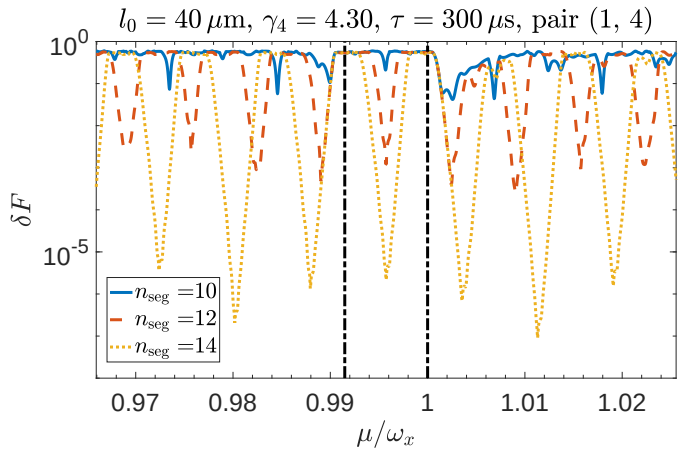

Figure 2.4: Infidelity for an entangling gate between ion 1 and ion 4 as a function of the detuning μ. Here gate time $\tau = 300\,\mu$s and 3 segment numbers $n_{\text{seg}} = 10, 12, 14$ are used. The vertical dash-dot lines give the range of the spectrum of the transverse normal modes. (From Ref. [1], ©2018 American Physical Society.)

generally reduces the gate infidelity. We also notice that there are multiple local minima in

the gate infidelity. Therefore, we do not attempt to find the "best" solution, but rather look for solutions that are "good enough". That is, the solution needs to achieve high gate fidelity in the ideal case, and it should also be robust against errors in these control parameters, which may arise from imperfect calibration, finite resolution or random fluctuation in the experiment. Specifically, we perturb the gate parameters at local minima of plots similar to Fig. 2.4 when scanning these parameters and keep the ones that are most insensitive to the noise. We will assume that these noises are "slow" such that they stay constant during one gate period. This assumption is reasonable because typically the high-frequency noise will be weak in the experiment. For instance, Ref. [50] considers the influence of high-frequency noise in a two-ion crystal and the experimental noise level is found to be about one order of magnitude lower than what is allowed for an error of 10^{-4}. Also note that the same technique to optimize the gate design has been applied in Ref. [2], but the number of segments and the gate time we use here are generally larger because of this additional requirement of robustness.

Below we show the results for ion pairs with three typical separations. For experimentally achievable effective Rabi frequencies, we only present solutions satisfying $|\Omega(t)| < 2\pi \times 1\,\mathrm{MHz}$ at all times.

- Ion 5 and ion 6 (separation 1):

  We use $n_{\mathrm{seg}} = 10$ segments and $\tau = 80.4\,\mu\mathrm{s}$. Laser sequence $\mathbf{\Omega}_0$ is optimized for $\mu_0 = 0.995\omega_x$ (Fig. 2.5). For the sensitivity to control parameters, in Fig. 2.6 we show how the gate infidelity changes under a shift in detuning μ of $2\pi \times 1\,\mathrm{kHz}$, in the global laser intensity $\mathbf{\Omega}$ of 1%, in gate time τ of $0.4\,\mu\mathrm{s}$, as well as the effect of a nonzero $\varphi^{(m)}$. [See Eq. (2.15) for the definition. Here the motional phase is assumed to be equal for

both ions.] For parameters fluctuating inside these ranges, the gate infidelity is always below 10^{-3}.

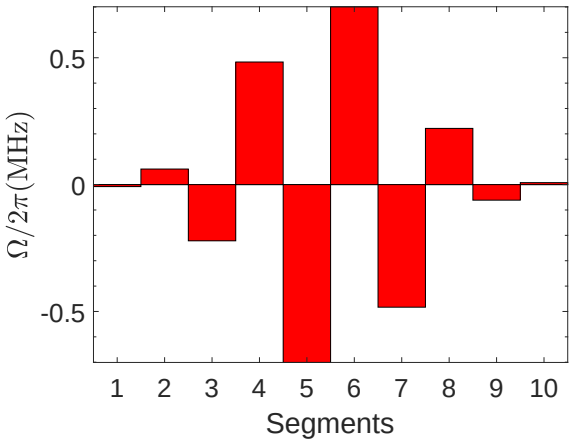

Figure 2.5: Optimized effective Rabi frequency sequence $\mathbf{\Omega}_0$ on ion 5 and ion 6 for $n_{\text{seg}} = 10$, detuning $\mu_0 = 0.995\omega_x$ and gate time $\tau = 80.4\,\mu$s. Here we allow the Rabi frequency to take negative values by adding a phase shift of π. If such a phase shift is not available, we can look for other solutions where all the Rabi frequencies are positive. Some examples are shown in Ref. [2]. (From Ref. [1], ©2018 American Physical Society.)

- Ion 1 and ion 4 (separation 3):

  We use $n_{\text{seg}} = 17$ segments and $\tau = 250\,\mu$s. Laser sequence $\mathbf{\Omega}_0$ is optimized for $\mu_0 = 0.997\omega_x$ (Fig. 2.7), but then for the robustness under fluctuation in detuning (where positive and negative shifts have asymmetric effect), the gate is performed at the detuning $\mu_0' = \mu_0 + 2\pi \times 0.8\,\text{kHz}$ with a slight rescaling of the laser intensity. (See Sec. 2.2.3 for more details about this rescaling, which aims to reduce the accumulation of errors when multiple gates are applied.) Therefore in Fig. 2.8 the smallest infidelity does not always appear at the center of the parameter range.

- Ion 9 and ion 14 (separation 5):

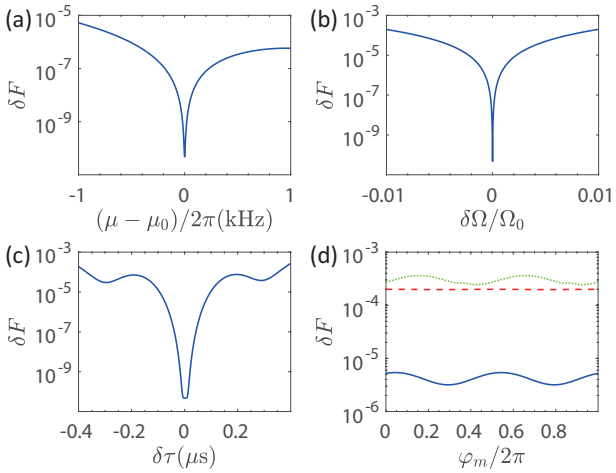

Figure 2.6: Parameter sensitivity for the entangling gate between ion 5 and ion 6. (a) Infidelity as a function of shift in detuning. (b) Infidelity as a function of relative shift in laser intensity. Here we assume that the frequency of the noise is low so that the laser intensities of all the segments are shifted by the same percentage. (c) Infidelity as a function of shift in gate time τ. (d) Dependence on the motional phase $\varphi^{(m)}$. Here we consider $\varphi_i^{(m)} = \varphi_j^{(m)}$ between 0 and 2π. Solid blue, dashed red and dotted green curves are the maximal infidelity for a shift of 1 kHz in detuning μ, a 1% change in Rabi frequency, and $0.4\,\mu$s change in total gate time, respectively. (From Ref. [1], ©2018 American Physical Society.)

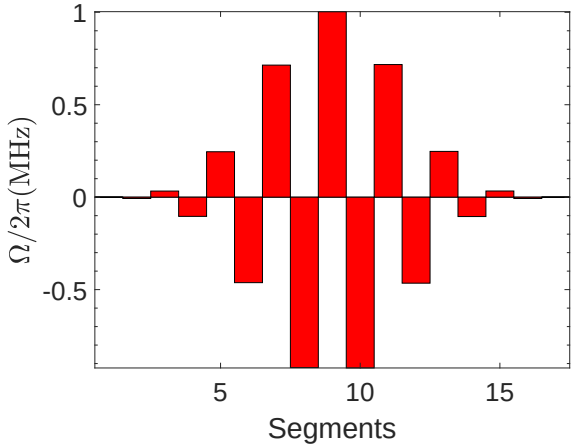

Figure 2.7: Optimized laser sequence $\mathbf{\Omega}_0$ on ion 1 and ion 4 for $n_{\text{seg}} = 17$, detuning $\mu_0 = 0.997\omega_x$ and gate time $\tau = 250\,\mu$s. (From Ref. [1], ©2018 American Physical Society.)

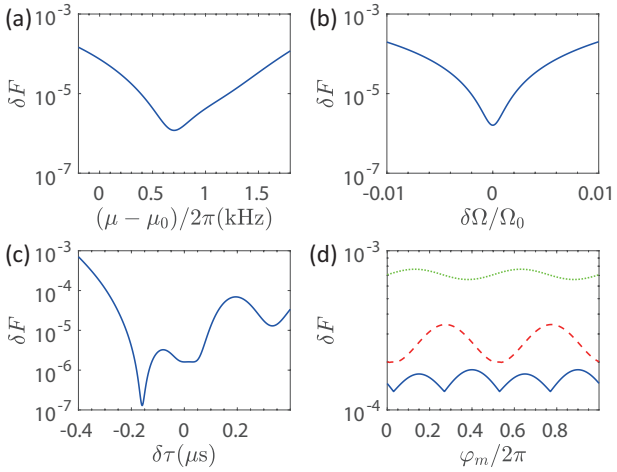

Figure 2.8: Parameter sensitivity for the entangling gate between ion 1 and ion 4. (a) Infidelity as a function of shift in detuning. (b) Infidelity as a function of relative shift in Rabi frequency. We assume the laser intensities of all the segments are shifted by the same percentage. (c) Infidelity as a function of shift in gate time τ. (d) Consider $\varphi_i^{(m)} = \varphi_j^{(m)}$ between 0 and 2π. Solid blue, dashed red and dotted green curves are the maximal infidelity for a shift of 1 kHz in detuning μ, a 1% change in intensity, and 0.4 μs change in total gate time, respectively. (From Ref. [1], ©2018 American Physical Society.)

We use $n_{\rm seg} = 24$ segments and $\tau = 482\,\mu$s. Laser sequence $\mathbf{\Omega}_0$ is optimized for $\mu_0 = 0.997\omega_x$ (Fig. 2.9). For the robustness under fluctuation in parameters, we then work at the detuning $\mu_0' = \mu_0 - 2\pi \times 0.5\,$kHz. Gate infidelity under shifts in parameters are shown in Fig. 2.10.

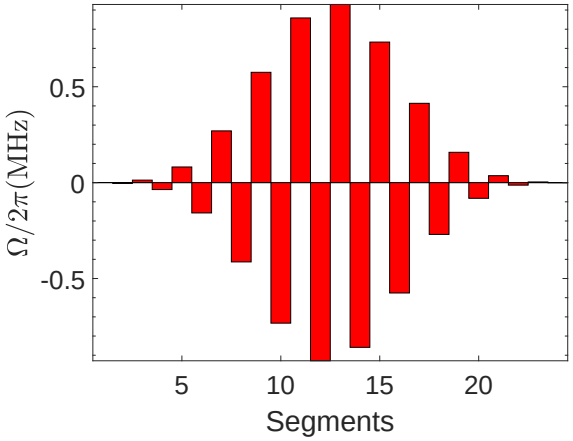

Figure 2.9: Optimized laser sequence $\mathbf{\Omega}_0$ on ion 9 and ion 14 for $n_{\rm seg} = 24$, detuning $\mu_0 = 0.997\omega_x$ and gate time $\tau = 482\,\mu$s. (From Ref. [1], ©2018 American Physical Society.)

As we can see in Figs. 2.6, 2.8 and 2.10, a nonzero but constant $\varphi_i^{(m)} = \varphi_j^{(m)}$ does not influence the fidelity significantly. This justifies the use of the phase-insensitive setup, which suppresses the fluctuation in $\varphi^{(s)}$ but allows $\varphi^{(m)}$ to change over different gates. Nevertheless, we still need to set $\varphi^{(s)} = 0$ initially for the desired XX entangling gate: by taking $U = \exp(i\pi\sigma_i^n\sigma_j^n/4)$ in Eq. (1.8) with small spin phases $\varphi_i^{(s)}$ and $\varphi_j^{(s)}$, we can show that it causes an infidelity $\delta F \approx 2[\varphi_i^{(s)2} + \varphi_j^{(s)2}]/5$. Imbalance between $\varphi_i^{(m)}$ and $\varphi_j^{(m)}$ should also be small: numerically we find that the infidelity scales as $[\varphi_i^{(m)} - \varphi_j^{(m)}]^2$, thus we need $|\varphi_i^{(m)} - \varphi_j^{(m)}| < \pi/100$ for a gate fidelity higher than 99.9%.

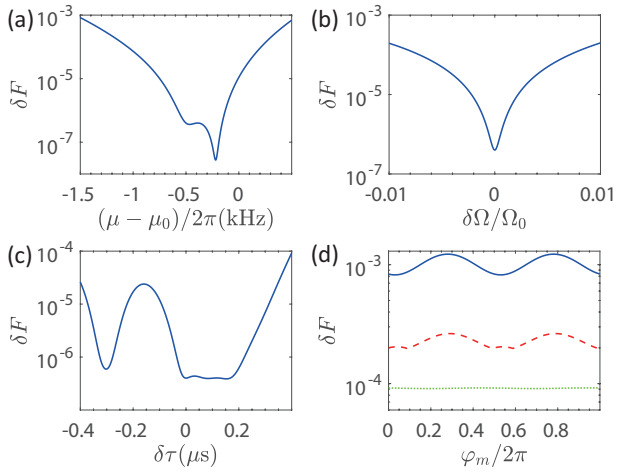

Figure 2.10: Parameter sensitivity for the entangling gate between ion 9 and ion 14. (a) Infidelity as a function of shift in detuning. (b) Infidelity as a function of relative shift in Rabi frequency. (c) Infidelity as a function of shift in gate time τ. (d) Consider $\varphi_i^{(m)} = \varphi_j^{(m)}$ between 0 and 2π. Solid blue, dashed red and dotted green curves are the maximal infidelity for a shift of 1 kHz in detuning μ, a 1% change in intensity, and 0.4 μs change in total gate time, respectively. (From Ref. [1], ©2018 American Physical Society.)

2.2.2 Approximations in the Formulae and Neglected Effects

In order to get the analytical expressions for the gate fidelity [Eqs. (2.48, 2.49, 2.53)], we have made several approximations in the derivation and neglected some physical processes. Some of them are covered along the derivation in Sec. 2.1: for example, to get the effective Hamiltonian Eq. (2.14), we have applied RWA and the adiabatic elimination of the excited state. Their influence can be estimated to be $|\delta|/\omega_{01}$, $|\Omega_{1(2)}|/\omega_{1(2)}$ and $|\Omega_{1(2)}|^2/\Delta^2$. With the Raman transition detuned close to the motional sideband, the first term is about 10^{-4} while the other terms are orders of magnitude smaller. Below we address the effects of other approximations.

Micromotion

For the linear Paul trap, alternating potential is only applied in the x and y directions. Hence there is no micromotion in the z direction. To the first order in trap parameter q, the effect of the transverse micromotion is to replace a_k with $a_k[1-(q/2)\cos\omega_{\rm rf}t]$ when quantizing the transverse modes [20, 51] (see Sec. 3.3 for more details), where $q \approx 2\sqrt{2}\omega_x/\omega_{\rm rf} \sim 0.1$ for the parameters we consider. The effect of the RF-frequency term is $O(\eta_k q\Omega_j/\omega_{\rm rf})$ on α_j^k and $O(\eta_k^2 q\Omega_j/\omega_{\rm rf}) + O(\eta_k^2 q^2\Omega_j/\mu)$ on λ_j^k in Eqs. (2.25, 2.27). Its influence on Θ_{jm} [Eq. (2.28)] is more complex. By comparing terms like

$$\int dt_1 \int dt_2 \sin\mu t_1 \sin\mu t_2 \cos\omega_{\rm rf} t_1 \sin\omega_k(t_1-t_2) \tag{2.56}$$

with the original integration of Eq. (2.28), which is $O(1)$, we estimate the error in Θ_{jm} to be $O(q/\omega_{\rm rf}\tau)$ and $O(q|\mu-\omega_k|/\omega_{\rm rf})$. We also numerically evaluate these correction terms for the three gate designs we consider in Sec. 2.2.1 and get results lower than these estimations. All of these terms are further squared when calculating fidelity, and the dominate contribution is estimated to be 10^{-6} from α_j^k. Nevertheless, the correction factor of $[1-(q/2)\cos\omega_{\rm rf}t]$ can always be incorporated into the formulation if its effect is not negligible, which will be discussed further in Sec. 3.3 for more general ion crystals and a more accurate description of the micromotion.

Carrier term

As is mentioned after Eq. (2.19), in the derivation of the XX entangling gate, we dropped a single-qubit rotation term. Strictly speaking this is not an error source because we can apply an additional rotation to compensate it. However, our numerical result shows that for

all the three gates we considered in Sec. 2.2.1, such single-qubit rotation terms are less than 10^{-5} and can be directly neglected. The reason is that we use multiple laser segments with opposite phases, which largely cancels the single-qubit rotation.

Higher order terms in the Lamb-Dicke parameter

In the derivations of Eqs. (2.20, 2.23 and 2.34-2.37), we only keep zeroth and first order terms in the Lamb-Dicke parameters and the second order diagonal terms with paired a_k and $a_k^\dagger$ of the same motional mode. Here we will show that the error in gate fidelity from such approximations is of the order η^4, and because the Lamb-Dicke parameter η always comes with the operators a_k and $a_k^\dagger$ whose magnitudes are related to the thermal motion, we can express the error as $O(\eta^4(2\bar{n}+1)^2)$, where $\bar{n}$ is the average phonon number of a typical transverse mode.

Let us consider the derivation from Eq. (2.20) to Eq. (2.23). The higher order terms can be divided into four classes:

1. $O(\eta_k^2)$ off-resonant terms with unpaired a_k or $a_k^\dagger$ and a single-qubit rotation, such as

$$\eta_k^2 a_k^2 \sigma_j^n \int dt \Omega_j e^{-2i\omega_k t} \cos(\mu t + \varphi_j^{(m)}) \tag{2.57}$$

   and

$$\eta_k \eta_l a_k a_l^\dagger \sigma_j^n \int dt \Omega_j e^{-i(\omega_k - \omega_l)t} \cos(\mu t + \varphi_j^{(m)}) \tag{2.58}$$

   for $k \neq l$, where numerical factors of the order 1 are omitted. These terms have vanishing expectation values in a thermal state and therefore they contribute to the gate fidelity only when pairing with another two creation or annihilation operators.

Hence the error is $O(\eta_k^4)$. Also notice that for the example we considered in Sec. 2.2.1, the spectrum of the transverse modes is narrow and all the ω_k's are similar and are also close to μ. Therefore the time integral is of the order $\Omega_j/\omega_k \lesssim 1$.

2. $O(\eta_k^3)$ resonant terms with unpaired a_k or $a_k^\dagger$ and a single-qubit rotation, such as

$$\eta_k\eta_l\eta_m a_k^\dagger a_l^\dagger a_m \sigma_j^n \int dt\Omega_j e^{i(\omega_k+\omega_l-\omega_m)t}\sin(\mu t+\varphi_j^{(m)}). \tag{2.59}$$

We consider two possible cases here. (i) Two frequencies are the same, e.g. $\omega_l = \omega_m$. Then the time integration has exactly the same form as Eq. (2.25). According to Eq. (2.53), as we optimize the gate fidelity to higher than 99.9%, each $|\alpha_j^k|^2$ term should be of the order 10^{-3} or less. Besides, the term we drop here has an additional η_k^2 coefficient compared with α_j^k. (ii) All the three frequencies are different. For a wide spectrum, such terms become off-resonant and can be treated in a similar way as $O(\eta_k^2)$ terms; for a narrow spectrum we considered in Sec. 2.2.1, that is, 19 transverse modes located within a width of about 0.9% of ω_x, such a term has a shifted ω_k compared with Eq. (2.25), hence its contribution should be similar to a shifted detuning μ by the same amount, with the additional η_k^2 factor. To sum up, such terms have negligible effects so long as the gate fidelity calculated by Eq. (2.53) is high at the optimized parameters and is robust against shift in detuning. To balance the creation and annihilation operators when taking the trace with a thermal state, this type of terms can be paired with the first order terms as well, which, however, vanish for the optimized parameters.

3. $O(\eta_k^3)$ off-resonant terms with unpaired a_k or $a_k^\dagger$ and a two-qubit operation, such as the time integral of the commutator between one first order term and one second order term. To balance the creation and annihilation operators, another $O(\eta_k)$ term must

be added. So the final contribution is $O(\eta_k^4)$.

4. $O(\eta_k^4)$ resonant terms with a two-qubit operation, such as the time integral of the commutator between two second order terms, or that between one first order term and one third order term. Such terms lead to a relative error of $O(\eta_k^2)$ in Θ_{ij} of Eq. (2.28). Whether the creation and annihilation operators are balanced or not, an error of $O(\eta_k^4)$ in the fidelity is resulted, because Θ_{ij} is set to be $\pi/4$ in Eq. (2.48) and the error only appears as a quadratic term.

Since only two ions appear in the Hamiltonian [Eq. (2.20)] and $(\sigma_j^n)^2 = I$, there are no multi-qubit operation terms. There are also terms purely in the subspace of motional states, e.g. the commutator between two first order terms with the single-qubit rotation on the same ion. However, such terms act as a global phase on the subspace of the ions' internal states and are irrelevant to the gate fidelity.

Similar arguments also apply to Eqs. (2.34-2.37): $O(\eta_k^2)$ terms with unpaired creation or annihilation operators or $O(\eta_k^3)$ terms cause an error of $O(\eta_k^4)$ in fidelity and therefore can be neglected. In the derivation of these equations, we use the Zassenhaus Formula [45]:

$$e^{X+Y} = e^X e^Y e^{-\frac{1}{2}[X,Y]} \times \cdots \tag{2.60}$$

After dropping the commutators, which are higher order terms based on the argument above, we obtain Eqs. (2.34-2.37).

Asymmetry in blue- and red-detuned coupling

In the derivation of Eq. (2.15), we assume the two pairs of Raman transitions on one ion have the same effective Rabi frequency and opposite detunings (see Fig. 2.2). However, in experiments there are always errors in these parameters, which can significantly influence the gate fidelity. Here we discuss the influence of small asymmetry in the phase-insensitive geometry. A similar analysis can also be applied to the phase-sensitive one.

Suppose one Raman transition pair has effective Rabi frequency $\Omega_j + \delta\Omega_j$ and detuning $\mu + \delta\mu$, while the other pair has effective Rabi frequency $\Omega_j - \delta\Omega_j$ and detuning $-\mu + \delta\mu$. Following similar steps as in Eq. (2.15), we get the effective interaction-picture Hamiltonian

$$\begin{aligned} H_I =& \hbar\Omega_j \cos[\mu t + \varphi_j^{(m)} - \Delta k \cdot x_j(t)] \left[\sigma_j^x \cos(\delta\mu \cdot t + \varphi_j^{(s)}) - \sigma_j^y \sin(\delta\mu \cdot t + \varphi_j^{(s)})\right] \\ & - \hbar\delta\Omega_j \sin[\mu t + \varphi_j^{(m)} - \Delta k \cdot x_j(t)] \left[\sigma_j^x \sin(\delta\mu \cdot t + \varphi_j^{(s)}) + \sigma_j^y \cos(\delta\mu \cdot t + \varphi_j^{(s)})\right]. \end{aligned} \tag{2.61}$$

Clearly $\delta\mu$ produces a slow change in the rotation axis and its effect (for small $\delta\mu \cdot \tau$) can be bounded by that of a constant error in $\varphi_j^{(s)}$. So the error from asymmetric detuning is $O(\delta\mu^2\tau^2)$ where τ is the gate time.

The $\delta\Omega_j$ term corresponds to a rotation in the orthogonal direction, which oscillates at the same frequency as the leading order term but with a phase difference of $\pi/2$. It is more difficult to bound this effect. So instead we tackle this problem numerically. A multiple-phonon-mode problem is still hard to solve, even for a relatively small cutoff of phonon numbers; but for only two ions and one phonon mode, the system can be easily solved by standard numerical integration methods, using a Hamiltonian analogous to Eq. (2.14) with two pairs of Raman transitions on each of the ion. Then the result can be compared with the

method we used in Sec. 2.1. Since our purpose is just to estimate the order of magnitude, we choose a special initial state $|00\rangle\langle 00| \otimes \rho_{\text{th}}$ to calculate fidelity.

For symmetric detunings and effective Rabi frequencies, the result is consistent with the error analysis we made in the previous subsection, namely a discrepancy of the order η^4. For a nonzero $\delta\Omega_j$, it turns out that the dominant source of error is the additional rotation due to the carrier term of the Hamiltonian, i.e.,

$$H_I^{\text{carrier}} = \hbar\Omega_j\sigma_j^x \cos\mu t - \hbar\delta\Omega_j\sigma_j^y \sin\mu t, \tag{2.62}$$

where we choose $\varphi_j^{(m)} = \varphi_j^{(s)} = 0$ and $\delta\mu = 0$ for simplicity. Originally the carrier term almost vanishes for the optimized gate parameters; but now with the $\delta\Omega_j$ term, the carrier term leads to an additional small rotation, which causes errors in the final entangling gate.

With this observation, we can now estimate the influence of asymmetric effective Rabi frequencies in the gates we considered in Sec. 2.2.1. All we need to do is to numerically solve the unitary evolution operator corresponding to the carrier term of the Hamiltonian [Eq. (2.62)], given the pulse sequence $\mathbf{\Omega}$ from Sec. 2.2.1. It must be a single-qubit rotation, and the rotation angle $\delta\phi$ indicates that the error in gate fidelity is of the order $\delta\phi^2$. Supposing the intensities of different laser beams are proportional, we have $\delta\Omega(t) = \epsilon\Omega(t)$ where ϵ is a small parameter. Plugging in the gate parameters, we need $\epsilon < 0.1\%$ for ion 5 and ion 6, $\epsilon < 0.02\%$ for ion 1 and ion 4, and ion 9 and ion 14, to achieve a gate fidelity higher than 99.9%. Note that the gate design is robust against global shift of the laser intensity, and our scheme does not require the same laser driving on the two ions; it is the relative change between the two Raman transition pairs on the same ion that causes this type of error. Usually the multiple laser beams used in the experiment are separated from a single laser through beam splitters,

hence it is possible to control the relative difference in their intensity and frequencies to be small, even though the laser itself is fluctuating.

Finally, we also use this method to estimate the effect of the asymmetry in Δk, which is about the ratio of the hyperfine splitting to the laser frequency, as is discussed in Sec. 2.1.2. It turns out that this error is negligible for the parameters we choose.

AC Stark shift

The counter-rotating or off-resonant couplings neglected before not only introduce fluctuations between the two qubit states, but also cause a shift in the energy levels, which is known as the AC Stark shift. For $^{171}Yb^+$ ions, the 355 nm laser is particularly chosen to reduce the relative shift between the two hyperfine ground states, a.k.a. the differential AC Stark shift. According to Ref. [43], the differential Stark shift is only about 10^{-4} of the effective coupling Ω_{eff} between $|0\rangle$ and $|1\rangle$. However, such a relative shift in the energy levels does not correspond to a shift $\delta\mu$ in the Hamiltonian [Eq. (2.15)], to which our gate design is not sensitive; instead it will increase the asymmetry between the two Raman transition pairs and, as we have mentioned above, will lead to an infidelity of $(\delta\mu_{\text{asym}}\tau)^2$. A constant AC Stark shift can be easily compensated by a corresponding shift in the driving laser's frequencies, but in our case the intensities of the driving laser are also varying. One possible solution is to tune the laser frequencies for each segment accordingly. Another possibility is to use one strong beam and one weak beam for each Raman transition, and only to adjust the weak beam to change the effective coupling strength. For example, in Fig. 2.2 we can make the lower beam stronger than the upper one, while still balance the effective Rabi frequencies of the two Raman transitions. By letting the strong beam 10 times as the weak one, we can reduce the changes in AC Stark shift to 1/10 while keeping the effective coupling unchanged.

Spontaneous emission

So far we have not considered the spontaneous emission from the excited state. To couple the two ground states with the off-resonant Raman transition, there is actually a small probability of $\Omega_{1(2)}^2/\Delta^2$ for the ion to be in the excited state, from which the spontaneous emission can occur at the rate of γ_e. This will lead to decoherence between the two qubit states. To estimate its effect, we simply time-integrate $\gamma_e(\Omega_1^2 + \Omega_2^2)/\Delta^2$ over the whole laser sequence. For the gate design we considered in Sec. 2.2.1, the error from spontaneous emission is thus computed to be 10^{-3} for the longest gate time of about $500\,\mu$s, if we set $\Omega_1 = \Omega_2$. Note that if we use one strong and one weak beams for Raman transition to reduce the change in AC Stark shift, as described above, the spontaneous emission error will be dominated by the stronger beam and hence will be increased.

Crosstalk of Laser Driving

A broad laser beam can cause unwanted transitions on the adjacent ions, while a narrow beam can lead to fluctuation in the laser intensity felt by the target ion due to its thermal motion. Suppose the laser beams have a Gaussian profile, that is, the intensity is proportional to $\exp(-r_\perp^2/2\sigma^2)$ where σ is the width of the beam. With $\sigma = 2\,\mu$m, when a beam is shined on one ion, its effect on an adjacent ion is of the order $\exp(-d_{\rm av}^2/2\sigma^2) \sim 10^{-4}$. (Actually the intensity of the electric field, i.e. Rabi frequency, is only the square root of the laser power; but we get a further square when computing the fidelity.) Meanwhile, the thermal motion perpendicular to the laser beam is dominated by that in the axial z direction. For a harmonic trap at the temperature of T, the axial oscillation amplitude can be estimated to be $\Delta z \sim \sqrt{k_B T/m\omega_z^2}$. The temperature is related to the phonon number

$\bar{n}$ in the transverse direction by $k_B T = \hbar\omega_x(\bar{n} + 1/2)$. We can further use the Lamb-Dicke parameter $\eta = 2(2\pi/\lambda)\sqrt{\hbar/2m\omega_x}$ for counter-propagating laser beams with wavelength λ, and finally we estimate the fluctuation of the laser intensity on the ion due to its thermal motion as $\Delta z^2/2\sigma^2 \sim (1/32\pi^2)\eta^2(2\bar{n}+1)(\lambda/\sigma)^2(\omega_x/\omega_z)^2$. To realize a linear trap along the z direction, we need $\omega_x/\omega_z > 0.77N/\sqrt{\log N}$ [42,52,53] for a harmonic trap; the estimation for anharmonic trap is more difficult but the scaling should not be worse. Therefore the noise on the laser intensity due to thermal motion is of the order 10^{-4} for a chain of tens of ions; while the gate design can tolerate a fluctuation of 1%.

Fluctuation in Trapping Potential

The trapping parameters $\omega_{x(y,z)}$ are also subjected to experimental noise. It has mainly two effects: (1) a shift in phonon mode frequencies (phonon mode dephasing), whose effect is roughly the same as an opposite shift in detuning μ and (2) small change in the equilibrium configuration, whose effect depends on the width of each laser beam. Because we are considering a linear chain of ions, small change in the transverse potential will not change the equilibrium positions, but only shift the transverse mode frequencies. Therefore, our examples of gate design are able to tolerate $2\pi \times 1\,\mathrm{kHz}$ shift in the transverse trapping frequencies while still maintains a fidelity of 99.9%. The weaker axial trapping is achieved by a DC field, hence less vulnerable to fluctuations. For an estimation, we again consider a harmonic potential ω_z. The dimension of length appears as $(q^2/4\pi\epsilon_0 m\omega_z^2)^{1/3}$, hence $\delta z/z \sim -2\delta\omega_z/3\omega_z$. For N ions in the linear chain, the largest change in equilibrium position is for ions on the end, with $z = Nd_{\mathrm{av}}/2$. Now if we want the change in the laser intensity to be less than 1% for an ion, i.e. $1 - \exp(-\delta z^2/2\sigma^2) \approx \delta z^2/2\sigma^2 \sim 1\%$, we get $\delta\omega_z/\omega_z \sim 0.5\sigma/Nd_{\mathrm{av}} \approx 0.5\%$, that is, our gate design can tolerate a relative change of 0.5% in the axial frequency. Actually

large shift during one gate time is not very likely; usually trapping parameters vary in a much longer time scale and in principle we can adjust the laser beams before the experiment to compensate such a long-term effect.

Motional Heating

We have assumed that the ion chain is sideband cooled to a low temperature before the experiment and stays there. Now we consider the effect of heating in the motional modes, which varies with the trap design. According to Eq. (2.55), our optimization process is not sensitive to the phonon numbers if they stay constant. Hence the infidelity due to the motional heating can be bounded by the "failure rate" as $\delta F_{\text{heating}} < N\Gamma\tau$ where N is the number of the transverse modes in use, τ the gate time and Γ the average heating rate. Currently it is possible to realize a heating rate around 1 phonon/s for our choice of $^{171}\text{Yb}^+$ ion and transverse mode frequencies around $2\pi \times 3\,\text{MHz}$ [32, 54]. Hence the error is bounded by $\delta F_{\text{heating}} < 10^{-2}$ for $N = 19$ and $\tau = 500\,\mu\text{s}$, but note that this is not a tight bound. For one thing, as is mentioned in Sec. 1.2.2, the dominant heating source through electric noise mainly heats the center-of-mass mode of the ion crystal. Therefore when the size of the crystal is smaller than the wavelength of the electric noise, the heating rate may not significantly rely on the number of the ions. For another, when we conduct a similar numerical simulation as that for the asymmetry of Raman transitions for two ions and one motional mode, with an additional Lindblad term describing the heating, we find that the infidelity does scale linearly with the heating rate, but the value is about 2 orders of magnitude smaller. Meanwhile, the use of multiple segments should further reduce the error. Therefore we believe that the motional heating is not a dominant source of error for tens of ions.

Nonlinear Interaction

Another effect not covered is the Kerr coupling, i.e. the dependence of one mode's frequency on the phonon number of another mode due to the nonlinearity in the Coulomb interaction [55]. It can be calculated by expanding the Coulomb potential to the fourth order. Numerically we find that for the ion chain we use, the largest coupling is about 0.14 Hz/phonon between a transverse mode and an axial mode, and about 0.02 Hz/phonon between two transverse modes. The error due to a constant shift in a mode frequency ω_k can be estimated by that in the detuning μ, because if we apply RWA to Eq. (2.25) and Eq. (2.28), only the difference between μ and ω_k influences the final fidelity [Eq. (2.48)]. Because our scheme can tolerate such a shift up to 1 kHz, we conclude that the Kerr coupling has negligible effects for the examples we are considering.

2.2.3 Coherent vs Incoherent Errors

Up to now we have been using average gate fidelity to evaluate the gate performance, because it is easier to treat theoretically and also easier to measure experimentally through randomized benchmarking [56]. However, it is well-known that high gate fidelity does not immediately imply a low enough error rate, or more precisely the diamond norm, which appears in the statement of the Quantum Threshold Theorem [14, 57]. In certain cases these two measures can differ significantly, especially for coherent errors. Since we have motivated our analysis by fault-tolerant quantum computing, it is worthwhile to discuss the relation between our results and the diamond norm.

The error sources we considered in Sec. 2.2.2 can be divided into two classes. The effects of the micro-motion, RWA and the higher order terms in Lamb-Dicke parameters should be

mainly unitary because the approximations are directly made in the Hamiltonian. They are estimated to be $O(10^{-4})$ or less, hence the diamond norm should be of order $O(10^{-2})$. On the other hand, spontaneous emission and other errors related to the thermal motions should be incoherent and the diamond norm will not be very different from the infidelity [14].

The parametric shifts that we considered in Sec. 2.2.1 are generally unitary errors. For this type of error it is known that the diamond norm D scales as $\sqrt{\delta F}$ [14], hence our criteria of $\delta F < 10^{-3}$ will give a diamond norm of about 3×10^{-2} in the worst case. Actually as we have already derived the expression of the density matrix [Eq. (2.39)], we can numerically evaluate the diamond norm using semidefinite programming [16,58]. The results for the gate designs we considered in Sec. 2.2.1 are shown in Figs. 2.11, 2.12 and 2.13. As expected, the diamond norms at the extreme shifts reach the order of $O(10^{-2})$ and are slightly above the threshold of the surface code of about 1%, although for the small system we are considering, it is more meaningful to compare with the pseudothreshold, which is about 8×10^{-4} for the Surface-17 code [49]. This suggests that better controls on the parameters are needed for low enough error rates. Similarly, we expect the bounds on the asymmetry of the beam configurations and the mismatched laser phases to be tighter, as they are also coherent errors. Note however that diamond norm is usually a pessimistic estimation of the errors, and 99.9% fidelity is nevertheless a good target in practice for many near-term applications of quantum computation.

Accumulation of Gate Design Error

Another observation from Figs. 2.11, 2.12 and 2.13 is that the error from the imperfect gate design, when there is no parametric shifts, has similar values measured by the infidelity and the diamond norm. This suggests that this gate design error is incoherent and will

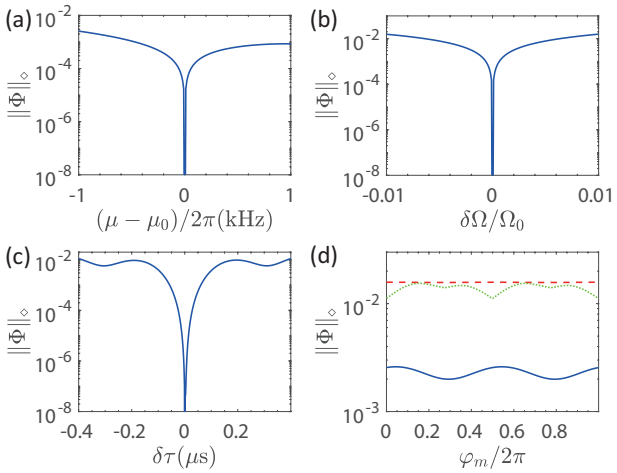

Figure 2.11: Parameter sensitivity for the entangling gate between ion 5 and ion 6. (a) Diamond norm as a function of shift in detuning. (b) Diamond norm as a function of relative shift in Rabi frequency. (c) Diamond norm as a function of shift in gate time τ. (d) Consider $\varphi_i^{(m)} = \varphi_j^{(m)}$ between 0 and 2π. Solid blue, dashed red and dotted green curves are the maximal diamond norm for a shift of 1 kHz in detuning μ, a 1% change in intensity, and 0.4 μs change in total gate time, respectively. For (a), (b) and (c), the diamond norms below 10^{-8} are not shown, since they are subject to numerical errors. (From Ref. [1], ©2018 American Physical Society.)

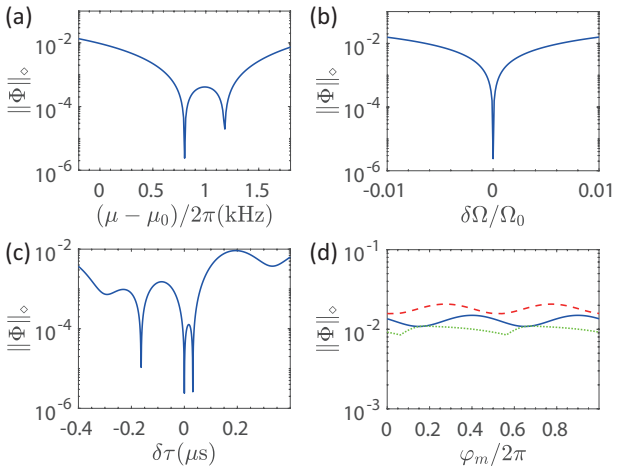

Figure 2.12: Parameter sensitivity for the entangling gate between ion 1 and ion 4. (a) Diamond norm as a function of shift in detuning. (b) Diamond norm as a function of relative shift in Rabi frequency. (c) Diamond norm as a function of shift in gate time τ. (d) Consider $\varphi_i^{(m)} = \varphi_j^{(m)}$ between 0 and 2π. Solid blue, dashed red and dotted green curves are the maximal diamond norm for a shift of 1 kHz in detuning μ, a 1% change in intensity, and 0.4 μs change in total gate time, respectively. (From Ref. [1], ©2018 American Physical Society.)

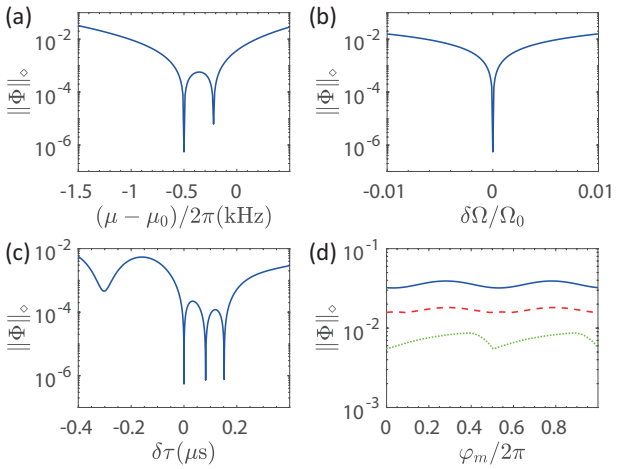

Figure 2.13: Parameter sensitivity for the entangling gate between ion 9 and ion 14. (a) Diamond norm as a function of shift in detuning. (b) Diamond norm as a function of relative shift in Rabi frequency. (c) Diamond norm as a function of shift in gate time τ. (d) Consider $\varphi_i^{(m)} = \varphi_j^{(m)}$ between 0 and 2π. Solid blue, dashed red and dotted green curves are the maximal diamond norm for a shift of 1 kHz in detuning μ, a 1% change in intensity, and 0.4 μs change in total gate time, respectively. (From Ref. [1], ©2018 American Physical Society.)

scale linearly with the number of gates. It is understandable because in our derivation of Eq. (2.39) we have traced out the phonon modes after applying the gate, and hence the coherence is lost. In other words, we assume no memory effect of the phonon modes, namely the Markovian approximation for the sequential application of the entangling gates.

This is a reasonable assumption because the phonon modes naturally decohere over long evolution time. Furthermore, we will now show that even if the coherence time of the phonon modes is longer than the separation of the gates, the gate design error still accumulates linearly if we introduce small randomness in their separations.

In our formulation, the effect of multiple gates on the same pair of two ions can be easily modelled as a longer pulse sequence. Suppose we have m gates starting at T_1, $T_2, \cdots, T_m$ respectively, with $T_1 < T_1 + \tau \leq T_2 < T_2 + \tau \leq \cdots \leq T_m < T_m + \tau$ where τ is the gate time. Then Eq. (2.25) and Eq. (2.29) should be modified to

$$\begin{aligned}\alpha_j^k =& -\frac{i}{\hbar}\eta_k b_j^k \int_{T_1}^{T_1+\tau} \chi_j(t) e^{i\omega_k t} dt - \frac{i}{\hbar}\eta_k b_j^k \int_{T_2}^{T_2+\tau} \chi_j(t) e^{i\omega_k t} dt - \cdots \\ & - \frac{i}{\hbar}\eta_k b_j^k \int_{T_m}^{T_m+\tau} \chi_j(t) e^{i\omega_k t} dt, \end{aligned} \tag{2.63}$$

and

$$\begin{aligned}\Theta_{ij} =& \frac{2}{\hbar^2}\sum_k \eta_k^2 b_i^k b_j^k \Bigg\{ \Bigg(\int_{T_1}^{T_1+\tau} dt_1 \int_{T_1}^{t_1} dt_2 \\ & + \int_{T_2}^{T_2+\tau} dt_1 \int_{T_1}^{T_1+\tau} dt_2 + \int_{T_2}^{T_2+\tau} dt_1 \int_{T_2}^{t_1} dt_2 \\ & + \cdots \\ & + \int_{T_m}^{T_m+\tau} dt_1 \int_{T_1}^{T_1+\tau} dt_2 + \cdots + \int_{T_m}^{T_m+\tau} dt_1 \int_{T_m}^{t_1} dt_2 \Bigg) \chi_i(t_1)\chi_j(t_2) \sin\left[\omega_k(t_1 - t_2)\right] \Bigg\}. \end{aligned} \tag{2.64}$$

Changing the starting point of the gate within a range of $2\pi/\omega_x$, which is much shorter than the gate time τ, will introduce a fully random phase factor to each term in α_j^k. This ensures a $\sqrt{m}$ scaling for each α_j^k as random walks on the complex plane, and hence the accumulated infidelity of m gates, which is proportional to $\sum_{jk} |\alpha_j^k|^2(2n_k+1)$ [see Eq. (2.53)], will scale as m instead of m^2. Besides, the varying starting point of the integration in α_j^k also leads to a varying motional phase $\varphi_j^{(m)}$ for each gate. In Sec. 2.2.1 we optimize the gate parameters at $\varphi_j^{(m)} = 0$ for both ions, but later in Fig. 2.14 we will show that these gate designs are robust for a nonzero motional phase.

Now we consider the Θ_{ij} term. First note that any double integrals involving two gates will vanish in Eq. (2.64), because then these integrals have a similar form as those in α_j^k and are suppressed by our optimization. The error from these terms will further be squared when computing the fidelity, hence can be safely neglected. Then we are left with m double integrals, each corresponding to an individual gate. Here a random motional phase will also appear due the the varying starting points of the gates. Ideally each double integral should be $\pm\pi/4$ and the total phase $\pm m\pi/4$, but the random motional phase will cause a distribution of the integral. To suppress the accumulated error, we set the mean of this distribution at $\pm\pi/4$, assuming a uniform distribution of the motional phase over $[0, 2\pi)$. Then the deviation of the sum of the m gates from $\pm m\pi/4$ will be $O(\sqrt{m})$ and therefore the infidelity will scale as m.

As an example, we plot the infidelity due to α_j^k terms (residual coupling to the phonon modes) in Fig. 2.14 and the value of Θ_{ij} in Fig. 2.15 as functions of the motional phase $\varphi_j^{(m)}$. These plots are computed from our gate design for ion 9 and ion 14, where first we determine the shape of the pulse sequence at the detuning $\mu_0 = 0.997\omega_x$, then we move to the working point $\mu_0' = \mu_0 - 2\pi \times 0.5\,\mathrm{kHz}$ and rescale the pulse intensity to set $\Theta_{ij} = \pm\pi/4$. These

parameters are the same as those used to get Fig. 2.10. As we can see, the residual coupling to the phonon modes is very insensitive to the motional phase. We should further rescale the pulse sequence to move the mean of Fig. 2.15 to -1, so that the infidelity accumulates as $O(m)$.

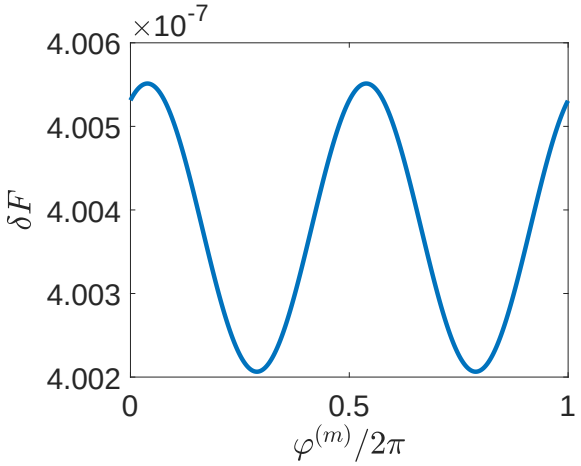

Figure 2.14: Infidelity due to residual coupling to the phonon modes vs. motional phase $\varphi^{(m)}$. The pulse sequence is optimized for $\varphi^{(m)} = 0$, but the infidelity is almost independent of $\varphi^{(m)}$. (From Ref. [1], ©2018 American Physical Society.)

Finally we show an example of applying repeated gates by setting $T_i + \tau = T_{i+1}$ ($i = 1, 2, \cdots, m-1$). The gate infidelity due to the imperfect design vs. m is plotted in Fig. 2.16. No clear accumulation in the gate infidelity is observed, partially because the starting point of each gate is not randomly chosen. Nevertheless, we expect the accumulated error to be $O(m)$ rather than $O(m^2)$.

We should emphasize that with the existence of spontaneous emission, phonon mode dephasing and heating, the above formulation will finally break down as $m\tau$ goes above the coherence time. The purpose of this discussion here is just to show that the gate design error is not a dominant source in our scheme even if multiples gates are applied.

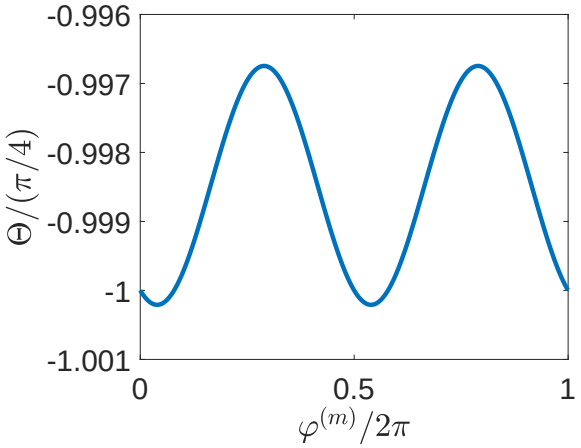

Figure 2.15: XX rotation angle Θ_{ij} vs. motional phase $\varphi^{(m)}$. The pulse sequence is chosen such that $\Theta_{ij} = \pm\pi/4$ at $\varphi^{(m)} = 0$. A further rescaling is needed to shift the average of this curve to -1 if we assume a uniform distribution of the motional phase over $[0, 2\pi)$. (From Ref. [1], ©2018 American Physical Society.)

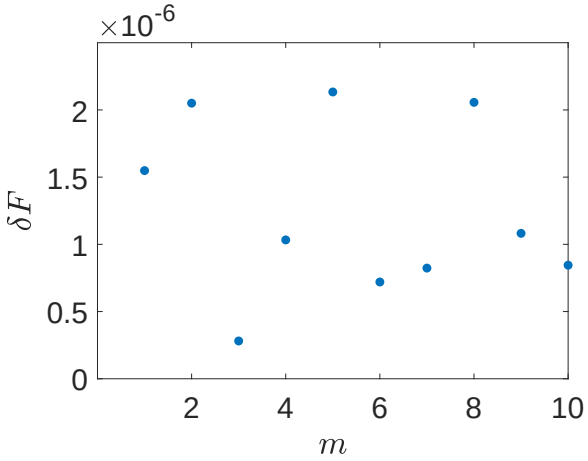

Figure 2.16: Total gate design infidelity vs. number of repeated gates m between ion 9 and ion 14. Here we consider a special case where there is no interval between two adjacent gates. (From Ref. [1], ©2018 American Physical Society.)

2.2.4 Summary and Discussion

We summarize in Table 2.1 the requirements on the relevant parameters for a gate fidelity higher than 99.9%, and in Table 2.2 the error from terms and effects neglected in the

Table 2.1: Restriction on fluctuations or errors in physical parameters for $F > 99.9\%$.

Source of Error	Requirement
Slow fluctuation in μ	$\lvert\delta\mu\rvert < 1\,\mathrm{kHz}$
Slow fluctuation in Ω	$\lvert\delta\Omega/\Omega_0\rvert < 1\%$
Error in gate time τ	$\lvert\delta\tau\rvert < 0.4\,\mu\mathrm{s}$
Detuning asymmetry in phase-insensitive setup	$\lvert\delta\mu_{\mathrm{asym}}\rvert < 10\,\mathrm{Hz}$
Rabi frequency asymmetry in phase-insensitive setup	$\lvert\delta\Omega_{\mathrm{asym}}/\Omega_0\rvert < 0.02\%$
Phase asymmetry on the two ions	$\lvert\varphi^{(m)}_{\mathrm{asym}}\rvert < \pi/100$
Nonzero $\varphi^{(s)}$	$\lvert\varphi^{(s)}\rvert < \pi/100$
Laser's phase fluctuation during one gate time	$\lvert\delta\varphi\rvert < \pi/100$
Change in trapping frequencies	$\lvert\delta\omega_x\rvert < 1\,\mathrm{kHz}$ $\lvert\delta\omega_z/\omega_z\rvert < 0.5\%$

derivation. As we can see, the most prominent technical challenge in realizing a high-fidelity entangling gate is to compensate any imbalance in the two Raman transition pairs to couple the qubit states; they require very careful control in the frequencies, intensities and beam profiles of the laser.

In comparison, errors from spontaneous emission of the excited state, which is right at the order of 0.1% in our examples of gate design, seems to set an ultimate limitation: we note that the error from spontaneous emission is proportional to the effective Rabi frequency $\mathbf{\Omega}$ (if two beams of the Raman transition have the same intensity) and the total gate time τ. If one is reduced, the other should be increased to realize the desired entangling gate and therefore

Table 2.2: Errors from neglected terms and effects. In this table, q is a parameter of the Mathieu equation describing the Paul trap (see Sec. 1.2.1); γ_e the spontaneous emission rate of the excited state $|e\rangle$; Ω_1 and Ω_2 the Rabi frequencies corresponding to any Raman transition pair and Ω_{eff} the resulting effective coupling between $|0\rangle$ and $|1\rangle$; d_{av} the average ion spacing; σ the width of each laser beam. See the main text for the definition of other symbols. The last column gives an estimation of the order of magnitude based on the chosen experimental parameters.

Source of Error	Expression	Value
Micromotion	$(\eta q \Omega_{\text{eff}}/\omega_{\text{rf}})^2$	10^{-6}
RWA	$\lvert\delta\rvert/\omega_{01},\ \lvert\Omega_{1(2)}\rvert/\omega_{1(2)}$	10^{-4}
Adiabatic elimination of the excited state	$\lvert\Omega_{1(2)}\rvert^2/\Delta^2$	10^{-7}
Spontaneous emission of the excited state	$\gamma_e \tau \lvert\Omega_{1(2)}\rvert^2/\Delta^2$	10^{-3}
Higher order terms in Lamb-Dicke parameter η	$\eta^4(2\bar{n}+1)^2$	10^{-4}
Laser beams on adjacent ions	$\exp(-d_{\text{av}}^2/2\sigma^2)$	10^{-4}
Thermal motions perpendicular to the laser beams	$\frac{\eta^2(2\bar{n}+1)}{32\pi^2}\left(\frac{\lambda}{\sigma}\right)^2\left(\frac{\omega_x}{\omega_z}\right)^2$	10^{-4}

the error does not decrease. However, what we presented in Sec. 2.2.1 are not the shortest possible gate time and weakest possible Rabi frequency: when optimizing parameters such as $\mathbf{\Omega}$ and τ, we have considered the robustness against fluctuation in parameters. If these fluctuations can be further suppressed, we can use other solutions with shorter gate time and weaker laser intensity [2], then the infidelity from spontaneous emission can be reduced. Also note that in the above estimation we use a detuning Δ corresponding to the 355 nm laser for $^{171}Yb^{+}$ ions. The spontaneous emission error will decrease if we use larger $|\Delta|$ [32], although then we will have larger differential AC Stark shift [43].

Finally, for the current example we are considering with a few tens of ions, effects of thermal motion and heating are not dominant; but as these effects scale with the ion number N, we will need better way to cool the ion chain and to isolate it from the environment when we proceed to larger scale ion trap quantum computing.

Chapter 3

Scalability of Ion Trap Quantum Computing

Although the method we studied in the previous chapter works for a multi-ion crystal, the number of phonon modes scales linearly with the number of ions and hence it becomes more and more difficult to suppress all the residue entanglement between the qubit states and the phonon modes. Besides, in large ion crystals (possibly 2D or 3D) the micromotion cannot be neglected. In this sense, it is not clear whether this approach for gate design can be applied to a system of thousands to millions of ions. In this chapter, we will address this problem of scalability. First we will consider numerical methods to solve ions' (classical) motions and examine the stability of a large crystal in Sec. 3.1. Then a scalable way to design and to apply the entangling gates will be described in Sec. 3.2. Finally in Sec. 3.3 we include the effect of micromotion into the gate design.

3.1 Numerical Solution of Ions' Classical Motions

In this section we solve the dimensionless equation of motion (EOM) of N ions in a trap [Eq. (1.13)]:

$$\ddot{R}_{i\sigma} + (a_\sigma - 2q_\sigma \cos 2t) R_{i\sigma} - 4 \sum_{j \neq i} \frac{R_{i\sigma} - R_{j\sigma}}{\left[\sum_\rho (R_{i\rho} - R_{j\rho})^2\right]^{\frac{3}{2}}} = 0, \tag{3.1}$$

where $i = 1, 2, \cdots, N$ corresponds to each ion and $\sigma = x, y, z$ for the three spatial directions.

Since the potential has a period of π, it is reasonable to expect a solution with π period [51]. In Sec. 3.1.1 we will follow the notation of Ref. [51] and describe how the periodic solutions (equilibrium configuration of the ions) can be found accurately. Then we will review the derivation of the EOM for small perturbations around the periodic solution in Sec. 3.1.2 following the steps of Ref. [51] and develop numerical methods to solve this equation to arbitrary precision. After briefly discussing the stability of infinitesimal perturbation in Sec. 3.1.3, we move on to the molecular dynamics (MD) method for large disturbance and the phenomenon of RF heating in Sec. 3.1.4. Finally in Sec. 3.1.5 we will examine the existence of soft modes (low-frequency modes) in large ion crystals and their influence on the formation of the crystal and on quantum computing.

3.1.1 Periodic Crystal Solution

To find the crystal structure in the ion trap, we can time evolve the system and gradually turn down the damping until it reaches the equilibrium distribution. For this purpose we can apply some standard ordinary differential equation (ODE) integrators such as forward Euler, leapfrog or Runge-Kutta methods (see e.g. Ref. [59]) to solve the Newtown's equation of

the N ions (molecular dynamics simulation). Because there will be nonzero damping terms, the stability of the ODE integrator is not very important and the step size need not be extremely small. In comparison, in Sec. 3.1.4 we will consider how to simulate these motions more accurately to study weak heating effects when no damping term is applied.

We can start from a random initial configuration. If some symmetries or some *a priori* knowledge about the final distribution exist, then we can also choose the initial conditions accordingly. For example, if the trapping potential along the z direction is much stronger than that along x and y directions, then we can choose $z_i = 0$ for all the ions, which can speed up the convergence.

To reach the equilibrium positions from a random initial state, there must be some dissipation in the system. In the simulation we add a $-\gamma(t)\dot{R}_{i\sigma}$ term to the RHS of Eq. (3.1) and gradually turn it down during the time of simulation. For example, we can choose $\gamma(t) = \gamma_0(1 - t/T)^n$ where T is the total evolution time; or we can use piecewise-constant $\gamma(t)$, that is, we start from a large γ and evolve the system for some hundreds of RF periods, then we use the final state we get as the new initial state, reduce γ and repeat this process. Similar to the case of a static potential, there can be multiple local minima, i.e. multiple equilibrium solutions. By gradually reducing the damping term it is more likely to go into a stable solution. (See Sec. 3.1.3 for the stability of a solution.)

One problem is that sometimes by numerically evolving the system with a cooling term we are not able to get an accurate periodic solution to Eq. (3.1): when the damping is high, the solution we get clearly deviates from what we want; but if the damping is too low, instability may arise due to the ODE integrator or the finite step size we use, and the accurate simulation may be too costly (see Sec. 3.1.4 for more details about MD simulation). This motivates us to consider a method that can iteratively increase the accuracy of a solution.

Let us express the equilibrium solution with the period of π as

$$R^{\pi}_{j\sigma}(t) = \sum_{n=-\infty}^{+\infty} B_{2n,j\sigma} e^{i2nt}, \tag{3.2}$$

where $j = 1, 2, \cdots, N$ labels the ions and $\sigma = x, y, z$ the spatial directions. To the lowest order in a and q^2, we have [51]

$$B_{2,j\sigma} \approx -\frac{q_\sigma}{4} B_{0,j\sigma}. \tag{3.3}$$

Also note that due to the time-reversal symmetry of Eq. (3.1), we have $B_{2n,j\sigma} = B_{-2n,j\sigma} = B^*_{2n,j\sigma}$. Therefore all the expansion coefficients are real.

For the purpose of quantum computing, we want the micromotion to be small, because we need to focus the laser beams on each ion for their manipulation. Therefore we are mainly interested in the small a and q regime, and we can expect to truncate at some order in the above expansion for a given precision.

If $R^{\pi}_{i\sigma}(t)$ has a period of π, so does any function of coordinates. Therefore the last term in Eq. (3.1) can be regarded as a driving term with a period of π:

$$D^{\pi}_{i\sigma}(t) \equiv 4 \sum_{j \neq i} \frac{R^{\pi}_{i\sigma}(t) - R^{\pi}_{j\sigma}(t)}{\left\{ \sum_\rho \left[R^{\pi}_{i\rho}(t) - R^{\pi}_{j\rho}(t) \right]^2 \right\}^{3/2}} \equiv \sum_{n=-\infty}^{+\infty} D_{2n,i\sigma} e^{i2nt}. \tag{3.4}$$

Then we get a recurrence relation:

$$(a_\sigma - 4n^2) B_{2n,i\sigma} - q_\sigma B_{2n-2,i\sigma} - q_\sigma B_{2n+2,i\sigma} = D_{2n,i\sigma}. \tag{3.5}$$

If we truncate at finite order of Fourier series, this is just a system of linear equations and can be solved iteratively: we can use the old solution of $\{B_{2n,i\sigma}\}$ to calculate the driving

term $\{D_{2n,i\sigma}\}$ and then find the new solution of $\{B_{2n,i\sigma}\}$. Unfortunately, numerically we find that this method is not stable and the result will deviate further and further away from the periodic solution. The reason is that for the leading order term $B_{0,i\sigma}$, we have $n = 0$ and thus the coefficient in front of it is only of the order $O(a)$, which is a small parameter. When computing the new solution from the odd one, we take the inverse of these small parameters and therefore the error gets enlarged.

On the other hand, the "driving term" can also be expressed as [51]

$$D^{\pi}_{i\sigma}(t) = 4\sum_{j} G^{\pi}_{ij}(t) R^{\pi}_{j\sigma}(t), \tag{3.6}$$

where

$$\begin{aligned} G^{\pi}_{ij}(t) &= \delta_{ij} \sum_{k\neq i} \frac{1}{\left\{\sum_{\rho}\left[R^{\pi}_{i\rho}(t) - R^{\pi}_{k\rho}(t)\right]^2\right\}^{3/2}} - (1-\delta_{ij}) \frac{1}{\left\{\sum_{\rho}\left[R^{\pi}_{i\rho}(t) - R^{\pi}_{j\rho}(t)\right]^2\right\}^{3/2}} \\ &\equiv \sum_{n=-\infty}^{+\infty} G_{2n,ij} e^{i2nt}. \end{aligned} \tag{3.7}$$

With a suitable division of the Coulomb interaction term into these two alternative forms, we get

$$(a_\sigma - 4n^2) B_{2n,i\sigma} - q_\sigma B_{2n-2,i\sigma} - q_\sigma B_{2n+2,i\sigma} + 4\alpha \sum_{m,j} G_{2n-2m,ij} B_{2m,j\sigma} = (1+\alpha) D_{2n,i\sigma}, \tag{3.8}$$

where the α-dependent terms on the two sides cancel each other for the accurate solution. Their purpose is to give larger "weight" to the leading order terms in the system of linear equations. We can now use the old solution to evaluate $G_{2n,ij}$ and $D_{2n,i\sigma}$ and then calculate the new solution iteratively. Numerically we find that $\alpha \geq 1$ leads to convergence around the

periodic solution, if we start from the approximate solution we found with a weak damping term. Note that if in $B_{2n,i\sigma}$ we truncate at $n = \pm M$, then in $G_{2n,ij}$ we need to truncate at $n = \pm 2M$. Also note that such a truncation will only work for small q so that the higher order terms quickly go to zero.

3.1.2 Normal Modes

In this subsection we solve all the collective normal modes of the ion crystal. For this purpose we consider small perturbation around the equilibrium trajectories $\{R^\pi_{i\sigma}(t)\}$.

Expansion around Crystal Solution

Let us first derive the equation of motion for a small deviation. Following Ref. [51], we define a matrix function $K(t)$

$$K_{i\sigma,j\tau}(t) = \begin{cases} -3\frac{(R^\pi_{i\sigma}-R^\pi_{j\sigma})(R^\pi_{i\tau}-R^\pi_{j\tau})}{\left[\sum_\rho (R^\pi_{i\rho}-R^\pi_{j\rho})^2\right]^{5/2}} & (i\neq j, \sigma\neq\tau) \\ \frac{\left[\sum_\rho (R^\pi_{i\rho}-R^\pi_{j\rho})^2\right]-3(R^\pi_{i\sigma}-R^\pi_{j\sigma})^2}{\left[\sum_\rho (R^\pi_{i\rho}-R^\pi_{j\rho})^2\right]^{5/2}} & (i\neq j, \sigma=\tau) \\ 3\sum_{k\neq i}\frac{(R^\pi_{i\sigma}-R^\pi_{k\sigma})(R^\pi_{i\tau}-R^\pi_{k\tau})}{\left[\sum_\rho (R^\pi_{i\rho}-R^\pi_{k\rho})^2\right]^{5/2}} & (i=j, \sigma\neq\tau) \\ -\sum_{k\neq i}\frac{\left[\sum_\rho (R^\pi_{i\rho}-R^\pi_{k\rho})^2\right]-3(R^\pi_{i\sigma}-R^\pi_{k\sigma})^2}{\left[\sum_\rho (R^\pi_{i\rho}-R^\pi_{k\rho})^2\right]^{5/2}} & (i=j, \sigma=\tau) \end{cases} \tag{3.9}$$

where the t dependence of $R^\pi_{i\sigma}$ is omitted for simplicity. Small perturbation $r_{i\alpha}$ around the periodic crystal solution is then governed by

$$\frac{d^2 r_{i\sigma}}{dt^2} + (a_\sigma - 2q_\sigma \cos 2t) r_{i\sigma} + 4\sum_{j,\tau} K_{i\sigma,j\tau}(t) r_{j\tau} = 0. \tag{3.10}$$

Because the $K(t)$ matrix also has a period of π, it can be expanded as

$$K(t) = K_0 - 2K_2 \cos 2t - 2K_4 \cos 4t - \cdots \tag{3.11}$$

For a typical periodic solution $R^{\pi}_{i\sigma}$, we would expect K_0 to be of the same order as a and q^2, because the Coulomb interaction should on average be balanced by the external AC and DC fields; K_2 should be smaller by a factor of q, and K_4 be even smaller. Then we can define $A_{i\sigma,j\tau} = a_\sigma \delta_{ij}\delta_{\sigma\tau} + 4(K_0)_{i\sigma,j\tau}$ and $Q_{i\sigma,j\tau} = q_\sigma \delta_{ij}\delta_{\sigma\tau} + 4(K_2)_{i\sigma,j\tau}$. The above equation can be written in the vector form [51]:

$$\frac{d^2\boldsymbol{r}}{dt^2} + (A - 2Q\cos 2t)\boldsymbol{r} = 0, \tag{3.12}$$

where $\boldsymbol{r}$ is a $3N$ by 1 column vector, and we have neglected higher order terms such as K_4, K_6, $\cdots$ The effect of the K_4 term is considered in Ref. [60], but the method used there is difficult to generalize to higher order terms. Furthermore, as we will see below, it is hard to directly apply the method used in Refs. [51, 60] for large ion crystals. Here we will tackle this problem in a different way: we first consider how to find good approximate normal modes, at least in the small a and q regime; then we describe how the accuracy of the solution to Eq. (3.12) or more precisely Eq. (3.10) can be improved iteratively. Also note that, although throughout this chapter we work with ideal harmonic traps, our method can be easily generalized to anharmonic traps by absorbing the higher order forces into $K(t)$ in Eq. (3.10).

Approximate Normal Modes

Following Ref. [51], a solution to Eq. (3.12) can be expanded as

$$\boldsymbol{r} = \sum_{n=-\infty}^{+\infty} \boldsymbol{C}_{2n} \left[c e^{i(2n+\beta)t} + c^* e^{-i(2n+\beta)t} \right], \tag{3.13}$$

which is correct for non-integral β. Here $\boldsymbol{C}_{2n}$ are real $3N$ by 1 vectors and c is a complex number. To solve all the normal modes, we must determine all the characteristic exponents β. An imaginary β means an exponential increase or decrease in the deviation from the equilibrium trajectories, while all β's being real corresponds to oscillatory behavior.

Plug this expansion into Eq. (3.12) and define $R_{2n} = A - (2n + \beta)^2$. We get

$$Q\boldsymbol{C}_{2n-2} = R_{2n}\boldsymbol{C}_{2n} - Q\boldsymbol{C}_{2n+2}. \tag{3.14}$$

Suppose the expansion can be truncated at some large $|n|$, we get two independent relations [51]

$$\boldsymbol{C}_2 = P_1 Q \boldsymbol{C}_0 \equiv \{R_2 - Q[R_4 - Q(R_6 - \cdots)^{-1}Q]^{-1}Q\}^{-1} Q\boldsymbol{C}_0 \tag{3.15}$$

and

$$Q\boldsymbol{C}_2 = P_2 \boldsymbol{C}_0 \equiv \{R_0 - Q[R_{-2} - Q(R_{-4} - \cdots)^{-1}Q]^{-1}Q\}\boldsymbol{C}_0. \tag{3.16}$$

To get a nonzero solution, we must have

$$\det(P_2 - QP_1Q) = 0, \tag{3.17}$$

and $\boldsymbol{C}_0$ is the eigenvector of $P_2 - QP_1Q$ corresponding to the eigenvalue of 0.

Now the remaining problem is to find all the solutions to Eq. (3.17). Given the order of truncation, $\det(P_2 - QP_1Q)$ is just a function of β. Therefore in principle we can solve this problem by finding all the roots of this function numerically, as is done in Refs. [51, 60]. However, as the ion number N increases, the separation between the frequencies of the $3N$ normal modes is decreasing and it becomes hard to solve all of them without any *a priori* knowledge about their distribution. Furthermore, we are not guaranteed that all the characteristic exponents are real, which makes the numerical search of the solution even more difficult.

Fortunately, in the limit of small a and q^2, some approximations can be made. In this limit we have

$$T \equiv P_2 - QP_1Q \approx R_0 - QR_2^{-1}Q - QR_{-2}^{-1}Q, \tag{3.18}$$

where R_{2n} terms for $n = \pm 2, \pm 3, \cdots$ are multiplied by higher order terms of q and therefore have been neglected. Later we will show that β is of the order $\sqrt{a + q^2/2}$. Then we have $R_2^{-1} \approx -(2+\beta)^{-2} \approx -1/4$ and $R_{-2}^{-1} \approx -(-2+\beta)^{-2} \approx -1/4$, and we get $T \approx A - \beta^2 + Q^2/2$. Therefore, to find the characteristic exponents, we only need to calculate the eigenvalues of $A + Q^2/2$ and then take the square root. $\boldsymbol{C}_0$'s are the corresponding eigenvectors. Also note that we have recovered the approximate solution of Mathieu equation [20] if $N = 1$, i.e. if there is no K matrix due to Coulomb interaction.

However, in many ion trap experiments a and q are not extremely small. For example, $q \approx 0.35$ in Ref. [28] and $q \approx 0.41$ in Ref. [32]. In this regime the above approximation is not good enough, and for some 2D or 3D ion crystals with low-frequency modes (soft modes) it may even produce imaginary characteristic exponents when the actual oscillation is stable. In these cases it will be necessary to include higher order expansions. Now we consider the

following expansion for $n \neq 0$:

$$\begin{aligned} R_{2n}^{-1} &= \left[A - (2n+\beta)^2\right]^{-1} = \left(A - 4n^2 - 4n\beta - \beta^2\right)^{-1} \\ &= -\frac{1}{4n^2}\left(1 - \frac{\beta}{n} - \frac{\beta^2 - A}{4n^2} + \frac{\beta^2}{n^2}\right) + O(\beta^3) \end{aligned} \tag{3.19}$$

where β is roughly of the order $\sqrt{a + q^2/2}$. Later we will see that the error is actually of the order $O(\beta^4)$, because the expression for the characteristic exponent is symmetric for positive and negative n; since the odd order terms of β contain an odd power of n, they will be cancelled in the final result.

Also we have the expansion

$$P_1 \approx \left[R_2 - QR_4^{-1}Q\right]^{-1} = R_2^{-1} + R_2^{-1}QR_4^{-1}QR_2^{-1} + O(q^4), \tag{3.20}$$

$$P_2 \approx R_0 - Q\left[R_{-2} - QR_{-4}^{-1}Q\right]^{-1}Q = R_0 - QR_{-2}^{-1}Q - QR_{-2}^{-1}QR_{-4}^{-1}QR_{-2}^{-1}Q + O(q^6). \tag{3.21}$$

Therefore

$$T = P_2 - QP_1Q \approx A + \frac{1}{2}Q^2 + \frac{1}{8}QAQ + \frac{1}{128}Q^4 - \beta^2\left(1 - \frac{3}{8}Q^2\right). \tag{3.22}$$

Because $\boldsymbol{C}_0$ satisfies $T\boldsymbol{C}_0 = 0$, β^2 is now given by a generalized eigenvalue problem

$$\left[A + \frac{1}{2}Q^2 + \frac{1}{8}QAQ + \frac{1}{128}Q^4\right]\boldsymbol{C}_0 = \beta^2\left(1 - \frac{3}{8}Q^2\right)\boldsymbol{C}_0, \tag{3.23}$$

with the error of the order a^2 and q^4. Note that here $\boldsymbol{C}_0$'s are no longer orthonormal. To describe the normal modes to the same order of approximation we must include oscillations

at the multiples of the RF frequency, which are given by:

$$\boldsymbol{C}_{\pm 2} = \left(R_{\pm 2} - QR_{\pm 4}^{-1}Q\right)^{-1} Q\boldsymbol{C}_0, \tag{3.24}$$

$$\boldsymbol{C}_{\pm 4} = R_{\pm 4}^{-1}Q\boldsymbol{C}_{\pm 2}. \tag{3.25}$$

Approach the Accurate Solution

What we described above is only an approximate solution to Eq. (3.17), or equivalently Eq. (3.12), and a generalization to higher order expansions in a and q is not trivial. Furthermore, from Eq. (3.10) to Eq. (3.12) we have already ignored higher order expansions of $K(t)$ [Eq. (3.11)]. Here we describe how we can reach arbitrary precision from the approximate solution we got before. First we will solve Eq. (3.17) and then we will go back to the original Eq. (3.10).

Let us rewrite Eq. (3.17) as

$$T\boldsymbol{C}_0 \equiv (A - M_+ - M_- - \beta^2)\boldsymbol{C}_0 = 0, \tag{3.26}$$

where

$$M_+ = Q\{R_2 - Q[R_4 - Q(R_6 - \cdots)^{-1}Q]^{-1}Q\}^{-1}Q \tag{3.27}$$

and

$$M_- = Q\{R_{-2} - Q[R_{-4} - Q(R_{-6} - \cdots)^{-1}Q]^{-1}Q\}^{-1}Q. \tag{3.28}$$

T is a matrix depending on β (note that not only the constant β^2 but also the R_{2n} matrices are β-dependent) and $\boldsymbol{C}_0$ is an eigenvector with the eigenvalue of 0. Now if we have an inaccurate β, $T(\beta)$ will not have an eigenvalue of exactly zero, but there should be one value

close to 0 if β is close to the accurate mode frequency. Hence what we can do is to start from our approximate β and compute the eigenvalue of $T(\beta)$ with the smallest magnitude, which we call Δ, using e.g. inverse iteration method [61], that is,

$$[A - M_+(\beta) - M_-(\beta) - \beta^2]\boldsymbol{C}_0 = \Delta \boldsymbol{C}_0, \tag{3.29}$$

or

$$[A - M_+(\beta) - M_-(\beta) - (\beta^2 + \Delta)]\boldsymbol{C}_0 = 0. \tag{3.30}$$

Then we can update $\beta \leftarrow \sqrt{\beta^2 + \Delta}$ and repeat this process until the value converges. Although T involves infinite-continued matrix inversions, we can truncate at some value of n such that the error is below the precision we set. Also note that if there are degeneracy in the eigenvalues, the corresponding eigenvectors we find may not be orthogonal and we need to apply Gram-Schmidt process manually.

All the above formulas are derived from Eq. (3.12), where higher order expansions of $K(t)$ have been neglected. For high-precision computation of the normal modes, we may need to include their effects. The K_4 term is considered in Ref. [60] by two modified continued inversions similar to Eq. (3.15) and Eq. (3.16). However, the derivation of these expressions becomes more and more complex as we include higher and higher order terms. Here we describe a simpler method given the above approximate solution.

In general, we can rewrite the EOM for small perturbation around the periodic solution [Eq. (3.10)] as

$$\frac{d^2\boldsymbol{r}}{dt^2} + (A - 2Q\cos 2t - 2Q_4\cos 4t - 2Q_6\cos 6t - \cdots)\boldsymbol{r} = 0 \tag{3.31}$$

with $Q_{2n} = 4K_{2n}$ ($n \geq 2$) from the Fourier expansion of the matrix function $K(t)$ [Eq. (3.11)].

Using the same expansion of Eq. (3.13), we get a general recurrence relation

$$R_{2n}\boldsymbol{C}_{2n} = Q(\boldsymbol{C}_{2n-2} + \boldsymbol{C}_{2n+2}) + Q_4(\boldsymbol{C}_{2n-4} + \boldsymbol{C}_{2n+4}) + Q_6(\boldsymbol{C}_{2n-6} + \boldsymbol{C}_{2n+6}) + \cdots \tag{3.32}$$

where again $R_{2n} \equiv A - (2n + \beta)^2$.

Now we truncate these equations at $\pm n$ and express them in a matrix form

$$\begin{pmatrix} R_{-2n} & -Q & -Q_4 & \cdots & 0 & 0 & 0 \\ -Q & R_{-2n+2} & -Q & \cdots & 0 & 0 & 0 \\ -Q_4 & -Q & R_{-2n+4} & \cdots & 0 & 0 & 0 \\ \vdots & \vdots & \vdots & \ddots & \vdots & \vdots & \vdots \\ 0 & 0 & 0 & \cdots & R_{2n-4} & -Q & -Q_4 \\ 0 & 0 & 0 & \cdots & -Q & R_{2n-2} & -Q \\ 0 & 0 & 0 & \cdots & -Q_4 & -Q & R_{2n} \end{pmatrix} \begin{pmatrix} \boldsymbol{C}_{-2n} \\ \boldsymbol{C}_{-2n+2} \\ \boldsymbol{C}_{-2n+4} \\ \vdots \\ \boldsymbol{C}_{2n-4} \\ \boldsymbol{C}_{2n-2} \\ \boldsymbol{C}_{2n} \end{pmatrix} = 0, \tag{3.33}$$

where the expansion of Q_{2n} can be truncated at some different order m, which is not shown in the above equation for simplicity. Again a mode frequency β_k should make the determinant of this matrix equal to zero, and all the mode vectors (including the higher order expansions) are given by the corresponding eigenvector with eigenvalue 0. Now we can simply plug in the approximate solutions we get before and apply the iterative method to approach the exact solution to each mode. Note that the diagonal of the above matrix has a common $-\beta^2$ term, so again we can attribute the nonzero eigenvalue Δ to β^2 by making $\beta \leftarrow \sqrt{\beta^2 + \Delta}$ in the iteration.

Finally, we show an example of the computed normal modes compared with the exact solution

from molecular dynamics simulation in Fig. 3.1. Here we consider a crystal of 100 ions and the normal modes match perfectly with the exact solutions.

3.1.3 Stability against Small Disturbance

By starting from a random initial state and gradually turn down the cooling term, usually we can find a periodic solution where all β's are real. Although it might be difficult to strictly prove the existence of periodic solutions with the same period as the periodic nonlinear differential equation [Eq. (3.1)], numerically it seems that for typical values of a and q used in ion trap experiments and an ion number of less than a few hundreds, we can always find such solutions.

Suppose we have found such a solution $R^{\pi}_{i\sigma}(t)$ with a period of π using e.g. the method in Sec. 3.1.1, with the characteristic exponents of all the $3N$ normal modes β_k being real. Since any small perturbation $r_{i\sigma}(t)$ around the equilibrium trajectories can be decomposed into these normal modes, we conclude that, at least to the first order, the small perturbation does not increase with time and thus the equilibrium configuration is stable.

Since the first order perturbation shows oscillatory behavior, we must consider higher order expansions to discuss the stability of the system, which becomes much more difficult. However, the above result also means that the system can be stabilized by introducing arbitrarily small damping, e.g. the existence of a weak laser cooling.

Let us formulate the derivation of the normal modes again with a small constant damping term. (It can also be taken as direction and position dependent, which does not change the

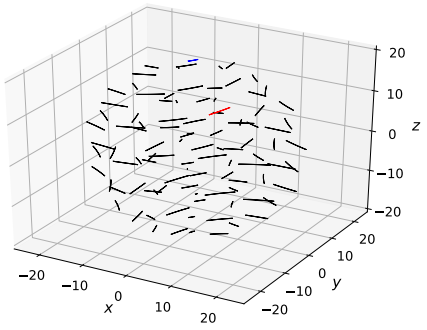

(a)

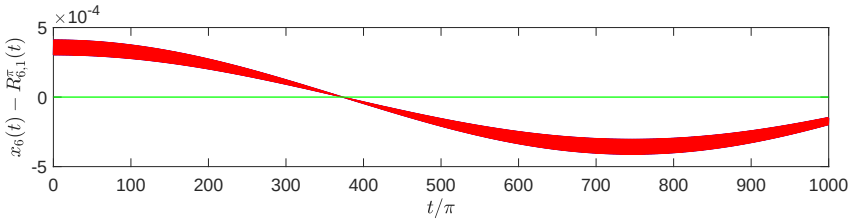

(b)

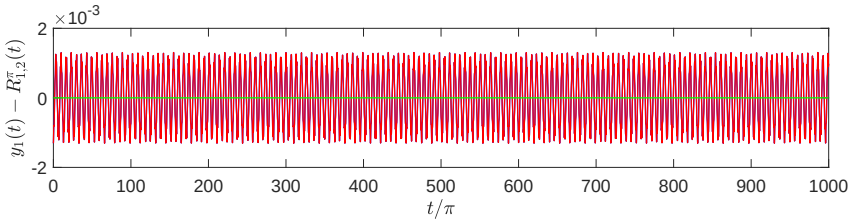

(c)

Figure 3.1: Comparison between the computed normal modes and the exact solution from numerical simulation. Here we consider a crystal of 100 ions with trap parameters $\boldsymbol{a} = (-0.015, -0.015, 0.03)$ and $\boldsymbol{q} = (0.3, -0.3, 0)$. (a) Equilibrium trajectories of the 100 ions. (b) Evolution of the x coordinate of ion 6 [colored in blue in (a)] over 1000 RF periods for a weak excitation of 0.01 in the lowest mode with $\beta = 0.001340$. (c) Evolution of the y coordinate of ion 1 [colored in red in (a)] over 1000 RF periods for a weak excitation of 0.01 in the highest mode with $\beta = 0.3032$. In both (b) and (c), the blue curve is from direct numerical simulation using Forest-Ruth method, 1000 steps per RF period and *double* precision (see Sec. 3.1.4), the red curve is computed from the normal mode expansions, and the green curve is their difference. The equilibrium trajectories $R^{\pi}_{i\sigma}(t)$ at the order of $O(1)$ is already subtracted from these curves. Note that our computed normal modes are correct for a wide range of spectra over two orders of magnitude.

qualitative conclusion about the stability.) The equation of motion [Eq. (3.1)] now becomes

$$\ddot{R}_{i\sigma} + (a_\sigma - 2q_\sigma \cos 2t)R_{i\sigma} + \gamma \dot{R}_{i\sigma} - 4\sum_{j\neq i} \frac{R_{i\sigma} - R_{j\sigma}}{\left[\sum_\rho (R_{i\rho} - R_{j\rho})^2\right]^{\frac{3}{2}}} = 0. \tag{3.34}$$

Again we look for solutions with period of π. With the existence of friction, a direct molecular dynamics simulation can quickly converge to the desired solution.

Here we assume that $R_{i\sigma}(t)$ approaches the previous periodic solution $R^{\pi}_{i\sigma}(t)$ as γ goes to zero, so that for small γ we can neglect their difference. This is a reasonable assumption because this is how we find the previous periodic solution in the first place. We then linearize the equation of motion for small perturbation around the periodic solution $R^{\pi}_{i\sigma}(t)$:

$$\ddot{r}_{i\sigma} + \gamma \dot{r}_{i\sigma} + (a_\sigma - 2q_\sigma \cos 2t)r_{i\sigma} + 4\sum_{j,\tau} K_{i\sigma,j\tau}(t) r_{j\tau} = 0, \tag{3.35}$$

where K is again given by Eq. (3.9). Taking a similar expansion as Eq. (3.13)

$$\boldsymbol{r} = \sum_{n=-\infty}^{+\infty} \left[ce^{i(2n+\beta)t}\boldsymbol{C}_{2n} + c^* e^{-i(2n+\beta^*)t}\boldsymbol{C}^*_{2n}\right], \tag{3.36}$$

with β and $\boldsymbol{C}_{2n}$ now allowed to take complex values, we have a modified recurrence relation

$$Q\boldsymbol{C}_{2n-2} = R'_{2n}\boldsymbol{C}_{2n} - Q\boldsymbol{C}_{2n+2}, \tag{3.37}$$

where $R'_{2n} = A - (2n+\beta)^2 + i\gamma(2n+\beta)$. As is mentioned above, γ can be chosen arbitrarily small, so we consider only first order terms in γ. Then a direct observation is that by

replacing the old solution of β in Sec. 3.1.2, which satisfies Eq. (3.14), with the new value

$$\beta_{\text{new}} = \beta_{\text{old}} + i\frac{\gamma}{2}, \tag{3.38}$$

the modified recurrence relation Eq. (3.37) is automatically satisfied (up to the first order in γ). Hence any small deviation from this periodic solution will converge back to it at the rate of $\gamma/2$.

3.1.4 Direct Molecular Dynamics Simulation and RF Heating

We have shown in the previous subsections the stability of crystal solutions under small perturbation with arbitrarily weak damping. However, it does not exclude the possibility of heating under finite disturbance. Actually, this phenomenon, called RF heating, is well-known for trapped ions in a cloud state with high trap parameter q, and has been widely studied experimentally and theoretically. In this subsection, we will review some previous studies on RF heating and then examine some potential problems and improvements in its numerical study. There are of course many other heating sources such as noise in the electric field and collision of the trapped ions with background gases, as we discussed in Sec. 1.2.2, but here we give special emphasis to the RF heating: these other sources are technical and can be suppressed by e.g. cooling down the electrodes or increasing the vacuum quality; but if a crystal with micromotion is to be heated by even an ideal RF field, this will set an ultimate bound on the scalability of quantum computing in large ion crystals.

The study of heating in ion trap dates back to 1960s [22], although debates about its detailed mechanism continued even in 1990s [26,62–64]. What is known is that inside the first stability region of (single-ion) Mathieu equation (see Fig. 1.1 as an example for a linear Paul trap),

there are some regions where two-(multiple-)ion crystal may not exist [65]; and for some other regions the crystal and the cloud solutions are bistable even under cooling, such that the system can stay in either state depending on the initial conditions [66]. Furthermore, the cloud state demonstrates deterministic chaos, which is the source of its RF heating, while the crystal state shows no visible heating in the numerical simulations; to go from the crystal to the cloud state, a strong enough disturbance is needed [66]. In other words, the crystal needs to melt first before it can be heated by the RF field, and this result seems to hold for quasi-1D [67], 2D [68] and 3D [69] crystals. This is consistent with our previous result that the crystal solution is stable under weak damping.

It is also shown that in some parameter regions the crystal solution is destabilized by nonlinear resonance [70], which is the coupling of different oscillation modes through higher order nonlinear interactions. The resonance condition can be written as $\sum_k m_k\omega_k = n\omega_{\rm rf}$ where m_k's and n are all integers, which is generalized from the two-ion case of Ref. [70]. This phenomenon was first studied for a single ion in the trap where the nonlinearity arises from the higher multipole expansions of the trapping potential [71–74]. For multiple ions, the Coulomb interaction can supply the required nonlinearity and hence such imperfection in the trapping potential is not necessary in the theory. We can expect a richer resonance structure as we increase the number of ions N because the number of normal modes is $3N$. However, we argue that this phenomenon should not be a significant problem for the stability of the ion crystal used for quantum computing for the following reasons. (1) The resonance conditions are fulfilled on lines of the 2D Mathieu stability region and hence it is not likely that a chosen set of parameters sits right on them. (2) The lowest order nonlinear resonances (small m_k) occur mainly for large q except for $n = 0$ in the above resonance condition, but the condition for $n = 0$ can be met even for a static potential and hence should not be related

to RF heating. On the other hand, for the purpose of quantum computing we are mainly interested in the small q regime, so we are away from the region where low-order nonlinear resonance (those with stronger influence) can occur. (3) If such nonlinear resonance occurs in the system and destabilize the crystal, then we would not be able to find such a crystal solution when we start from a random configuration and gradually reduce the damping rate. Therefore if we can get a crystal solution in the first place, as we almost always do using the methods described in the previous subsections for reasonable trap parameters and for ion numbers ranging from 2 to a few hundreds, then we already know they are not affected by the nonlinear resonance. Finally, this result of destabilization of two-ion crystal is not reproduced by the direct numerical simulation that will be described below. One reason is that Ref. [70] did not report all the parameters in their simulation such as the initial conditions and the Doppler cooling parameters, as well as the step size of the simulation; and another possibility is that various numerical errors, as will be discussed later in this subsection, might not be correctly treated. Nevertheless, we can conclude that nonlinear resonance is not a significant problem in the low q regime for a crystal with hundreds of ions.

To study the RF heating effect, we can directly simulate the dynamics of the ions, i.e. the molecular dynamics (MD) method. There are several challenges in applying the MD method to ions in a Paul trap. First, the timescale of different dynamics of the system spans several orders of magnitude: the fastest dynamics is at the RF frequency, which is typically tens of MHz; in comparison, the secular motions are typically at the order of 0.1-1 MHz, except for a few soft modes (see Sec. 3.1.5 for more discussions); the RF heating can be even slower, and to safely decide if it can be neglected or not, we may need to simulate the system up to the time of multiple gates, so the total simulated time can be as high as tens of ms. If each RF period is simulated by, say, 100 steps, then the total number of steps can be at the order

of 10^7-10^8.

Second, it is well-known that the N-body problem is chaotic even without the oscillatory fields, such that the numerical errors explode exponentially with the simulated time [75]. Arguably, small errors at each step of numerical simulation should not influence the observation of RF heating, because with the existence of Doppler cooling or electric noise, there will always be random disturbance during the evolution. However, without ruling out the possibility that numerical errors at each step can accumulate in a "coherent" way and lead to a fake increase in total energy, such simulations will not be convincing. We will look into these numerical errors later.

Third, the Coulomb interaction between the ions is long-range, so we cannot neglect the interaction between far-apart ion pairs and in principle we will need to consider the interaction between $O(N^2)$ pairs at each step. Some approximation methods such as particle-mesh algorithm and particle-particle-particle-mesh algorithms [76] have been devised to bring down the scaling to $O(N \log N)$ or even $O(N)$. However, due to the chaotic behavior mentioned above, here we prefer the exact algorithm. Luckily for just tens to hundreds of ions it will not be a significant problem.

Numerical Errors in MD Simulation

There are basically three types of errors when solving ordinary differential equations (ODE) numerically: data error, discretization error and computational error [77]. The data error comes from the inaccurate parameters such as $\boldsymbol{a}$ and $\boldsymbol{q}$ and initial values of positions and velocities of the ions. For the study of RF heating this is not very important because we are looking into some general behavior which should not be too sensitive to the parameters and

initial conditions.

The discretization error (truncation error) arises because we set a finite step length when numerically integrating an ODE. Two common methods to mitigate this error are to reduce the step length and to use higher order methods. For example, the widely-used 4th order Runge-Kutta method has a local discretization error of $O(\Delta t^5)$, while the 10th or 14th order Runge-Kutta methods [78] (the coefficients are given by Ref. [79]) have much smaller errors with the same step length. A problem with explicit Runge-Kutta methods is that they are not "stable" in the sense that the amplitude of even a simple harmonic oscillator, simulated by the Runge-Kutta method, will increase exponentially with time for a fixed step size (of course for a fixed time we can expect convergence as we reduce the step size), which may obscure the heating effect we want to see. To make sure we observe the true physical evolution we have to suppress the discretization error. For any method of a given order, the error scales polynomially with the step length. In comparison, for the chaotic system we are considering, the error will be exponentially enlarged during the evolution time. This means the required number of steps goes exponentially with the time interval we want to simulate, which soon becomes intractable. On the other hand, if we choose to increase the order of Runge-Kutta method, it only needs to scale linearly with the length of time interval, but it is generally difficult to find all the coefficients for higher order explicit Runge-Kutta method.

The third type of error is the computational error (round-off error). It appears because we are using finite precision date type (e.g. *float* or *double*) to approximate the intermediate results of the calculation. It is reasonable to assume that the round-off errors at different steps are uncorrelated, then the total effect will be like a random walk and scales as the square root of the number of steps. Moreover, any previous errors will still be escalated in the following evolution, so this type of error also accumulates exponentially with the evolution

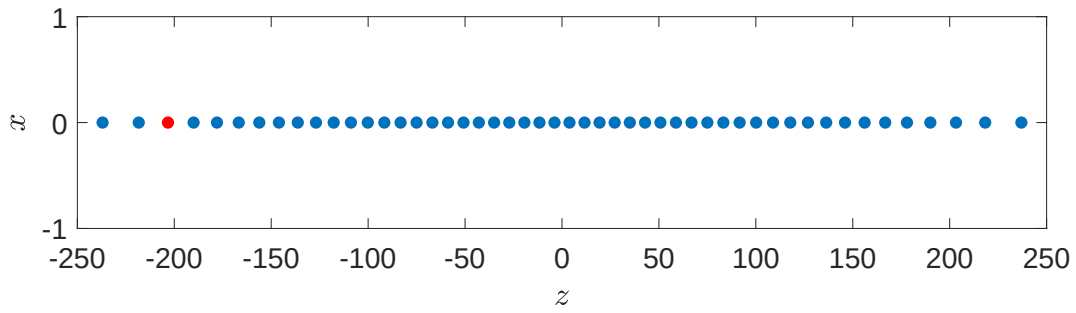

Figure 3.2: An example of 50 ions in a linear trap, with trapping parameters $\boldsymbol{a} = (-5.1 \times 10^{-5}, -4.9 \times 10^{-5}, 1 \times 10^{-4})$ and $\boldsymbol{q} = (0.343, -0.343, 0)$. The ions are initially at their equilibrium positions with the red ion being collided by a Yb-171 atom at room temperature $T = 300\,\mathrm{K}$, in a random direction.

time [77]. In general, this round-off error will lead to heating in the simulation [76, 80]. To reduce the error we can use arbitrary precision libraries like GMP for C language [81]. Since the precision of a floating-point type goes exponentially with the number of bits used to represent it, the latter only needs to scale linearly with the time duration of the simulation. However, the use of arbitrary-precision data type is in general much slower than that of the native data type of the machine such as *float* and *double*.

Now we show some numerical results to support the above analyses. Consider $N = 50$ $^{171}\mathrm{Yb}^{+}$ ions in a linear trap with $\boldsymbol{a} = (-5.1\times10^{-5},\ -4.9\times10^{-5},\ 1\times10^{-4})$ and $\boldsymbol{q} = (0.343,\ -0.343,\ 0)$. At low enough temperature they will form a 1D crystal as shown in Fig. 3.2. Here we choose $\omega_{\mathrm{rf}} = 2\pi \times 50\,\mathrm{MHz}$, which gives length unit $L_0 \approx 0.202\,\mu\mathrm{m}$ and time unit $T_0 \approx 6.37\,\mathrm{ns}$ (see Sec. 1.2). In the following figures we use dimensionless spatial and time coordinates.

Suppose initially all the ions are in their equilibrium positions but one ion (colored in red in Fig. 3.2) is collided by an Yb-171 atom at $t = 0$ at room temperature $T = 300\,\mathrm{K}$. The evolution of this ion's x coordinate is shown in Fig. 3.3 up to 1000 RF periods after the collision. The simulations are performed using the 10th order Runge-Kutta (RK10)

method with 100 steps per RF period, but with different numerical precisions to store the intermediate positions and velocities in the simulation. As we can see, the number of steps that can be simulated accurately for a given error tolerance roughly increases linearly with the number of bits we use to store the variables. Note that this is just to show the round-off error and that the solutions here still have large truncation errors.

In contrast, Fig. 3.4 shows the results using Runge-Kutta methods at different orders with different step sizes when fixing the precision at 128-bit. For convergence we want high order methods or small step sizes; but note that if we keep reducing the step size, i.e. increasing the number of steps for a given simulation time, the result will not converge because the round-off error will finally dominate. Therefore we shall increase the precision together with the number of steps to verify the convergence. According to the results in Fig. 3.3 and Fig. 3.4, we can suppress the round-off error to negligible level for $10^3 \sim 10^4$ RF periods using reasonable computational resources, but it is very difficult for the truncation error.

Even with nonzero truncation errors, it is still possible to prove the existence of RF heating in the simulation if we can separate the energy of the system from such errors. Actually this problem has also been considered for the traditional MD simulations with time-independent Hamiltonian: for these systems we want the energy to be conserved during the simulation regardless of the truncation errors. The solution is to use numerical methods that can preserve time-reversal symmetry such as leapfrog (2nd order) and Forest-Ruth (4th order, and it further preserves symplectic symmetry) methods [80]. Due to the time-reversal symmetry of EOM of the system [Eq. (3.1)] and the numerical method, if there is a solution with RF heating, by reversing the final velocity of all the ions, we can get a new solution with total energy decreasing with time. Thus we conclude that the numerical method itself does not prefer either an increase or a decrease in the energy; the RF heating, if observed, must

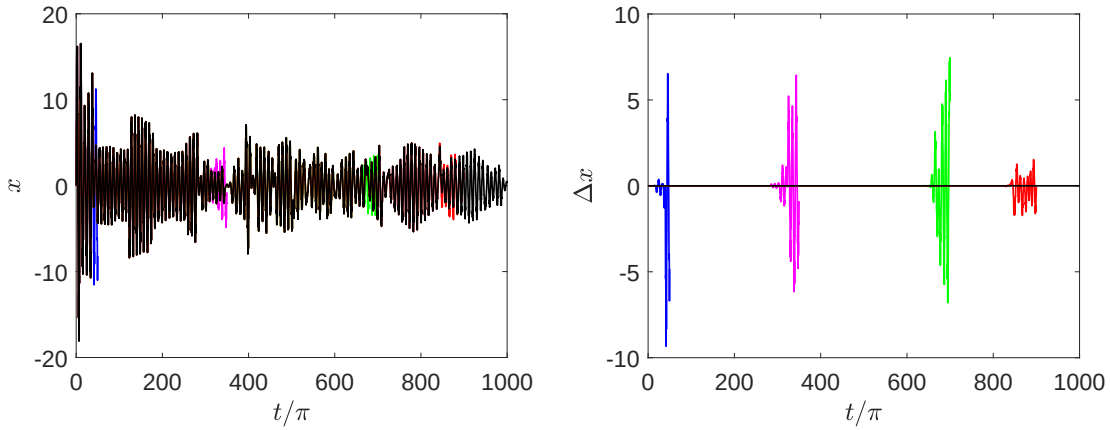

(a) (b)

Figure 3.3: (a) $x(t)$ for the ion being collided using RK10 method with 100 steps per RF period. The blue, magenta, green, red and black curves are for 32-bit, 96-bit, 160-bit, 192-bit and 384-bit precisions, respectively. We terminate each curve once they are significantly away from the "exact" solution of 384-bit precision. (b) Deviation of each curve from the "exact" solution. As we can see, there are noticeable computational errors at $t \approx 20\pi$ for 32-bit precision (*float*), $t \approx 285\pi$ for 96-bit precision, $t \approx 650\pi$ for 160-bit precision, and $t \approx 839\pi$ for 192-bit precision.

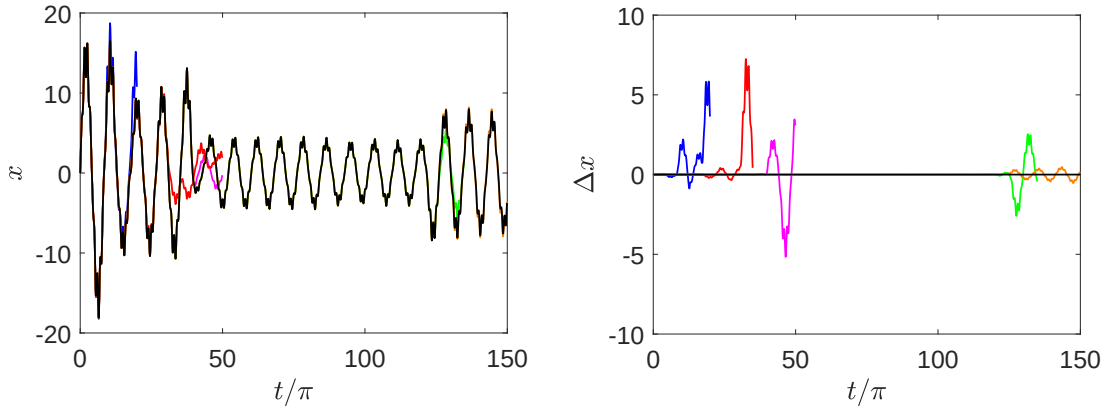

(a) (b)

Figure 3.4: (a) $x(t)$ for the ion being collided using 128-bit precision. The blue, magenta, green, red, orange and black curves are for RK4 with 10 steps per period, RK4 with 100 steps per period, RK4 with 1000 steps per period, RK10 with 10 steps per period, RK10 with 100 steps per period and RK14 with 100 steps per period, respectively. We terminate each curve once they are significantly away from the "exact" solution of RK14 with 100 steps per period. (b) Deviation of each curve from the "exact" solution.

be intrinsic in the system and will be analogous to the increase of entropy in statistical mechanics.

However, note that the time-reversal symmetry of these algorithms is held only in exact arithmetic [80]; with the existence of round-off errors we may still get fake heating behavior. For instance, we consider a chain of $N = 10$ $^{171}\mathrm{Yb}^+$ ions in a trap with $\boldsymbol{a} = (-5\times10^{-5},\ -5\times10^{-5},\ 1\times10^{-4})$ and $\boldsymbol{q} = (0.6,\ -0.6,\ 0)$. Note that here we use a large q just to demonstrate the effect; this value is much larger than what is typically used in the experiment. Again we assume all the ions are initially at their equilibrium positions but this time an initial thermal distribution at $T = 3\,\mathrm{K}$ for velocities. Fig. 3.5 shows the total kinetic energy of the system (averaged over each RF period) vs. the evolution time for two Forest-Ruth simulations using 100 steps per RF period but with 64-bit and 1024-bit precisions, respectively. The

low-precision one shows significant heating during the simulated time, which however is not seen in the simulation with higher precision, i.e. less round-off errors. Hence it is always favorable, if within the reach of computational resources, to increase the numerical accuracy and check the convergence of the simulation.

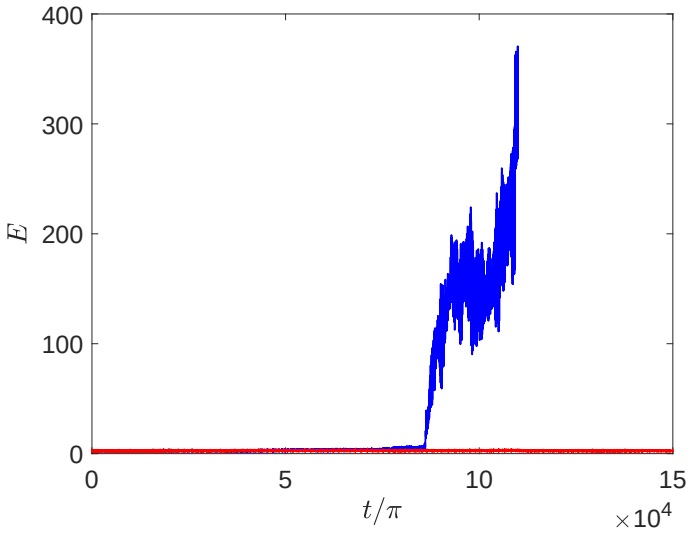

Figure 3.5: Average kinetic energy over each RF period vs. evolution time t. Both curves use Forest-Ruth method with 100 steps per RF period. The blue curve is simulated with 64-bit precision and shows significant heating since about 80000 RF periods; the red curve uses 1024-bit precision (which has no observable difference from the 1600-bit result) and shows no increase in energy over 150000 RF periods.

Having seen so many potential problems in studying RF heating, finally we look at an example where we can conclude for sure the existence of this phenomenon. Let us go back to the previous example of 50 ions as shown in Fig. 3.2 with the same initial conditions, and evolve the system for 3000 RF periods. Fig. 3.6 shows the forward and backward simulation of 3000 RF periods using Forest-Ruth method with 100 steps per period and 1600-bit precision. The velocities of the ions are reversed at $t = 3000\pi$, which separates the forward and the backward evolutions. The final state we get matches the initial states

within the *double* precision. Thus the heating shown in the forward evolution (starting from a randomly chosen initial state) is intrinsic in the dynamics of the system; in comparison, the backward evolution shows damping in the energy, but it is only for the specially chosen initial state. The round-off error here is negligible because there is no noticeable difference in these curves compared with the 1280-bit precision result.

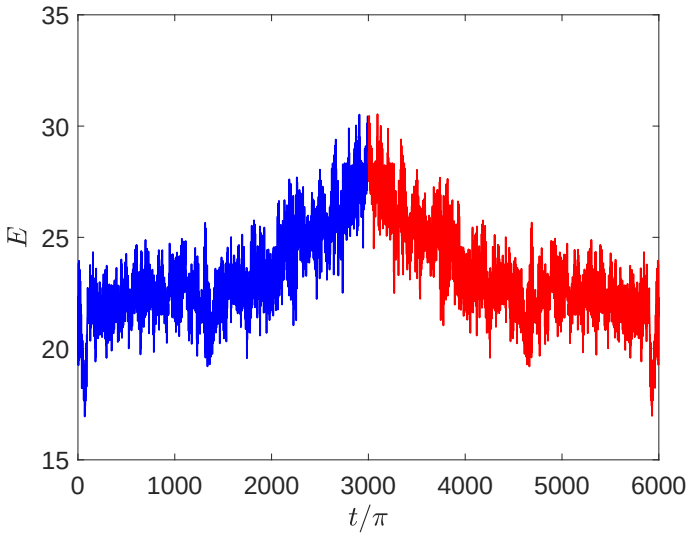

Figure 3.6: Average total energy over each RF period vs. time t. The blue curve is the forward evolution and the red part is the backward evolution. Both simulations uses FR method with 100 steps per period and 1600-bit precision.

Doppler Cooling

The simulation method described in this part is mainly based on Appendix D of Ref. [82], with small modifications. The author of this thesis is one of the coauthor of this paper and performed the numerical simulation of the ions' motions.

During the storage of the ion crystal, a weak Doppler cooling beam can be turned on to further stabilize it. Typically this beam is detuned at $\Delta = -\Gamma/2$ with a saturate intensity

$s = 1$ [see the definition below Eq. (1.20)] [30] and is at an angle to all the three principle axes of the trap, which we choose to be the [1, 1, 1] direction in the simulation.

Because the scattering rate of the photon $\Gamma\rho_{ee}$ is typically only a few MHz (e.g. for $^{171}\mathrm{Yb}^+$ ions) and is smaller than the RF frequency of the trap, the damping force should not be modeled as a simple $-\gamma\boldsymbol{v}$ term if we include the micromotion. In some literature, e.g. Ref. [66], this process is modelled by a velocity-dependent scattering rate of the photons, which still does not reflect the fact that the internal states of the ions may not follow the micromotion at the RF frequency. To describe this process in the simulation we use N vectors in $\mathbb{C}^2$ to represent the internal states of the ions and consider the excitation of ions by the laser beam quantum mechanically. Then quantum trajectory [83] method can be used to simulate the scattering process. At each step the internal state of an ion is first evolved from $|\psi(t)\rangle$ to $|\tilde{\psi}(t+\Delta t)\rangle$ under the effective Hamiltonian

$$H_{\text{eff}} = \frac{\Delta - \boldsymbol{k}\cdot\boldsymbol{v}}{2}\sigma_z + \frac{\Omega}{2}\sigma_x - \frac{i}{4}\gamma(I-\sigma_z). \tag{3.39}$$

Then with probability $\langle\tilde{\psi}(t+\Delta t)|\tilde{\psi}(t+\Delta t)\rangle$ it is renormalized to $|\psi(t+\Delta t)\rangle = |\tilde{\psi}(t+\Delta t)\rangle/\||\tilde{\psi}(t+\Delta t)\rangle\|$; otherwise a transition occurs and the ion goes back to the ground state $|\psi(t+\Delta t)\rangle = |0\rangle$, together with a momentum change as the ion absorbs a photon in the [1, 1, 1] direction and then emits one into a random direction. Note that if we include the Doppler cooling in the simulation, the time-reversal symmetry is broken so that the Forest-Ruth algorithm has no advantage over the Runge-Kutta algorithm; besides, since we introduce a random force due to the scattering of photons, small numerical errors at each step is no longer important and we can simply use *double* precision in the simulation.

Some numerical results are shown in Fig. 3.7. Fig. 3.7(a) uses the same trapping parameters

and initial conditions as those in Fig. 3.2, i.e. a single collision with an Yb-171 atom at room temperature. As we can see, the Doppler cooling is not functioning for this energetic motion because of the large detuning due to the Doppler effect. On the other hand, if we rescale the initial velocity so that it corresponds to a collision with H_2 rather than Yb-171, the system can be cooled by the laser beam, as is shown in Fig. 3.7(b). This observation matches well with the experiments: the Doppler cooling parameters we choose ($\Delta = -\Gamma/2$ and $s = 1$) is used for ions that are already at low temperature; at high temperature we will need larger detuning and stronger laser beams [30].

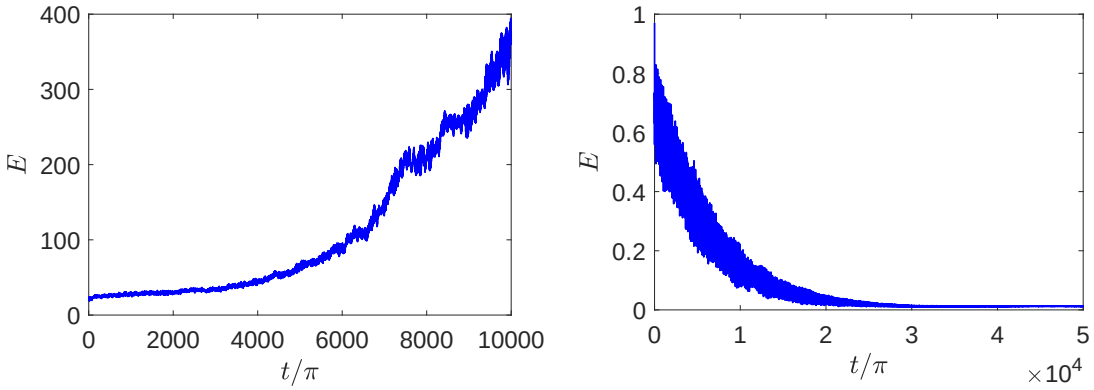

Figure 3.7: (a) Average total energy over each RF period vs. time t for the ions considered in Fig. 3.2 with the same initial conditions. (b) Average total energy over each RF period vs. time t for the same trapping parameters, but an initial collision with H_2 instead of Yb-171.

Melting of Ion Crystals

Knowing that the ion crystal needs to melt first before it can be heated by the RF field, now we want to estimate the temperature at which RF heating will start. Infinitely many ions in a plasma state can form a body-centered cubic (bcc) lattice at low temperature, whose

melting point is about [84–86]

$$k_B T \approx \frac{1}{173} \frac{e^2}{4\pi\epsilon_0 a_{WS}}, \tag{3.40}$$

with Wigner-Seitz radius defined by $4\pi a_{WS}^3/3 = V/N$. For finite ion crystals, the melting point will be shifted due to the different crystal structure and also the existence of a surface, but Eq. (3.40) can still be a good estimation for the order of magnitude [84]. Furthermore, Ref. [84] shows that the same melting point also holds for ions in RF trap if the effective temperature is correctly defined for only the secular motion (the velocity after averaging out the micromotion).

As an example, we consider a crystal of 50 $^{171}\mathrm{Yb}^+$ ions with the trapping parameters $\boldsymbol{a} = (0.0099, 0.0101, -0.02)$ and $\boldsymbol{q} = (-0.15, -0.15, 0.3)$. Here we choose $\omega_{\mathrm{rf}} = 2\pi \times 50\,\mathrm{MHz}$, and use the closest distance between the average positions of two ions $d_{\min} = 1.78\,\mu\mathrm{m}$ to approximate $2a_{WS}$. The melting point can be estimated to be around $T_c \sim 0.11\,\mathrm{K}$. First we find the equilibrium trajectories of the system using the methods in the previous subsections. Then we set the velocities of the ions according to a Maxwell-Boltzmann distribution at a temperature of T and let the system evolve for 1000 RF periods. In these and the following simulations we use Forest-Ruth algorithm with 100 steps per RF period and *double* precision. Because here we only want to study the immediate melting of the crystal, the accuracy of the simulation need not be very high. Fig. 3.8 shows the trajectories for the last 100 of the 1000 periods for (a) $T = 0.01\,\mathrm{K}$, (b) $T = 0.11\,\mathrm{K}$ and (c) $T = 1\,\mathrm{K}$. It is clear that when $T \ll T_c$ the ions only oscillate around their equilibrium positions and thus stay in the crystal state, while for $T \gg T_c$ they frequently change their positions and thus the crystal has melt. The $T \approx T_c$ case is more complex: it looks like in Fig. 3.8(b) the crystal has already melted, but the random motions of the ions are less violent than the $T \gg T_c$ case. This is probably

because the $d_{\min}$ we use is less than the actual a_{SW} and hence our estimated T_c is higher than the real value; therefore the behavior at the melting point is still not clear. Nevertheless, Eq. (3.40) seems to be a good estimation for the order of magnitude, and we shall be safe to say that the ions are in the crystal state if the temperature is much lower than the estimated transition point.

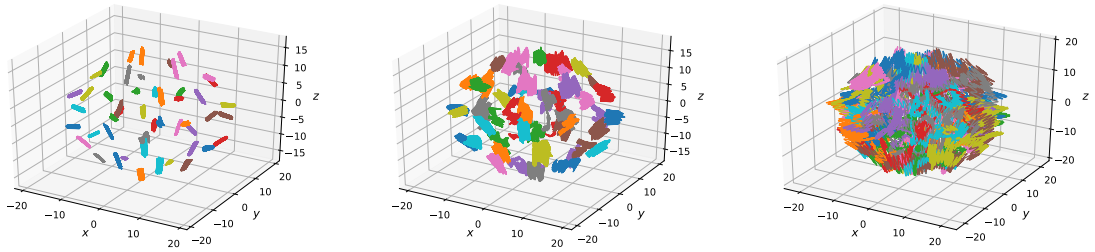

(a) (b) (c)

Figure 3.8: Trajectories for the last 100 RF periods during a 1000-period evolution. There are 50 $^{171}\mathrm{Yb}^{+}$ ions in a trap with parameters $\boldsymbol{a} = (0.0099, 0.0101, -0.02)$ and $\boldsymbol{q} = (-0.15, -0.15, 0.3)$. The initial positions of the ions are right at their equilibrium positions when the phase of the RF field is 0, while the initial velocities follow a Maxwell-Boltzmann distribution with (a) $T = 0.01\,\mathrm{K}$, (b) $T = 0.11\,\mathrm{K} \approx T_c$ and (c) $T = 1\,\mathrm{K}$.

The melting points for 2D and 1D crystals are more difficult to calculate. However, we can argue that the transition point should be higher than Eq. (3.40). The reasoning goes as follows: in one extreme case when the crystal is about to goes into the zigzag shape, effectively we still have a 3D crystal but with larger finite size effects, so the transition temperature should be similar to Eq. (3.40); in the other extreme case the crystal is strongly trapped in the transverse direction, so it takes higher energy to melt the crystal and the transition temperature increases (actually an ion chain in 1D is not possible to melt because the Coulomb repulsion will diverge as the ions approach each other and thus prevents the ions from exchanging positions). Thus Eq. (3.40) gives a good estimation for the order of

magnitude and upper bound of the melting temperature for all ion crystals. Some examples for 2D and 1D crystals are shown in Fig. 3.9 and Fig. 3.10. In the 1D case, for $T \gg T_c$ the trajectories of the ions have started to overlap with each other even though they have not exchanged positions; while for $T \lesssim T_c$ the ions are clearly separated from each other.

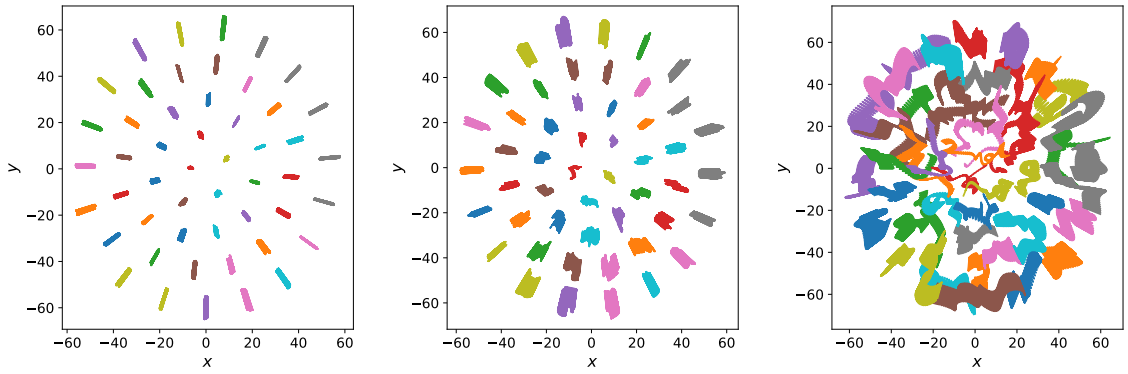

(a) (b) (c)

Figure 3.9: Trajectories (projected onto the x-y plane) for the last 100 RF periods during a 1000-period evolution. There are 50 $^{171}\mathrm{Yb}^{+}$ ions in a trap with parameters $\boldsymbol{a} = (-0.0099, -0.0101, 0.02)$ and $\boldsymbol{q} = (-0.15, -0.15, 0.3)$. The initial positions of the ions are right at their equilibrium positions when the phase of the RF field is 0, while the initial velocities follow a Maxwell-Boltzmann distribution with (a) $T = 0.007\,\mathrm{K}$, (b) $T = 0.066\,\mathrm{K} \approx T_c$ and (c) $T = 0.7\,\mathrm{K}$.

Incidentally, in the example of Fig. 3.6, where we do observe RF heating, the initial collision with Yb-171 at 300 K will give an effective temperature of $300/N = 6\,\mathrm{K}$ after thermalization, which is much higher than its melting point of about 0.1 K. On the other hand, for the example of Fig. 3.5, the melting point computed from Eq. (3.40) is $T_c \approx 0.05\,\mathrm{K}$. The temperature we use is 3 K, again much higher then T_c, but no heating is observed after we suppress the round-off error. One possible reason is that the simulated evolution time is not long enough to see significant heating; and another reason is that Eq. (3.40) is only an upper bound for 1D case and the actual melting point may be higher. Therefore, all our results

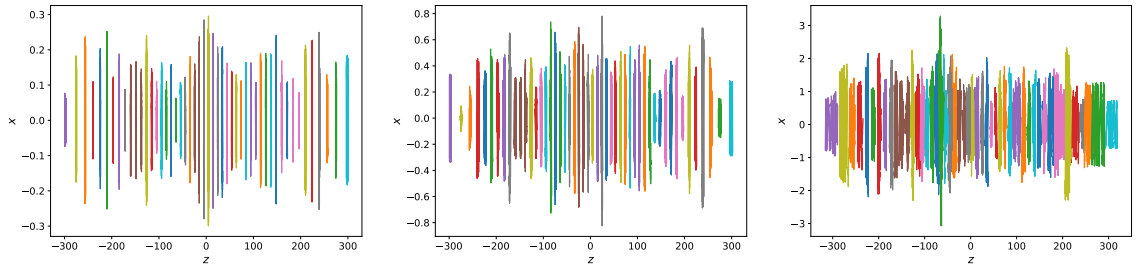

(a) (b) (c)

Figure 3.10: Trajectories (projected onto the z-x plane) for the last 100 RF periods during a 1000-period evolution. There are 50 $^{171}Yb^{+}$ ions in a trap with parameters $\boldsymbol{a} = (-2 \times 10^{-5}, -3 \times 10^{-5}, 5 \times 10^{-5})$ and $\boldsymbol{q} = (0.3, -0.3, 0)$. The initial positions of the ions are right at their equilibrium positions when the phase of the RF field is 0, while the initial velocities follow a Maxwell-Boltzmann distribution with (a) $T = 0.01\,\mathrm{K}$, (b) $T = 0.1\,\mathrm{K} \approx T_c$ and (c) $T = 1\,\mathrm{K}$. Axes are not to scale.

are consistent with each other.

3.1.5 Soft Modes in Large Ion Crystals

As we have already seen in Fig. 3.1, there are low-frequency normal modes in the ion crystals, namely the soft modes. This can be a problem for quantum computing because even weak excitation in these modes can lead to large amplitude.

In Fig. 3.11(a) we show the frequency of the lowest mode β_1 vs. the system size N in a trap with $\boldsymbol{a} = (-0.015, -0.015, 0.03)$ and $\boldsymbol{q} = (0.3, -0.3, 0)$. It seems that the soft mode frequency is going down with N, but there is not a clear scaling relation. These soft modes are generally rotational modes in 2D or 3D. One example is shown in Fig. 3.11(b) for $N = 100$. Note that even for a fixed N there can be multiple equilibrium configurations in the trap and they may have different soft mode frequencies. Some high data points in Fig. 3.11 such as that for $N = 20$ indicate that there are some configurations that are more "stable" than

the others.

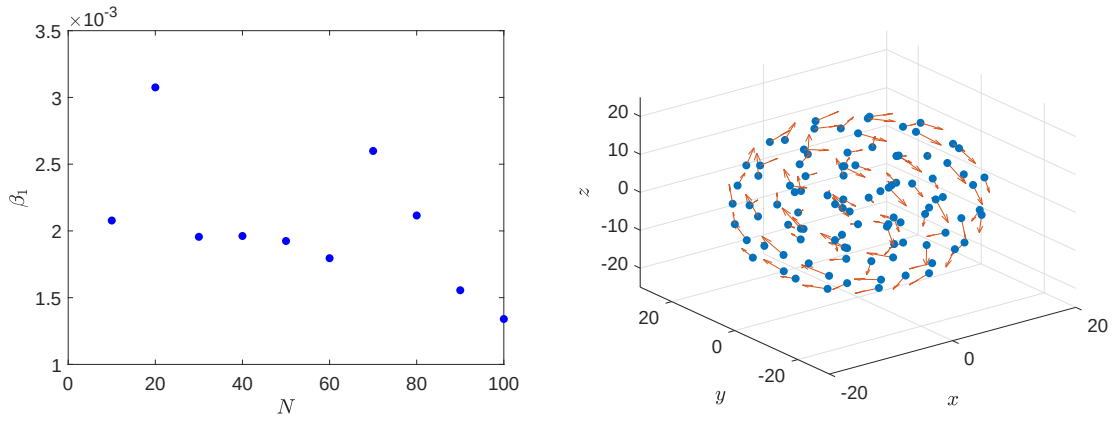

(a) (b)

Figure 3.11: (a) Lowest mode frequency β_1 (in the unit of $\omega_{\rm rf}/2$) vs. ion number N in a trap with $\boldsymbol{a} = (-0.015, -0.015, 0.03)$ and $\boldsymbol{q} = (0.3, -0.3, 0)$. (b) Mode vectors of each ion for $N = 100$.

It is much easier to find the equilibrium positions and the corresponding mode frequencies for ions in a static pseudo-potential. Although it is not a good approximation for large a and q parameters, it may still help us to understand the scaling of the soft modes. In Fig. 3.12 we show the lowest mode frequency for up to $N = 5000$ ions in a static harmonic trap with $\omega_x = 0.16$, $\omega_y = 0.17$ and $\omega_z = 0.18$ [$\boldsymbol{a} = (0.16^2, 0.17^2, 0.18^2)$ and $\boldsymbol{q} = (0, 0, 0)$]. A rough scaling of $\beta_1 \propto N^{-0.26}$ is observed.

At thermal equilibrium, we expect the energy to distribute evenly in each normal mode, thus the energy of the soft mode will not explode even if its amplitude is large. In this sense, the soft mode should not lead to a direct melting of the crystal, which is consistent with our previous result of a finite melting point. However, the large amplitude does break the small-perturbation approximation we made in Sec. 3.1.3; whether there can be long-term RF heating effect is not clear, and need to be studied with the numerical methods we described

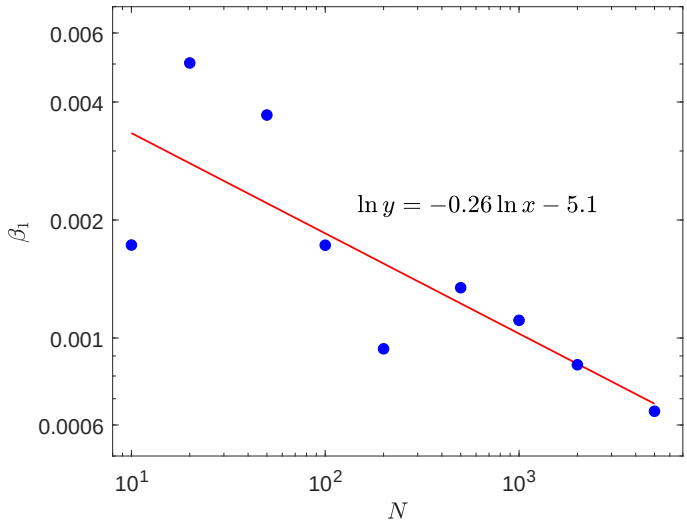

Figure 3.12: Lowest mode frequency β_1 vs. ion number N in a static harmonic trap with $\omega_x = 0.16$, $\omega_y = 0.17$ and $\omega_z = 0.18$.

in Sec. 3.1.4.

On the other hand, the large amplitude of the soft mode does have an immediate consequence. When applying quantum gates, we typically use narrow laser beams to selectively drive the chosen ions. Now if the oscillation amplitude is large, the target ion can leave the region of the laser beam and moreover the nearby ions may enter the region. This is probably not a fundamental limit for ion trap quantum computing, but more sophisticated control techniques may be needed for individual ion addressing; or we may need to cool the ion crystal, or at least the soft mode, to very low temperature before we apply the gates.

Fortunately, once cooled to low temperature, the soft mode is not very sensitive to the other heating sources. According to Sec. 1.2.2, one dominant heating source in ion trap is the electric noise, and it only heats up the center-of-mass modes which are at high frequencies. Another potential heating source is the collision with the background gases, which is esti-

mated to be infrequent in Sec. 1.2.2; thus we may just consider a single collision. Since there are $3N$ orthogonal normal modes, a random velocity kick from the collision with background gases will have a projection of $1/\sqrt{3N}$ on the soft mode. Therefore if the decrease of the mode frequency is slower than $1/\sqrt{N}$, e.g. the $N^{-0.26}$ scaling we observed in Fig. 3.12, the amplitude of the soft mode due to such a single collision will not explode in the large N limit.

3.2 Parallel Entangling Gates in Large Crystal

In this section we examine how the entangling gates can be parallelized in a large ion crystal. The key point in this scheme is that the influence of a locally driven ion on the other ions goes down quickly with their distance, so that entangling gates on distant ion pairs can be applied at the same time without much crosstalk. This fact also suggests that when designing the entangling gate between two ions, we can neglect all the ions far away, hence the complexity of optimizing the gate performance does not increase with the total size of the ion crystal.

This section is based on a paper that will be submitted soon [87], and the author is responsible for all the works presented here. It is organized in the following way: first we consider an infinite ion chain with uniform spacing for simplicity and study how the crosstalk between two entangling gates scales with the distance. This assumption of a uniform chain is just to simplify our derivation; neither the gate design nor their parallelization relies on it. For realistic ion crystals the spacing is never uniform, but good approximations can be achieved by adjusting the electric potential along the axial direction (see Sec. 2.1.1). Then in Sec. 3.2.2 we generalize the result to 2D ion crystals.

3.2.1 Entangling Gates on Uniform Infinite Ion Chain

Consider an infinite ion chain along the z axis with uniform spacing d. The ions can be labelled by integers with ion j located at $z_j = jd$. Suppose the trapping potential along the x direction is harmonic with trapping frequency ω_x, then the transverse oscillation modes in this direction can be expressed as travelling waves

$$b_j^k = \frac{1}{\sqrt{N}} e^{ikz_j}, \tag{3.41}$$

where N is the number of ions and we will later take the limit $N \to \infty$. The mode frequencies are

$$\omega_k = \omega_x \sqrt{1 - \frac{e^2}{4\pi\epsilon_0 d^3 m\omega_x^2} \sum_{j\neq 0} \frac{1-\cos jkd}{|j|^3}} \tag{3.42}$$

$$= \omega_x \sqrt{1 - \frac{e^2}{4\pi\epsilon_0 d^3 m\omega_x^2} 2\left[\zeta(3) - S(kd)\right]}, \tag{3.43}$$

where m and e are the mass and the charge of the ion, ζ the Riemann zeta function and $S(x) \equiv \sum_{j=1}^{\infty} \cos jx/j^3$.

Let us define $\epsilon = e^2/4\pi\epsilon_0 d^3 m\omega_x^2$, which characterize the narrowness of the spectrum of the transverse phonon modes. As we have seen in Chapter 2, it is typically a small parameter. Then we can make the approximation

$$\omega_k \approx \omega_x \left\{1 - \epsilon\left[\zeta(3) - S(kd)\right]\right\}. \tag{3.44}$$

Recall that an XX entangling gate between ion i and ion j takes the form [Eq. (2.31)]

$U_{\text{ideal}} = e^{\pm i\pi\sigma_i^x\sigma_j^x/4}$, while the actual gate we implement is [Eq. (2.23)]

$$U_I(\tau) \approx \exp\left(i\sum_j \phi_j(\tau)\sigma_j^n + i\sum_{i<j}\Theta_{ij}(\tau)\sigma_i^n\sigma_j^n\right), \tag{3.45}$$

where

$$\phi_j(\tau) = -i\sum_k \left[\alpha_j^k(\tau)a_k^\dagger - \alpha_j^{k*}(\tau)a_k\right], \tag{3.46}$$

$$\alpha_j^k(\tau) = -\frac{i}{\hbar}\eta_k b_j^k \int_0^\tau \chi_j(t)e^{i\omega_k t}dt, \tag{3.47}$$

and

$$\Theta_{ij}(\tau) = \frac{1}{\hbar^2}\sum_k \eta_k^2 b_i^k b_j^k \int_0^\tau dt_1 \int_0^{t_1} dt_2 \left[\chi_i(t_1)\chi_j(t_2) + \chi_j(t_1)\chi_i(t_2)\right]\sin\left[\omega_k(t_1-t_2)\right], \tag{3.48}$$

with $\chi_j(t) \equiv \hbar\Omega_j(t)\sin(\mu t + \varphi_j^{(m)})$ describing the laser sequence we apply. The ψ_j terms in Eq. (2.23) is not shown here because their influence to the gate fidelity is of the order $O(\eta_k^4)$ and is thus neglected in Eq. (2.53):

$$F \approx 1 - \frac{4}{5}\sum_k \left(|\alpha_i^k|^2 + |\alpha_j^k|^2\right)\coth\frac{\hbar\omega_k}{2k_BT}, \tag{3.49}$$

if we set $\Theta_{ij} = \pm\pi/4$ by suitably rescaling the laser intensity.

When parallelizing multiple entangling gates, we simply turn on all the laser beams at the same time. Suppose we want to implement two XX entangling gates between ions i_1 and j_1, and between i_2 and j_2. Now the ideal gate is the tensor product of the two gates: $U_{\text{ideal}} = \exp(\pm i\pi\sigma_{i_1}^x\sigma_{j1}^x/4 \pm i\pi\sigma_{i_2}^x\sigma_{j_2}^x/4)$, while what we really get still takes the form of Eq. (3.45) with the summation indices running over i_1, j_1, i_2 and j_2.

From Eq. (3.49) it is clear that the intrinsic gate errors due to the residual entanglement to the phonon modes add up together, because each α_j^k term only relies on the laser driving on that ion. From Eq. (3.48) we can see that the two-ion rotation angle $\Theta_{i_1 j_1}$ only depends on the laser driving on ions i_1 and j_1 and is not affected by the other driving on ions i_2 and j_2, so its value stays at $\pm\pi/4$ as we design it; the same argument holds for $\Theta_{i_2 j_2}$. However, now we have four additional crosstalk terms between i_1, j_1 and i_2, j_2. Because all these Pauli X operators commute with each other, what we get is the two original gates $XX_{i_1 j_1} \circ XX_{i_2 j_2}$ (including the intrinsic errors from the gate design) followed by an additional unitary channel $\mathcal{E}(\rho) = E\rho E^\dagger$ with

$$E = \exp\left[i \sum_{r=i_1,j_1} \sum_{s=i_2,j_2} \Theta_{rs} \sigma_r^x \sigma_s^x \right]. \tag{3.50}$$

As we have discussed in Sec. 2.2.3, for the purpose of quantum computing and in particular quantum error correction, it is desired to characterize the error by diamond norm. The diamond norm is generally difficult to compute, but luckily for a unitary channel $\mathcal{E}$ it can be easily bounded as [88]

$$\frac{1}{2}\|\mathcal{E}\|_\diamond \leq |\Theta_{i_1 i_2}| + |\Theta_{i_1 j_2}| + |\Theta_{j_1 i_2}| + |\Theta_{j_1 j_2}|. \tag{3.51}$$

Two entangling gates can be parallelized if $\|\mathcal{E}\|_\diamond \ll 1$.

Suppose we already have the design of two entangling gates with small intrinsic error δF. (We have seen how to do this for small to medium-sized ion crystals in Chapter 2; later in this subsection we will discuss how this can be done efficiently for large crystals.) Now we want to study how $\|\mathcal{E}\|_\diamond$ scales with the distance between the two ion pairs. It suffices to show how Θ_{ij} scales with $|i-j|$.

Analytical Result for the Scaling of Crosstalk

Before we start, note that the derivation of Eq. (3.48) assumes real mode vectors b_j^k; while now our mode vectors are travelling waves [Eq. (3.41)], which take complex values. For complex mode vectors we can derive a similar expression

$$\Theta_{ij} = \frac{1}{\hbar^2} \sum_k \eta_k^2 \cdot \mathrm{Im}\left\{ \int_0^\tau dt_1 \int_0^{t_1} dt_2 \left[b_i^{k*} b_j^k \chi_i(t_1)\chi_j(t_2) + b_j^{k*} b_i^k \chi_j(t_1)\chi_i(t_2) \right] e^{i\omega_k(t_1-t_2)} \right\}, \quad (3.52)$$

if we attach b_j^k to the annihilation operator a_k and b_j^{k*} to $a_k^\dagger$. With this convention, in Eq. (3.47) the b_j^k should also be replaced by b_j^{k*}, but since we will take the absolute value when optimizing the gate fidelity, this modification does not matter.

Plugging in the travelling wave mode vectors Eq. (3.41) we get

$$\begin{aligned}\Theta_{ij} =& \frac{1}{\hbar^2 N} \sum_k \eta_k^2 \int_0^\tau dt_1 \int_0^{t_1} dt_2 \Big\{ \left[\chi_i(t_1)\chi_j(t_2) + \chi_j(t_1)\chi_i(t_2)\right] \sin\omega_k(t_1-t_2) \cos k(z_j - z_i) \\ &+ \left[\chi_i(t_1)\chi_j(t_2) - \chi_j(t_1)\chi_i(t_2)\right] \cos\omega_k(t_1-t_2) \sin k(z_j - z_i) \Big\}. \end{aligned} \quad (3.53)$$

We further replace $\frac{1}{N}\sum_k$ with $\frac{d}{2\pi}\int dk$ and change the order of integration. Without loss of generality we assume $j > i$ and define $z_j - z_i = nd$. Because we are interested in the scaling with n, we only need to evaluate

$$\int_{-\pi}^{\pi} d(kd) \eta_k^2 \sin\omega_k(t_1-t_2) \cos nkd, \quad (3.54)$$

and

$$\int_{-\pi}^{\pi} d(kd) \eta_k^2 \cos\omega_k(t_1-t_2) \sin nkd, \quad (3.55)$$

while the rest part of Θ_{ij} only depends on the laser sequence on the ions but not on their distance. Here we calculate the first term as an example, the second one can be treated similarly.

Let us define $\phi = \omega_x(t_1 - t_2)[1 - \epsilon\zeta(3)]$ and $\lambda = \epsilon\omega_x(t_1 - t_2)$. They are functions of t_1 and t_2, but since we are considering the scaling with n, we can treat them as constants. η_k depends on k as $\eta_k^2 = \eta_0^2\omega_x/\omega_k$, where η_0 is a constant independent of k. Hence we can approximate η_k by η_0 with an error of ϵ. Then we have

$$\begin{aligned} &\int_{-\pi}^{\pi} d(kd) \sin\omega_k(t_1 - t_2) \cos nkd \\ =&\int_{-\pi}^{\pi} dx \left\{\sin\phi\cos[\lambda S(x)] + \cos\phi\sin[\lambda S(x)]\right\}\cos nx. \end{aligned} \tag{3.56}$$

Again we consider the first term as an example, while the second term can be calculated in the same way. Plugging in the series expansion forms $\cos x = \sum_{\alpha=0}^{\infty}(-1)^\alpha x^{2\alpha}/(2\alpha)!$ and $S(x) = \sum_{\beta=1}^{\infty}\cos\beta x/\beta^3$, we get

$$\int_{-\pi}^{\pi} dx \cos[\lambda S(x)]\cos nx = \sum_{\alpha=0}^{\infty}\frac{(-1)^\alpha}{(2\alpha)!}\int_{-\pi}^{\pi} dx \left(\lambda\sum_{\beta=1}^{\infty}\frac{\cos\beta x}{\beta^3}\right)^{2\alpha}\cos nx. \tag{3.57}$$

Now we argue that this expression has a scaling of $1/n^3$. First, note that for a given α, the integrand can be expanded into a series

$$\sum_{\{\beta_j\}}\lambda^{2\alpha}\cos nx\prod_{j=1}^{2\alpha}\frac{\cos\beta_j x}{\beta_j^3}, \tag{3.58}$$

with each term being a product of $(2\alpha + 1)$ cosine functions and the integration over their common period; therefore the integral is nonzero only if a resonance condition $n \pm \beta_1 \pm \beta_2 \pm$

$\cdots \pm \beta_{2\alpha} = 0$ is satisfied, and in such cases it can be loosely bounded by

$$\left| \int_{-\pi}^{\pi} dx \cos nx \prod_{j=1}^{2\alpha} \cos \beta_j x \right| \leq \int_{-\pi}^{\pi} dx |\cos nx| \cdot \prod_{j=1}^{2\alpha} |\cos \beta_j x| \leq \int_{-\pi}^{\pi} dx \cdot 1 = 2\pi. \tag{3.59}$$

Furthermore, the dominant term of Eq. (3.58) should contain one and only one β_j of the order $O(n)$; all the other $(2\alpha - 1)$ β_j's must be bounded by constant, say, $C/2$, otherwise its coefficient will decay faster than $1/n^3$. Admittedly, for α of the order $O(n)$ all the β_j's can be of the order $O(1)$, but then the $1/(2\alpha)!$ factor in Eq. (3.57) itself decays faster than $1/n^3$.

There are in total $2\alpha C^{2\alpha-1}$ such terms in Eq. (3.58): first we choose which one of the 2α β_j's takes the order of $O(n)$; then we assign the other $(2\alpha - 1)$ β_j's within $[1, C/2]$ and choose their signs in the resonance condition to be positive or negative; once we determine these values, the last one is automatically fixed from the resonance condition. Therefore finally Eq. (3.57) is bounded by

$$2\pi \sum_{\alpha=1}^{\infty} \frac{2\alpha C^{2\alpha-1} \lambda^{2\alpha}}{(2\alpha)!} \frac{1}{n^3} = \frac{2\pi\lambda \sinh \lambda C}{n^3} \propto \frac{1}{n^3}. \tag{3.60}$$

Note that λ actually depends on t_1 and t_2, but here we only consider the scaling with respect to n. Nevertheless, for typical parameters, $|\lambda| \leq \epsilon\omega_x\tau$ is of the order $O(1)$.

Similar argument applies to the other terms in Eq. (3.55) and Eq. (3.56), therefore we conclude that the crosstalk term Θ_{ij} decays with the ion spacing $n = |i - j|$ as $1/n^3$. If originally the gates are designed for two ions at a distance of m, and if the minimal distance between the two pairs of ions is n, then the crosstalk terms will be $O[(m/n)^3]$ when the two gates are applied simultaneously. (Note that Θ_{ij} is designed to be $\pm\pi/4$ when $|i - j| = m$.) In other words, the error due to the parallelization of the gates is $\|\mathcal{E}\|_\diamond = O[(m/n)^3]$.

Numerical Results

In the above derivation, we have made several approximations to get an analytical result. Thus it is desirable to verify the scaling numerically without these approximations at least for some special cases. Before this, let us first consider how to design the entangling gates efficiently in a large ion crystal.

We have proven that the distant ions have little effect on the fidelity of an entangling gate, which suggests that when designing the gate we can ignore all the ions far away and focus on a finite number of ions. This is verified numerically by the example shown in Fig. 3.13, where we consider gate design in uniform ion chains with $d = 8\,\mu$m but varying the total number of ions and the position of the ion pair inside the chain. The optimal gate design and the intrinsic infidelity for these cases are almost identical as they overlap with each other in the plot.

Now we consider the scaling of the crosstalk term $|\Theta_{ij}|$ vs. the ion distance $n = |i - j|$. For the convenience of numerical calculation, we consider a finite chain of $N = 100$ ions, again with $d = 8\,\mu$m. The gate design is chosen to be the same as that in Fig. 3.13, i.e. a nearest-neighbor ion pair, $n_{\text{seg}} = 6$ segments, gate time $\tau = 50\,\mu$s and detuning $\mu = 1.016\omega_x$. In Fig. 3.14 we plot $|\Theta_{ij}|$ vs. n in the log-log form. Θ_{ij} is computed by applying the same laser sequence on ion $i = 51$ and ion $j = 52, \cdots, 100$, respectively, thus changing the value of n. Note that when $n = 1$ we have $|\Theta_{ij}| = \pi/4$. A $1/n^3$ scaling is clear for large n. Similarly, we plot the scaling of entangling gates designed for ion pairs at a distance of 3 and 5 in Fig. 3.15 and observe a similar scaling of $1/n^3$. Also note that here we assume the same gate design for the two parallel gates (identical laser sequence on ions i and j) only for the convenience of evaluating Θ_{ij} [Eq. (3.48)] numerically. The derivation of the $1/n^3$ scaling does not rely

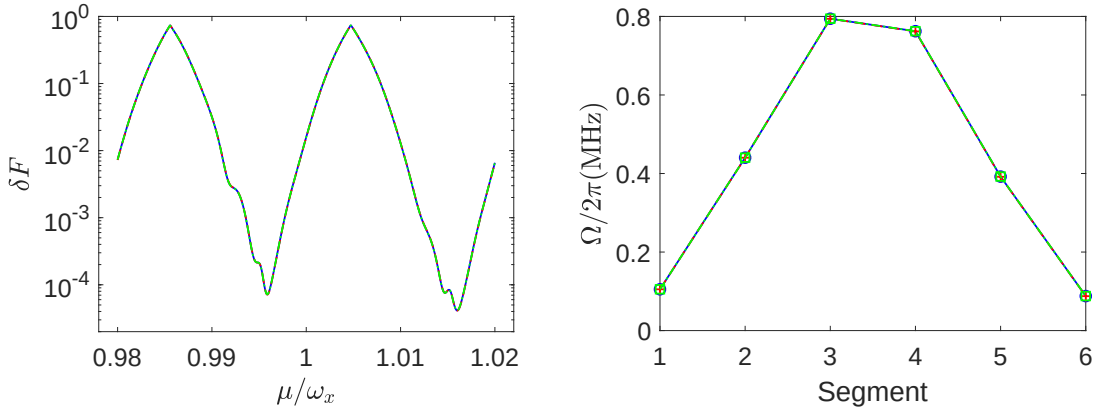

(a) (b)

Figure 3.13: (a) Optimal gate infidelity vs. laser detuning μ for $n = 6$ segments and a total gate time $\tau = 50\,\mu$s. (b) Rabi frequencies for each segment when $\mu = 1.016\omega_x$ is chosen at the minimizer of (a). The gate design is optimized through amplitude modulation, as we described in Sec. 2.1. There are 3 curves in each plot, blue solid line for $N = 50$ ions and ion pair 25 and 26, red dashed line for $N = 50$ ions and ion pair 10 and 11, and green dash-dotted line for $N = 100$ ions and ion pair 50 and 51. All these curves coincide within the resolution of the figure. Here we choose an ion spacing $d = 8\,\mu$m, Lamb-Dicke parameter $\eta_0 = 0.1$, transverse trapping frequency $\omega_x = 2\pi \times 3\,$MHz and 0.5 phonon per mode.

on this assumption and holds for parallelizing two different entangling gates.

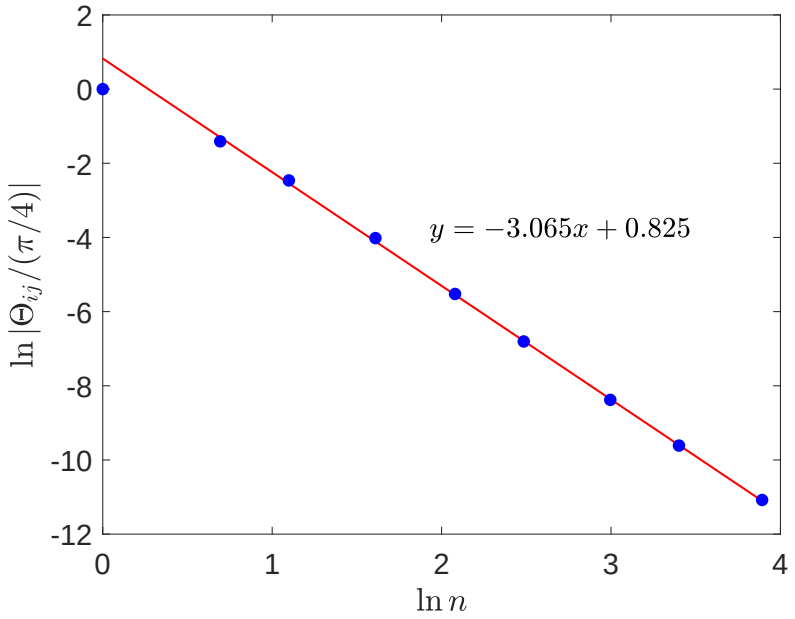

Figure 3.14: Log-log plot for crosstalk term $|\Theta_{ij}|$ vs. ion distance $n = |i - j|$. The gate is designed for a nearest-neighbor pair of ions with $\tau = 50\,\mu$s, $n_{\text{seg}} = 6$ segments, and $\mu = 1.016\omega_x$. The red line is fitted from the last five data points.

Parallelize Multiple Gates

The above result can directly be applied to parallelize multiple gates. Suppose we want to build a quantum circuit with XX entangling gates between all possible ion pairs whose distance is less than or equal to m [see Fig. 3.16, m is of the order $O(1)$]. We can divide these gates into $O[m(n+m)]$ layers and in each layer the gates are separated by a distance of at least n. In this way, the error per gate in each layer will be $O[(m/n)^3]$. Hence for a given error rate per gate ϵ, the number of required layers will be independent of the size of the crystal, which indicates scalability.

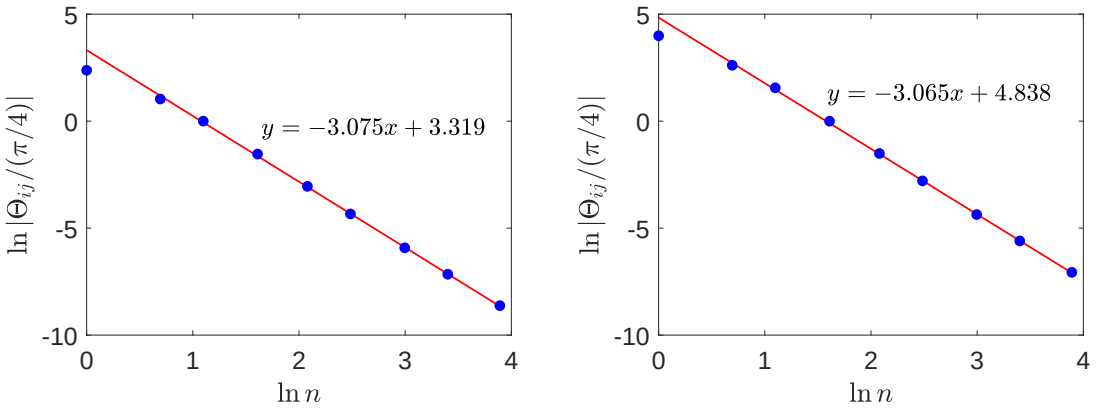

Figure 3.15: $|\Theta_{ij}|$ vs. $n = |i - j|$ for (a) a gate designed for two ions at a spacing of 3 separations with $\tau = 60\,\mu$s, $n_{\text{seg}} = 7$ segments, $\mu = 1.01403\omega_x$, (b) a gate designed for two ions at a spacing of 5 separations with $\tau = 100\,\mu$s, $n_{\text{seg}} = 10$ segments, $\mu = 1.01387\omega_x$. The red lines are fitted from the last five data points in each figure.

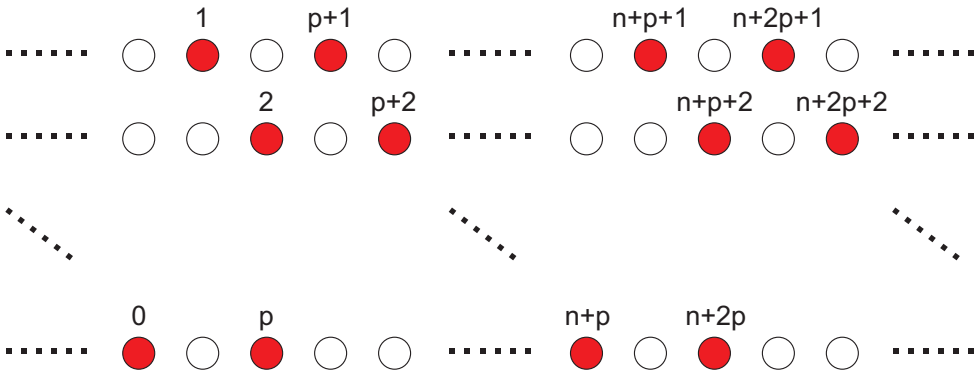

Figure 3.16: Partial illustration of the scheme to parallelize gates. $(n + p)$ layers are needed for all possible pairs of ions at a distance of p while maintaining a distance of n between any two pairs. For $p = 1, 2, \cdots, m$ we need $O[m(n + m)]$ layers in total.

3.2.2 2D Ion Crystal

Now we generalize our results to 2D. Due to the Coulomb interaction between the ions, a 2D ion crystal usually approximates a hexagonal lattice. Therefore here we consider a hexagonal lattice with translational symmetry (Fig. 3.17), although the same analysis can also be applied to other types of 2D lattices.

Let the crystal lie on the x-y plane. It can be characterized by its lattice vectors

$$\boldsymbol{a}_1 = d\,(1,\,0,\,0)\,, \qquad \boldsymbol{a}_2 = d\left(\frac{1}{2},\,\frac{\sqrt{3}}{2},\,0\right), \tag{3.61}$$

with the corresponding reciprocal vectors

$$\boldsymbol{b}_1 = \left(1,\,-\frac{1}{\sqrt{3}},\,0\right), \qquad \boldsymbol{b}_2 = \left(0,\,\frac{2}{\sqrt{3}},\,0\right). \tag{3.62}$$

The transverse oscillation modes in the z direction can be used for the entangling gates [41], which is a natural generalization of the scheme we studied in Chapter 2. In this case the normal modes are still travelling waves which can be characterized by the wave vector $\boldsymbol{k} = k_1\boldsymbol{b}_1 + k_2\boldsymbol{b}_2$ ($k_1,\,k_2 \in (-\pi/d,\,\pi/d]$). The mode vector for this travelling wave is given by

$$z^{\boldsymbol{k}}_{\alpha\beta} \propto \exp\left[i(\alpha k_1 d + \beta k_2 d)\right] \tag{3.63}$$

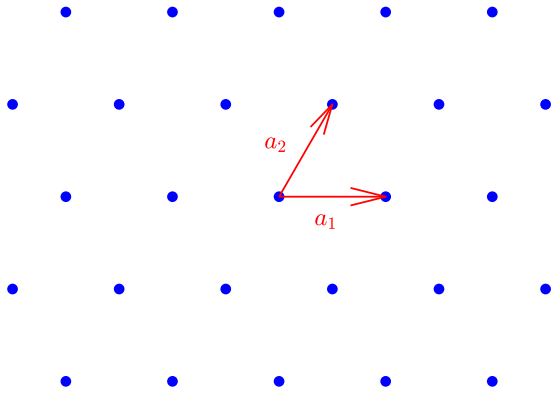

Figure 3.17: A hexagonal lattice with lattice vectors $\boldsymbol{a}_1 = d(1, 0, 0)$ and $\boldsymbol{a}_2 = d(1/2, \sqrt{3}/2, 0)$.

for the ion at position $\boldsymbol{r}_{\alpha\beta} = \alpha\boldsymbol{a}_1 + \beta\boldsymbol{a}_2$, with the corresponding eigenfrequency

$$\begin{aligned}
\omega_{\boldsymbol{k}} =& \omega_z \sqrt{1 - \frac{e^2}{4\pi\epsilon_0 d^3 m\omega_z^2} \sum_{(\alpha,\beta)}{}' \frac{1 - \cos \boldsymbol{k}\cdot\boldsymbol{r}_{\alpha\beta}}{|\alpha\boldsymbol{a}_1 + \beta\boldsymbol{a}_2|^3}} \\
=& \omega_z \sqrt{1 - \frac{e^2}{4\pi\epsilon_0 d^3 m\omega_z^2} \sum_{(\alpha,\beta)}{}' \frac{1 - \cos(\alpha k_1 d + \beta k_2 d)}{(\alpha^2 + \beta^2 + \alpha\beta)^{3/2}}} \\
\approx& \omega_z \left[1 - \frac{e^2}{4\pi\epsilon_0 d^3 m\omega_z^2} \sum_{(\alpha,\beta)}{}' \frac{1 - \cos(\alpha k_1 d + \beta k_2 d)}{2(\alpha^2 + \beta^2 + \alpha\beta)^{3/2}}\right],
\end{aligned} \tag{3.64}$$

where $\sum'$ means that the two indices for summation cannot both be 0 at the same time.

Following the same derivation as before, to study the scaling of the crosstalk error versus the distance on the lattice represented by $n\boldsymbol{a}_1 + m\boldsymbol{a}_2$, we need to evaluate some expressions

like

$$\sum_{\alpha=0}^{\infty}\frac{(-1)^{\alpha}}{(2\alpha)!}\int_{-\pi}^{\pi}dx\int_{-\pi}^{\pi}dy\left[\frac{\lambda}{2}{\sum_{\beta,\gamma}}'\frac{\cos(\beta x+\gamma y)}{(\beta^2+\gamma^2+\beta\gamma)^{3/2}}\right]^{2\alpha}\cos(nx+my). \tag{3.65}$$

Again for a given α we can expand the integrand into series:

$$\sum_{\{\beta_j,\,\gamma_j\}}\left(\frac{\lambda}{2}\right)^{2\alpha}\cos(nx+my)\prod_{j=1}^{2\alpha}\frac{\cos(\beta_j x+\gamma_j y)}{(\beta_j^2+\gamma_j^2+\beta_j\gamma_j)^{3/2}}, \tag{3.66}$$

and we get two resonance conditions $n\pm\beta_1\pm\cdots\pm\beta_{2\alpha}=0$ and $m\pm\gamma_1\pm\cdots\pm\gamma_{2\alpha}=0$, both of which need to be satisfied for a nonzero integral.

Without loss of generality, we can assume $|n|\geq|m|$. Consider two different cases: (1) only $|n|$ goes to infinity and $|m|$ stays constant. Then we go back to the previous 1D case and the coefficient decays as $1/n^3$. (2) Both $|n|$ and $|m|$ go to infinity. Then again we argue that for any given α, the 2α terms of $\{\beta_j,\,\gamma_j\}$ can only have one term of the order $O(|n|)$ and $O(|m|)$; all the other β_j's and γ_j's need to be bounded by constant. Otherwise the coefficient for their product will decay faster than $1/(n^2+m^2+nm)^{3/2}$. If we count the number of such terms and add all of them together, we will get a scaling of $1/(n^2+m^2+nm)^{3/2}$, that is, a cubic decay with the distance.

Below we show some numerical results in Figs. 3.18, 3.19 and 3.20, where we design entangling gates for different ion pairs in a 80×80 lattice with $d=8\,\mu$m and compute crosstalk Θ_{ij} explicitly when parallelizing two identical gates at different distances. To avoid the potential boundary effect, in these numerical calculations we limit ourselves to the ion pairs in the central 40×40 sublattice. Again we see that the slope is fairly close to -3.

Also note that this $1/\text{distance}^3$ scaling is not special for a hexagonal lattice. In Fig. 3.21 we see the same scaling in a square lattice. Although this type of lattice is not very realistic for

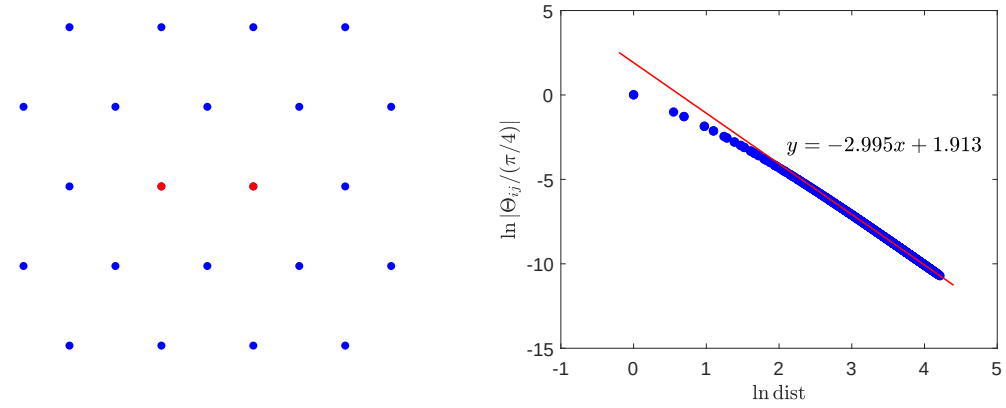

(a) (b)

Figure 3.18: Numerical results for 80×80 hexagonal lattice with ion spacing $d = 8\,\mu$m, transverse trapping frequency $\omega_z = 2\pi \times 3\,$MHz, Lamb-Dicke parameter $\eta = 0.1$ and temperature $k_B T = \hbar\omega_z$. The gate is designed for two ions in a relative position of (a). Parameters are $\tau = 60\,\mu$s, $n_{seg} = 10$ segments, $\mu = 1.01378\omega_z$.

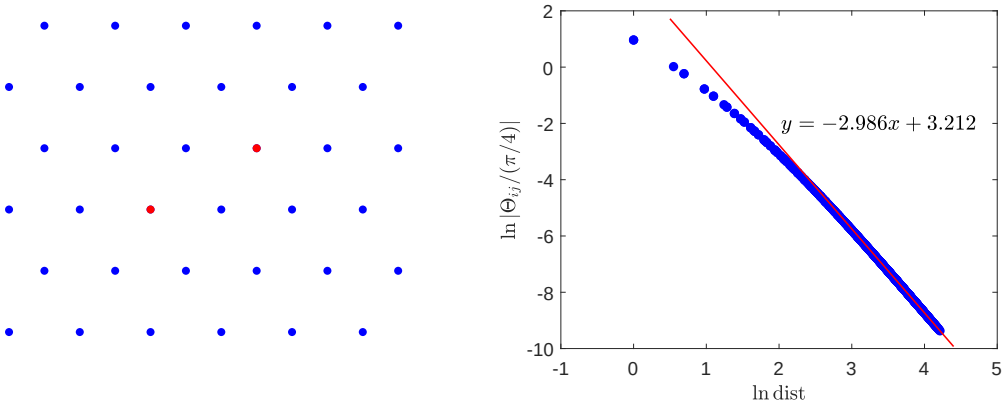

(a) (b)

Figure 3.19: Numerical results for 80×80 hexagonal lattice with ion spacing $d = 8\,\mu$m, transverse trapping frequency $\omega_z = 2\pi \times 3\,$MHz, Lamb-Dicke parameter $\eta = 0.1$ and temperature $k_B T = \hbar\omega_z$. The gate is designed for two ions in a relative position of (a). Parameters are $\tau = 100\,\mu$s, $n_{seg} = 15$ segments, $\mu = 1.01015\omega_z$.

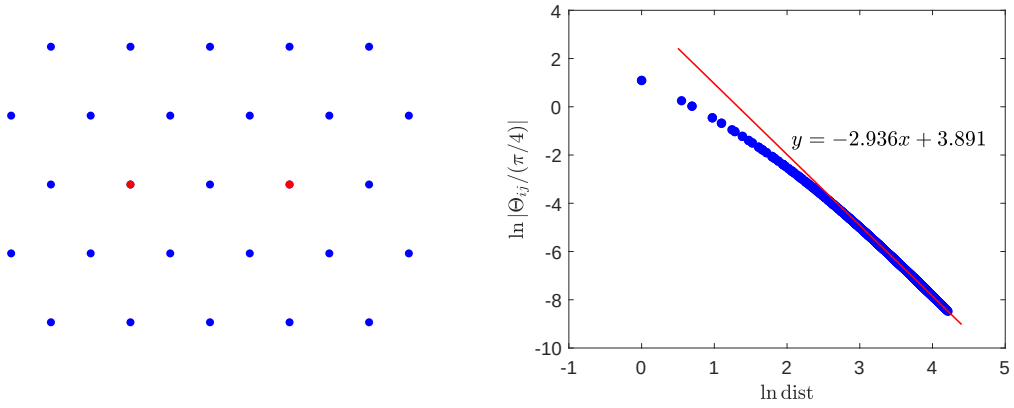

(a) (b)

Figure 3.20: Numerical results for 80×80 hexagonal lattice with ion spacing $d = 8\,\mu$m, transverse trapping frequency $\omega_z = 2\pi \times 3\,$MHz, Lamb-Dicke parameter $\eta = 0.1$ and temperature $k_B T = \hbar\omega_z$. The gate is designed for two ions in a relative position of (a). Parameters are $\tau = 150\,\mu$s, $n_{seg} = 20$ segments, $\mu = 1.00621\omega_z$.

ion crystals, the observation of the same scaling result in 1D and different types of lattices in 2D indicates that it is universal and can be applied to more general ion crystals.

3.3 Include Micromotion in Gate Design

In this section, we address the influence of micromotion on the gate design. In Chapter 2 this effect is neglected, because for 1D ion chain in a linear Paul trap it is possible to place the ions in such a way that (ideally) there is no zeroth order micromotion, while the high-frequency modulation on the normal modes is far off-resonant to the driving. However, for larger ion crystals and in particular in 2D or 3D, micromotion can become more and more significant. Thus it is desired to include its effect into the gate design.

It has been shown in Ref. [89] that the effect of micromotion, to the lowest order, can be

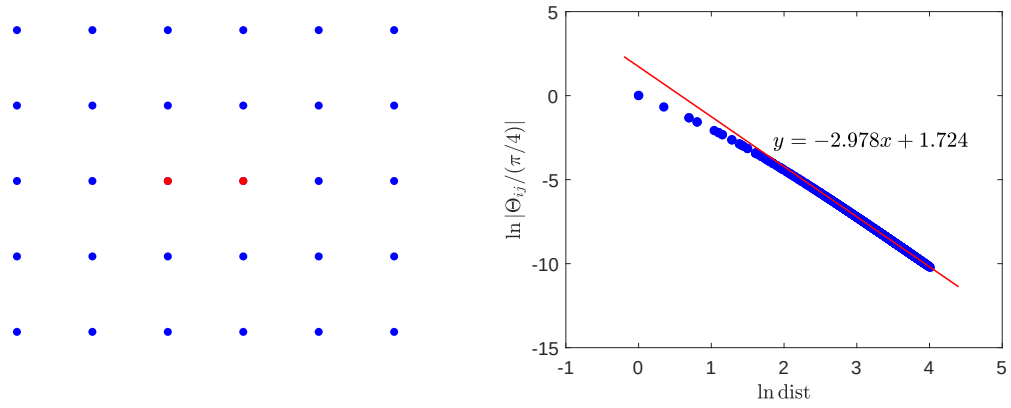

(a) (b)

Figure 3.21: Numerical results for 80×80 square lattice with ion spacing $d = 8\,\mu$m, transverse trapping frequency $\omega_z = 2\pi \times 3\,$MHz, Lamb-Dicke parameter $\eta = 0.1$ and temperature $k_B T = \hbar\omega_z$. The gate is designed for two ions in a relative position of (a). Parameters are $\tau = 60\,\mu$s, $n_{seg} = 10$ segments, $\mu = 1.01386\omega_z$.

compensated by a rescaling of the laser intensity depending on the micromotion amplitude. However, this approximation may not be adequate if we want very high gate fidelity, say, above 99.9%. In this section we extend this method to higher orders through a series expansion. Combined with the numerical solutions of micromotion and normal modes we have found in Sec. 3.1, the error in the formulation can be systematically suppressed by including higher and higher order terms.

3.3.1 Effects of Micromotion

Recall that, for an ion crystal without micromotion, the design of entangling gates turns into minimizing the residual entanglement to the phonon modes [Eq. (3.47)]

$$\alpha_j^k(\tau) = -\frac{i}{\hbar}\eta_k b_j^{k*} \int_0^\tau \chi_j(t) e^{i\omega_k t} dt, \tag{3.67}$$

while maintaining the desired two-qubit phase $\Theta_{ij} = \pm\pi/4$ [Eq. (3.52)]

$$\Theta_{ij} = \frac{1}{\hbar^2}\sum_k \eta_k^2 \cdot \mathrm{Im}\left\{ \int_0^\tau dt_1 \int_0^{t_1} dt_2 \left[b_i^{k*} b_j^k \chi_i(t_1)\chi_j(t_2) + b_j^{k*} b_i^k \chi_j(t_1)\chi_i(t_2) \right] e^{i\omega_k (t_1 - t_2)} \right\}, \quad (3.68)$$

where

$$\chi_j(t) \equiv \hbar\Omega_j(t) \sin\left(\mu t + \varphi_j^{(m)}\right). \quad (3.69)$$

The advantage of the segmented amplitude modulation we considered in Sec. 2.1 is that $\Omega_j(t)$ is now piecewise-constant and hence the above time integrations can be performed analytically on each segment. Then this optimization problem turns into a generalized eigenvalue problem [Eq. (2.55)], and thus can be efficiently solved.

Strictly speaking, in the above process the analytical expression for the time integral is not necessary: once we choose a gate time τ and the number of segments n_{seg}, we can plug in these numbers into the lower and upper limits of the integral and evaluate it numerically. However, for the oscillatory functions we are considering, this will require very high numerical accuracy and usually takes long time to perform; in comparison, if we can derive an analytical expression, the evaluation of the integral becomes much easier and thus we get a practical algorithm to optimize the gate design.

Now we consider the influence of the micromotion on the gate performance. It appears in three aspects:

Time-Dependent Motional Phase

Instead of staying at the equilibrium configuration which minimizes the pseudo-potential, the ions in an RF trap are oscillating at the RF frequency in equilibrium. Intuitively, this is

equivalent to a (classical) oscillating phase of the laser in the form of $\boldsymbol{\Delta k}\cdot\boldsymbol{R}_j(t)$ where $\boldsymbol{R}_j(t)$ is the equilibrium trajectory of the ion j [periodic solution to Eq. (1.13)]. If we go through the derivation of Sec. 2.1.2, this effect can mathematically be described by a time-dependent motional phase $\varphi_j^{(m)}$ for each ion as appears in Eq. (3.69) with a period of $2\pi/\omega_{\mathrm{rf}}$. Thus we can expand this phase into Fourier series:

$$\varphi_j^{(m)} = \sum_{l=0}^{\infty} \varphi_j^{(l)} \cos l\omega_{\mathrm{rf}} t, \tag{3.70}$$

where the superscript "(m)" represents "motional" and will be omitted for simplicity, while "(l)" corresponds to the l-th order of expansion. Note that the amplitudes of these oscillating phases depend not only on the amplitude of the micromotion but also on its projection along the direction of the laser wave vector.

Time-Dependent Complex Normal Modes

Another effect of the micromotion is a high-frequency modulation to each normal mode, which we have seen in Sec. 3.1.2. To begin with, we consider the lowest order approximation:

$$\boldsymbol{r}^{(k)}(t) = \boldsymbol{C}_0^{(k)} \cos(\omega_k t + \phi) + \boldsymbol{C}_2^{(k)} \cos[(\omega_{\mathrm{rf}} + \omega_k)t + \phi] + \boldsymbol{C}_{-2}^{(k)} \cos[(-\omega_{\mathrm{rf}} + \omega_k)t + \phi], \tag{3.71}$$

where superscript "(k)" represents the k-th normal mode, $\boldsymbol{C}_0^{(k)}$ is the solution to an eigenvalue problem $(A + Q^2/2)\boldsymbol{C}_0^{(k)} = \beta_k^2 \boldsymbol{C}_0^{(k)}$ which gives the zeroth order normal mode, and

$$\boldsymbol{C}_{\pm 2}^{(k)} = -\frac{1}{4}(1 \mp \beta_k) Q \boldsymbol{C}_0^{(k)} \tag{3.72}$$

gives the first order correction. (We have recovered the units of the formulae, e.g. $\omega_k = \beta_k \omega_{\rm rf}/2$.) Higher order terms are omitted in this expression.

We can express two independent general solutions to Eq. (3.12) at this order as

$$\boldsymbol{u}^{(k)}(t) = \left(I - \frac{1}{2} Q \cos \omega_{\rm rf} t - \frac{i}{2} \beta_k Q \sin \omega_{\rm rf} t \right) \boldsymbol{C}_0^{(k)} e^{-i\omega_k t} \tag{3.73}$$

and its complex conjugate $\boldsymbol{u}^{(k)*}(t)$. The initial conditions are $\boldsymbol{u}^{(k)}(0) = (I - Q/2)\boldsymbol{C}_0^{(k)}$ and $\dot{\boldsymbol{u}}^{(k)}(0) = -i\omega_k (I + Q/2)\boldsymbol{C}_0^{(k)}$.

Now note that the quantum operators for the small displacements around the equilibrium trajectories $\hat{\boldsymbol{r}}(t)$ satisfy the same set of linear differential equations as $\boldsymbol{u}^{(k)}(t)$. Following a similar derivation as Sec. IIB of Ref. [20], we find that the Wronskian determinant $\boldsymbol{u}^{(k)\dagger}(t)\dot{\hat{\boldsymbol{r}}}(t) - \dot{\boldsymbol{u}}^{(k)\dagger}(t)\hat{\boldsymbol{r}}(t)$ is a constant and should be proportional to the annihilation operator $\hat{a}_k$ for the mode k. Actually, for suitably normalized $\boldsymbol{u}^{(k)}(t)$, we have

$$\hat{\boldsymbol{r}}(t) = \sum_k \sqrt{\frac{\hbar}{2m\omega_k}} \left[\hat{a}_k \boldsymbol{u}^{(k)}(t) + \hat{a}_k^\dagger \boldsymbol{u}^{(k)*}(t) \right] \tag{3.74}$$

with $[\hat{a}_k, \hat{a}_l^\dagger] = \delta_{kl}$.

Using the canonical commutation relation of $\hat{\boldsymbol{r}}(0)$ and $\hat{\boldsymbol{p}}(0) = m\dot{\hat{\boldsymbol{r}}}(0)$: $[\hat{r}_{i\sigma}(0), \hat{p}_{j\rho}(0)] = i\hbar\delta_{ij}\delta_{\sigma\rho}$, we find the correct normalization for $\boldsymbol{C}_0^{(k)}$:

$$(I - Q/2) \sum_k \left(\boldsymbol{C}_0^{(k)} \boldsymbol{C}_0^{(k)T} \right) (I + Q/2) = I, \tag{3.75}$$

or

$$\sum_k \left(\boldsymbol{C}_0^{(k)} \boldsymbol{C}_0^{(k)T} \right) = I, \tag{3.76}$$

if we approximate $(I + Q/2)(I - Q/2) \approx I$. This is directly satisfied by the orthonormal condition $\boldsymbol{C}_0^{(k)T}\boldsymbol{C}_0^{(l)} = \delta_{kl}$ of the eigenvalue problem we solved above.

Now it is clear that the effect of micromotion is to replace the mode vector b_j^k related to the mode $\hat{a}_k$ in the pseudo-potential case [e.g. Eq. (3.67) and Eq. (3.68)] by a time-dependent one

$$b_j^k \sim \boldsymbol{C}_0^{(k)} \to \left(I - \frac{1}{2}Q\cos\omega_{\mathrm{rf}}t - \frac{i}{2}\beta_k Q\sin\omega_{\mathrm{rf}}t\right)\boldsymbol{C}_0^{(k)}. \tag{3.77}$$

This leads to a time-dependent multiplicative factor in the integration of α_j^k [Eq. (3.67)] and Θ_{ij} [Eq. (3.68)], but as it is a trigonometric function, an analytical expression for the integral can still be found. Also note that our previous expression of Θ_{ij} [Eq. (2.28)] is derived for a real mode vector; now our mode vector is complex and hence Eq. (3.68) should be used.

The same analysis also applies to higher order expansion of the normal modes. From Sec. 3.1.2 we know that at one order higher $\boldsymbol{C}_0^{(k)}$ will be a solution to the generalized eigenvalue problem

$$\left[A + \frac{1}{2}Q^2 + \frac{1}{8}QAQ + \frac{1}{128}Q^4\right]\boldsymbol{C}_0^{(k)} = \beta^2\left(1 - \frac{3}{8}Q^2\right)\boldsymbol{C}_0^{(k)} \tag{3.78}$$

and we have $\boldsymbol{C}_{\pm 2}^{(k)} = -(1 \mp \beta_k)Q\boldsymbol{C}_0^{(k)}/4$ and $\boldsymbol{C}_{\pm 4}^{(k)} = (1 \mp 3\beta_k/2)Q^2\boldsymbol{C}_0^{(k)}/64$.

To this order of approximation, the general solution can be represented as

$$\begin{aligned}\boldsymbol{u}^{(k)}(t) = &\left(I - \frac{1}{2}Q\cos\omega_{\mathrm{rf}}t - \frac{i}{2}\beta_k Q\sin\omega_{\mathrm{rf}}t\right.\\ &\left. + \frac{1}{32}Q^2\cos 2\omega_{\mathrm{rf}}t + \frac{3i}{64}\beta_k Q^2\sin 2\omega_{\mathrm{rf}}t\right)\boldsymbol{C}_0^{(k)}e^{-i\omega_k t}\end{aligned} \tag{3.79}$$

and its complex conjugate. The initial conditions are $\boldsymbol{u}^{(k)}(0) = (I - Q/2 + Q^2/32)\boldsymbol{C}_0^{(k)}$ and

$\dot{\boldsymbol{u}}^{(k)}(0) = -i\omega_k(I + Q/2 - 5Q^2/32)\boldsymbol{C}_0^{(k)}$. Again we use Eq. (3.74) as the expansion for the displacement operators. This time the normalization condition gives

$$\left(I - \frac{Q}{2} + \frac{Q^2}{32}\right) \sum_k \left(\boldsymbol{C}_0^{(k)T} \boldsymbol{C}_0^{(k)}\right) \left(I + \frac{Q}{2} - \frac{5Q^2}{32}\right) = I \tag{3.80}$$

or

$$\sum_k \left(\boldsymbol{C}_0^{(k)T} \boldsymbol{C}_0^{(k)}\right) = \left(I - \frac{3}{8}Q^2\right)^{-1}, \tag{3.81}$$

which again is automatically satisfied by the orthonormal condition for the generalized eigenvalue problem we solved above:

$$\boldsymbol{C}_0^{(k)T} \left(I - \frac{3}{8}Q^2\right) \boldsymbol{C}_0^{(l)} = \delta_{kl}. \tag{3.82}$$

Based on the above results, we can make the conjecture that this process holds for any higher order expansions and thus also for the exact result of Sec. 3.1.2. Once we get ω_k and all the $\boldsymbol{C}_{2n}^{(k)}$ in the expansion of the normal mode, we can write down a general solution similar to Eq. (3.73) and Eq. (3.79). The normalization of this solution can be derived from the commutation relation between $\hat{\boldsymbol{r}}$ and $\hat{\boldsymbol{p}}$, and between $\hat{a}_k$ and $\hat{a}_l^\dagger$. Then we can read the time-dependent mode vectors from this expression and plug them into our formula for the gate design.

Time-Dependent Modulation of Laser Intensity

The micromotion perpendicular to the direction of the laser beam also leads to a variation in the laser intensity the ion feels during the gate. This effect will become important if the amplitude of the micromotion is comparable to the width of the laser beam. It corresponds to

a time-dependent effective Rabi frequency in Eq. (3.69), which oscillates at the RF frequency (apart from other amplitude modulation we use to optimize the gate performance) and can be expanded into Fourier series. Again they are multiplicative trigonometric functions and thus we can still get analytical expressions for α_j^k and Θ_{ij} on each segment. We will not consider this effect below because the coefficients of the Fourier series depend on the detailed shape of the laser beam.

3.3.2 Numerical Calculation with Micromotion

As is mentioned above, to efficiently optimize the gate design, we want to derive analytical expressions for Eq. (3.67) and Eq. (3.68) with piecewise constant $\Omega_j(t)$ on arbitrary intervals.

Among the three effects of micromotion we described, the second and the third are not difficult to treat because our integrand is still the product of some trigonometric function. However, the first effect of an oscillating motional phase, even if only expanded to the first order, will give us some terms like $\cos(\varphi^{(1)} \cos \omega_{\mathrm{rf}} t)$ whose integral only have analytical results on an interval at a multiple of the RF period. If we are not able to get an analytical expression, we will have to evaluate highly oscillating functions, which will be beyond our computational power.

We will tackle this problem by a series expansion of the motional phase, such that for each expansion term we still have an analytical expression for the integral, while the error of the final result can be systematically improved by adding higher order terms. The pivot of our algorithm is the following formula [90, 91]

$$\exp(i\varphi \cos \omega t) = J_0(\varphi) + 2 \sum_{n=1}^{\infty} i^n J_n(\varphi) \cos(n\omega t). \tag{3.83}$$

Note that for $0 < \varphi \ll \sqrt{n+1}$, we have

$$J_n(\varphi) \sim \frac{1}{n!}\left(\frac{\varphi}{2}\right)^n, \tag{3.84}$$

thus the terms in the above series go to 0 quickly and we can expect a fast convergence.

Residual Coupling to Phonon Modes

For the residual coupling to the phonon modes α_j^k, we want to derive an analytical expression for the following integral:

$$\int dt \sum_{n=-\infty}^{+\infty} \boldsymbol{C}_{2n,j\sigma}^{(k)} e^{in\omega_{\mathrm{rf}}t} \sin\left(\mu t + \sum_{l=0}^{\infty} \varphi_j^{(l)} \cos l\omega_{\mathrm{rf}} t\right) e^{i\omega_k t} \tag{3.85}$$

where $\sigma = x$, y, z corresponds to different spatial directions and $\boldsymbol{C}_{2n,j\sigma}^{(k)}$ is the $j\sigma$ component of the k-th mode vector at the $2n$-th order. Because $\boldsymbol{C}_{2n}^{(k)}$ goes down quickly with $|n|$ (for small trapping parameter q), we can truncate the summation over n at $\pm n_{\mathrm{cut}}$.

Furthermore, we can regard $n\omega_{\mathrm{rf}} + \omega_k$ as a new variable ω in the above expression; once we get an analytical result as a function of ω, we can plug in the value of $n\omega_{\mathrm{rf}} + \omega_k$ to compute the value for any order n. Therefore we only need to consider

$$\begin{aligned}
&\int dt \sin\left(\mu t + \sum_{l=0}^{\infty} \varphi_j^{(l)} \cos l\omega_{\mathrm{rf}} t\right) e^{i\omega t} \\
=&\frac{1}{2i}\int dt \left[e^{i(\mu t + \varphi_j^{(0)})} \prod_{l=1}^{\infty} e^{i\varphi_j^{(l)} \cos l\omega_{\mathrm{rf}} t} - c.c.\right] e^{i\omega t}.
\end{aligned} \tag{3.86}$$

We can expand $\exp(i\varphi_j^{(l)} \cos l\omega_{\mathrm{rf}} t)$ into cosine functions using Eq. (3.83). Suppose the

$\varphi_j^{(1)}$, $\varphi_j^{(2)}$, $\cdots$ terms are expanded to the order of n_1, n_2, $\cdots$, respectively, then we need to compute

$$\int dt e^{i(\mu t+\varphi_j^{(0)})} e^{i\omega t} \cos(n_1\omega_{\rm rf}t)\cos(n_2\omega_{\rm rf}t)\cdots \tag{3.87}$$

with the coefficient of this term given by $\prod_l 2i^{n_l} J_{n_l}(\varphi_j^{(l)})$. Then we sum over all possible combinations of $\{n_1, n_2, \cdots\}$ to get the total integral.

The other half of Eq. (3.86) about the complex conjugate can be computed similarly. The result will be to replace μ and $\varphi_j^{(0)}$ in Eq. (3.87) with $-\mu$ and $-\varphi_j^{(0)}$, and to take the complex conjugate of the corresponding coefficients.

It seems that the number of terms we need to evaluate is large, so that even if we have an analytical expression for Eq. (3.87) and the evaluation of a single term is fast, the total time cost may still be high. Luckily, in the small q regime the micromotion amplitude goes down quickly with the order of expansion, so $\varphi_j^{(l)}$ will be close to 0 for large l. From Eq. (3.84), we know that these terms are vanishingly small except for $n_l = 0$; but if $n_l = 0$, we have $\cos(n_l\omega_{\rm rf}t) = 1$ so that we can truncate at $l \leq L$ for some small L in Eq. (3.87). Even for the remaining $\varphi_j^{(l)}$ terms, the corresponding coefficient $J_{n_l}(\varphi_j^{(l)})$ will be vanishingly small for large n_l, so usually the number of terms we need to evaluate is small. Note that all the truncations described above can be determined according to a chosen error tolerance, say, 10^{-8}, and the precision can be systematically improved by including higher order terms.

What remains to be done is to evaluate Eq. (3.87) for up to L cosine functions. For a given L, an analytical expression for the integral is possible, but it can become more and more complex as L increases and it can be difficult for coding. Therefore we split each cosine function into two exponential functions using $\cos x = (e^{ix} + e^{-ix})/2$. In this way, Eq. (3.87) turns into 2^L integrals of exponential functions, whose analytical expressions are easy to get.

This is easy to program using depth-first search. Since the truncation L is typically small and we do not need to do the splitting for the l-th term if $n_l = 0$, this method gives a good balance between the cost of programming time and that of the running time.

Two-Qubit Rotation Angle

For the two-qubit rotation angle Θ_{ij}, we want to derive an analytical expression for

$$\int dt_1 \int dt_2 \sum_{n,m=-\infty}^{+\infty} \boldsymbol{C}^{(k)}_{2n,i\rho} e^{in\omega_{\rm rf}t_1} \boldsymbol{C}^{(k)}_{2m,j\sigma} e^{-im\omega_{\rm rf}t_2} \sin\left(\mu t_1 + \sum_{l_1=0}^{\infty} \varphi_i^{(l_1)} \cos l_1\omega_{\rm rf}t_1\right) \times \sin\left(\mu t_2 + \sum_{l_2=0}^{\infty} \varphi_j^{(l_2)} \cos l_2\omega_{\rm rf}t_2\right) e^{i\omega_k(t_1-t_2)} \tag{3.88}$$

for one term in Eq. (3.68) and the other term can be gotten by an exchange of i and j.

Recall that to get the $\boldsymbol{\gamma}$ matrix in Eq. (2.55), we need two types of integral limits:

$$\int_{(p-1)\tau/n_{\rm seg}}^{p\tau/n_{\rm seg}} dt_1 \int_{(q-1)\tau/n_{\rm seg}}^{q\tau/n_{\rm seg}} dt_2 \qquad \text{and} \qquad \int_{(p-1)\tau/n_{\rm seg}}^{p\tau/n_{\rm seg}} dt_1 \int_{(p-1)\tau/n_{\rm seg}}^{t_1} dt_2. \tag{3.89}$$

For the first type, the integrations over t_1 and t_2 are separable and are exactly what we have solved for α_j^k above. Therefore we only need to consider the second type.

Following the previous steps for α_j^k, let us define new variables $\omega_1 = \omega_k + n\omega_{\rm rf}$ and $\omega_2 = \omega_k + m\omega_{\rm rf}$, split the sine function into two exponential functions, and expand $\exp(\pm i\varphi_j^{(l)} \cos l\omega_{\rm rf}t)$ using Eq. (3.84). What remains to be solved is

$$\int dt_1 \int dt_2 e^{\pm i(\mu t_1 + \varphi_i^{(0)})} e^{\pm i(\mu t_2 + \varphi_j^{(0)})} e^{i\omega_1 t_1} e^{-i\omega_2 t_2} \prod_{l_1=1}^{L_1} \cos n_{l_1}\omega_{\rm rf}t_1 \prod_{l_2=1}^{L_2} \cos m_{l_2}\omega_{\rm rf}t_2. \tag{3.90}$$

Again we truncate at large values of L_1, L_2 and n_{l_1}, m_{l_2} in the expansions and express the cosine functions as two exponential functions, then analytical formulae for these integrals are easy to derive. One thing to note is that when $e^{\pm i(\mu t_1+\varphi_i^{(0)})}$ and $e^{\pm i(\mu t_2+\varphi_j^{(0)})}$ take opposite signs, the result we get may have an $\omega_1-\omega_2$ in the denominator, thus the expression becomes undefined in the special case $\omega_1=\omega_2$. Actually there is no problem here because in this case the numerator will also be 0. What we need to do is to rewrite the expression in the form of a sinc function to avoid numerical problems in coding.

Numerical Results

As a simple example, we consider an entangling gate for two ions in the 100-ion crystal shown in Fig. 3.1(a) and make a similar plot as Fig. 2.4 by scanning the detuning of the laser. To be specific, we consider 100 $^{171}\mathrm{Yb}^+$ ions in a trap with trapping parameters $\boldsymbol{a} = (-0.015,\ -0.015,\ 0.03)$ and $\boldsymbol{q} = (0.3,\ -0.3,\ 0)$, and an RF frequency $\omega_{\mathrm{rf}} = 2\pi\times 50\,\mathrm{MHz}$. The two ions we consider are indicated in red in Fig. 3.22, which shows the equilibrium trajectories of the ions. Counter-propagating laser beams with a wavelength around $\lambda = 355\,\mathrm{nm}$ are applied in the x direction to form a phase-insensitive geometry (see Chapter 2), and the ions are cooled to the Dopper temperature $k_BT = \hbar\Gamma/2$ with the spontaneous emission rate $\Gamma = 2\pi\times 20\,\mathrm{MHz}$ for $^{171}\mathrm{Yb}^+$ ions. Suppose we use $n_{\mathrm{seg}} = 15$ segments for a total gate time $\tau = 300\,\mu\mathrm{s}$. The optimal gate infidelity is shown in Fig. 3.23 as we scan the laser detuning μ. This is only a rough scan and we have not optimized the choice of n_{seg} and τ; but as we can see, high gate fidelity of 99.9% is still possible when we consider the micromotion. In Fig. 3.23(b) we show a comparison for different truncations of the micromotion. The computation for an expansion to higher order (truncated at $L = 5$ for the equilibrium trajectories and $n_{\mathrm{cut}} = 5$ for the high-frequency modulation of the normal modes) is about

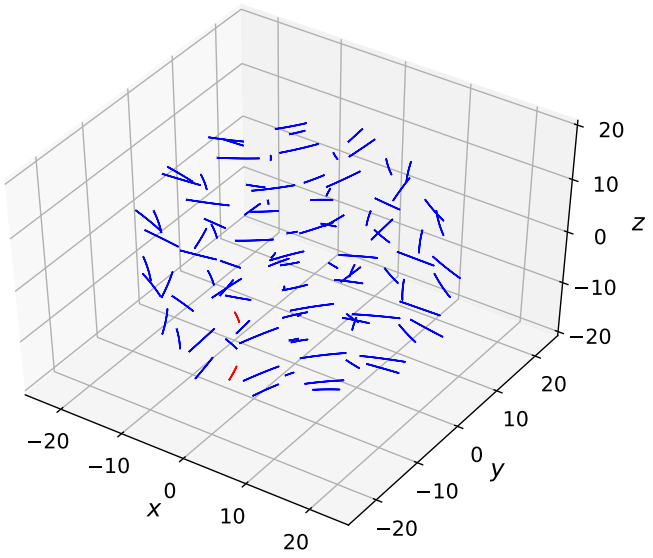

Figure 3.22: Equilibrium trajectories of the ions in the trap. The two ions on which we apply the entangling gate are colored in red.

50 times slower than the lower order one ($L = 1$ and $n_{\text{cut}} = 1$); but clearly this time cost is worth it because the gate infidelity can differ by one order of magnitude. We expect the difference to be more significant for ions with larger micromotion amplitudes.

Note that for this example the micromotion along the z direction is much smaller than in other directions, so we could have gotten much faster convergence had we applied the laser beams in the z direction; but here we just want large micromotion to demonstrate the idea. Also note that the timing of the algorithm scales linearly with the number of ions (number of normal modes) and linearly with the number of segments (because the most time-consuming part of the algorithm is the $p = q$ double integral of the two-qubit rotation angle); and the scan of the gate parameters can be performed in parallel. Therefore even though the design of the gate with micromotion is much slower than that without micromotion, we can still expect it to work for hundreds of ions and hundreds of pulse segments.

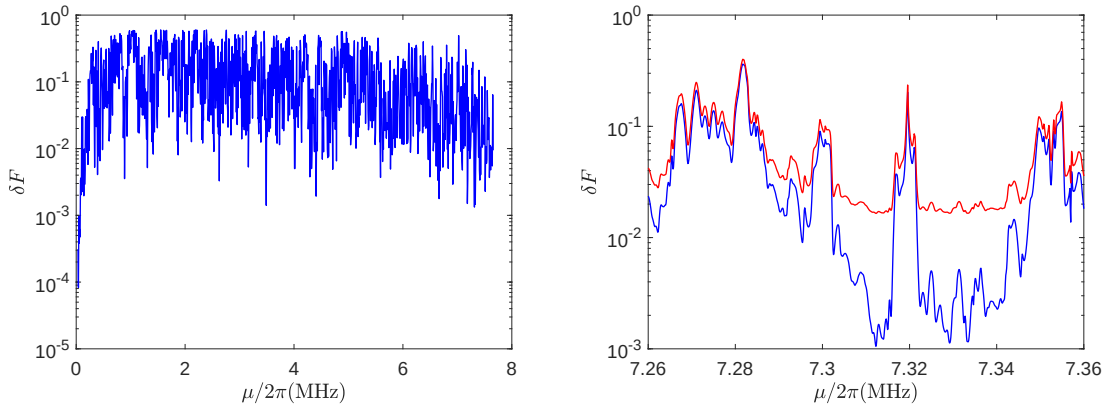

(a) (b)

Figure 3.23: (a) Optimal gate infidelity δF for a scan of the laser detuning μ over the whole spectrum of the normal modes of the crystal. Note that the resolution of this plot is not enough to show all the structures of the curve. (b) A zoomed-in scan for a small range of frequencies at the high-frequency end. (We avoid the use of the low-frequency end, which may be sensitive to the soft modes, even though it seems to have higher fidelity.) The blue curve is optimized for ions' motions truncated at $L = 5$ for the equilibrium trajectories and at $n_{\text{cut}} = 5$ for the high-frequency modulation of the normal modes. The red curve is what we would have gotten using the same optimized laser sequence if we truncated at $L = 1$ and $n_{\text{cut}} = 1$.

Chapter 4

Simple Application in Medium-Sized Ion Crystal

Having seen how the basic quantum operations can be realized in a general ion crystal, let us consider a simple application in a medium-sized crystal with tens of ions: the quantum simulation of Ising model with arbitrary all-to-all coupling. First we will review the previous work on analogue simulation of the Ising model with arbitrary coupling. After showing some disadvantages of this scheme, we then move on to a proposal using digital simulation. Many of the formulas and techniques used here are directly generalized from the previous chapters.

4.1 Quantum Simulation of Ising Model in Ion Trap

4.1.1 Ising Model

An Ising model is described by the Hamiltonian

$$H = \sum_i h_i \sigma_i^x + \sum_{i,j} J_{ij} \sigma_i^x \sigma_j^x. \tag{4.1}$$

Its classical version ($\sigma_i^x = \pm 1$) was invented by Wilhelm Lenz in 1920 to study magnetism and was first solved in 1D by Ernst Ising in 1924 [92]. In two or higher dimensions, the Ising model shows an order-disorder phase transition as the temperature changes, which has been widely studied both analytically [93, 94] and numerically [95–97].

Its quantum counterpart, the quantum Ising model, is also one of the simplest spin models that show non-trivial properties of quantum magnetism such as phase transition [98] and spin glass phase [99]. Thus it is considered as one of the best candidates to demonstrate the idea of quantum simulation [100]. Several experiments have been conducted for small to medium-sized systems [28, 101–104] using trapped ions, which provide strong flexibility in the coupling strength between the spins.

4.1.2 Analogue Simulation

Here we briefly review the scheme of Ref. [105], where an Ising model with arbitrary all-to-all coupling is simulated by the effective Hamiltonian of the system.

To start with, we go back to the laser beam scheme in Chapter 2 with the unitary time evolution described by Eq. (2.23). For fast two-qubit entangling gates, we apply strong laser driving on the two ions with small detuning to the phonon modes, which can lead to strong entanglement between the qubit states and the phonon states; then we optimize the gate parameters such that at certain gate time τ, the two-qubit phase Θ_{ij} is at the desired value of $\pm\pi/4$ while the residual entanglement to the phonon modes is minimized.

This time, let us consider weak laser beams on all the ions at the same time, with large detuning such that all the phonon modes are only weakly excited. In this limit the ϕ_j and ψ_j terms in Eq. (2.23) can be regarded as small perturbations, while Θ_{ij} is governed by a

linear term in the evolution time, i.e. the evolution under a constant Hamiltonian. More rigorously, we assume $\Omega_j \ll \mu$, $\eta_k b_j^k \Omega_j \ll |\mu - \omega_k|$, then the unitary evolution is effectively governed by a time-independent Hamiltonian [101]

$$H_{\text{eff}} = \sum_{i<j} J_{ij} \sigma_i^x \sigma_j^x, \tag{4.2}$$

where

$$J_{ij} = \Omega_i \Omega_j \sum_{k=1}^{N} \frac{\eta_k^2 b_i^k b_j^k \omega_k}{\mu^2 - \omega_k^2}. \tag{4.3}$$

This interaction is usually fitted by a power law: $J_{ij} \approx J_0/|i-j|^\alpha$ with $0 < \alpha < 3$ for a 1D chain [104]. The additional terms in Eq. (2.23) act as small fluctuations around $\exp(-iH_{\text{eff}}t)$ at the order of $O(\eta_k b_j^k \Omega_j/|\mu - \omega_k|)$, which does not increase with the evolution time. Besides, there is a carrier term, which we compensated by single-qubit gates when designing entangling gates, at the order of $O(\Omega_j/\mu)$.

If we apply laser beams with multiple frequency components (because for all-to-all coupling there are $N(N-1)/2$ independent parameters, it should suffice to use N frequencies with adjustable intensity on each of the N ions), the coupling strength is given by [105]

$$J_{ij} = \sum_{n=1}^{N} \Omega_{i,n} \Omega_{j,n} \sum_{k=1}^{N} \frac{\eta_k^2 b_i^k b_j^k \omega_k}{\mu_n^2 - \omega_k^2} \equiv \sum_{n=1}^{N} \Omega_{i,n} \Omega_{j,n} F_{i,j,n} \tag{4.4}$$

where $\Omega_{i,n}$ describes the intensity of the laser beam whose detuning is μ_n on the ion i. By solving these $N(N-1)/2$ equations for $\{\Omega_{i,n}\}$ we get the required laser beams to simulate this Ising model.

Let us now estimate the influence of the leading order error terms on the quantum simulation. Usually in this type of experiments, we prepare an initial state, apply the Hamiltonian

for certain time and then make measurements of the final states [100]. Ideally we want a unitary evolution $\exp(-iH_{\text{eff}}t)$, while the error terms will change the probability distribution of measuring the final states. This can be characterized by the fidelity between the ideal and the real final states, which can be computed in the same way as Chapter 2: we have an infidelity of $\sum_{jk}(n_k+1/2)|\eta_k b_j^k \Omega_j/(\mu-\omega_k)|^2$ from the entanglement to the phonon modes, assuming a phonon number of n_k in the k-th mode, and an additional infidelity of $\sum_j |\Omega_j/\mu|^2$ from the carrier terms.

However, in many cases we do not want to simulate a constant Hamiltonian, but vary the parameters adiabatically. This is used, for example, to find the ground state of a final Hamiltonian, from an initial Hamiltonian whose ground state is easy to compute and to prepare. In this situation, the errors are more difficult to bound even if the adiabatic condition is satisfied. The reason is that, for adiabatic evolution, we do not care about the intermediate Hamiltonian so long as the change is slow compared with the gap of the Hamiltonian; but to evaluate the errors in the unitary evolution, we must know the detailed form of parameters such as $\Omega_{i,n}(t)$ and $\mu_n(t)$ so that we can integrate the whole process, and usually we cannot get an analytical result.

Another disadvantage of this scheme is that the coupling strength between different ions is low, thus it will be sensitive to other noise and errors in the experiment. Suppose we can tolerate an error of ϵ, and we assume ground-state cooling for all the phonon modes to minimize the error. Here we consider two limits: (1) if the laser beams are detuned close to a single motional sideband, say, mode k, our estimation of infidelity requires that $|\eta_k b_j^k \Omega_j/(\mu-\omega_k)|^2 \lesssim \epsilon$. Then the coupling between ions i and j is of the order $J_{ij} \lesssim \epsilon\omega_k(\mu-\omega_k)/(\mu+\omega_k) \sim \epsilon|\mu-\omega_k|$. To neglect the effect of all the other phonon modes, $|\mu-\omega_k|$ needs to be much smaller than the detuning to the other modes. For a 1D or

2D ion crystal which is used for this type of experiments, the spectrum of the transverse modes is typically already very small, and to be far detuned to all the other $(N-1)$ modes we need a further factor of $1/N$. Actually, Ref. [105] estimates the coupling strength for nearest neighbor ion pairs to be 10-10^2 Hz for a chain of tens of ions. (2) In the other limit, we assume $|\mu - \omega_k|$ is large for all the modes. Then we can replace ω_k by their average $\bar{\omega}$ because the spectral is narrow. However, note that in Eq. (4.3) we have the summation of $b_i^k b_j^k$ over k, which vanishes due to the orthogonality of the normal modes. Therefore for the leading order term we must expand ω_k around $\bar{\omega}$ to the first order. Actually, the ω_k in the numerator of Eq. (4.3) cancels that in the η_k^2, thus the only k-dependent part is the $\mu^2 - \omega_k^2$ term in the denominator. We can bound the coupling as

$$\begin{aligned}
J_{ij} \sim & \Omega_i \Omega_j \sum_k \frac{b_i^k b_j^k \bar{\eta}^2 \bar{\omega}}{(\mu^2 - \bar{\omega}^2)^2} 2\bar{\omega}\delta\omega_k \\
\leq & \sum_k \frac{|\bar{\eta}^2 b_i^k b_j^k \Omega_i \Omega_j|}{(\mu - \bar{\omega})^2} \frac{2\bar{\omega}^2 |\delta\omega_k|}{(\mu + \bar{\omega})^2} \\
\leq & \sum_k \frac{|\bar{\eta}^2 b_i^k b_j^k \Omega_i \Omega_j|}{(\mu - \bar{\omega})^2} \frac{2\bar{\omega}^2 \delta}{(\mu + \bar{\omega})^2} \\
\leq & \sqrt{\sum_k \left(\frac{\bar{\eta} b_i^k \Omega_i}{\mu - \bar{\omega}} \right)^2} \sqrt{\sum_k \left(\frac{\bar{\eta} b_j^k \Omega_j}{\mu - \bar{\omega}} \right)^2} \frac{2\bar{\omega}^2 \delta}{(\mu + \bar{\omega})^2} \\
\lesssim & \epsilon \frac{2\bar{\omega}^2 \delta}{(\mu + \bar{\omega})^2}
\end{aligned} \tag{4.5}$$

with $\delta\omega_k \equiv \omega_k - \bar{\omega}$ and δ defined as the whole range of the spectrum. In the above derivation from the third to the fourth line we have applied the Cauchy-Schwarz inequality. Again we see that the coupling is bounded by the error tolerance times the range of the spectrum, which is small for typical experiments. For example, if we consider a trap with transverse trapping frequency of several MHz and a phonon mode spectrum of about 1% the width

(see the example we considered in Chapter 2), and if we want the error to be less than 1%, the largest coupling strength we can get is only of the order 10^2 Hz. Furthermore, in this regime we approach the $J_{ij} \sim 1/|i-j|^3$ scaling and thus are not able to arbitrarily control the coupling strength.

4.1.3 Digital Simulation

Another way to approximately simulate the Hamiltonian is to apply quantum gates that correspond to the unitary evolution of the system at a series of discrete time points, a.k.a. digital quantum simulation [100].

This method is very similar to the design of an entangling gate between two ions. The basic idea is still to minimize the residual entanglement to the phonon modes α_j^k [Eq. (2.25)] while setting $\Theta_{ij} = J_{ij}\delta t$ at small gate time δt for all the ion pairs [Eq. (2.28)]. Then by repeatedly applying this quantum gate we simulate the evolution under the Hamiltonian $\sum_{i<j} J_{ij}\sigma_i^x\sigma_j^x$. To realize arbitrary coupling among N ions, which corresponds to $O(N^2)$ degrees of freedom, we can apply $O(N)$ segmented pulses to the N ions. Note that if we have a lower bound on the length of each segment, here the total gate time will scale as $O(N)$. In comparison, if we apply the entangling gates between any two ions one after another, the timing will be $O(N^2)$. (We can use the method of Sec. 3.2 to parallelize some gates, but here we want arbitrary coupling between the ions and thus the distance between an ion pair on which we appliy the gate can be as large as N. Then the scheme of Sec. 3.2 does not work.) It is difficult to completely suppress the residual coupling to the phonon modes, so instead we consider the following optimization problem, which is a natural generalization of what we

have solved for the gate design in Sec. 2.1.3:

$$\begin{aligned} \min_{\{\boldsymbol{\Omega}_i\}} \quad & \sum_{i=1}^{N} \boldsymbol{\Omega}_i^T \left[\sum_k \boldsymbol{A}_i^{k\dagger} \boldsymbol{A}_i^k \coth \frac{\hbar\omega_k}{2k_BT} \right] \boldsymbol{\Omega}_i \\ \text{s.t.} \quad & \boldsymbol{\Omega}_i^T \boldsymbol{\gamma}^{(i,j)} \boldsymbol{\Omega}_j = J_{ij} \cdot \delta t \qquad (i<j) \end{aligned} \tag{4.6}$$

where $\boldsymbol{\Omega}_i$ is a column vector for the pulse sequence on ion i, and $\boldsymbol{J}$ is a real symmetric matrix describing the Ising coupling between the ions. $\boldsymbol{A}_i^k$ (row vector) and $\boldsymbol{\gamma}^{(i,j)}$ (matrix) are defined in Eq. (2.51) and Eq. (2.52) (after symmetrization). Note that the original Eq. (2.52) is derived for same laser sequence on both ions, and here we need a small modification for different $\boldsymbol{\Omega}_i$ and $\boldsymbol{\Omega}_j$, which corresponds to the symmetrization of the $\boldsymbol{\gamma}^{(i,j)}$ matrix.

This problem of quadratic optimization with quadratic equality constraints is in general NP-hard, but for small to medium-sized system it is still possible to find good numerical solutions, and in most cases we do not need to find the global minimum, but only some "good enough" solutions with infidelity below certain error tolerance. The similar technique has recently also been used to design parallel gates [106]. Note that different from what we considered in Sec. 3.2, this scheme is difficult to generalize to large crystals due to the difficulty in solving the parameters.

As an example, let us consider a linear chain of N ions with a uniform spacing of $d = 8\,\mu\text{m}$. Similar to Sec. 2.2 we assume a transverse trapping frequency $\omega_x = 2\pi \times 3\,\text{MHz}$, a temperature of $k_BT = \hbar\omega_x$ and Lamb-Dicke parameters $\eta_k \approx 0.11$. Numerically we find that $n_{\text{seg}} = 2N$ segments and gate time $\tau = 35N\,\mu\text{s}$ seem to work well for randomly generated $\boldsymbol{J}\delta t$ matrices whose entries are sampled uniformly from $[-1, 1]$, with an error around or less than 0.2% per ion. Note that both the achieved phase $J\delta t$ and the error from residual phonon excitation scale as $|\boldsymbol{\Omega}|^2$, so a simple rescaling of the laser intensity will not reduce

the gate error because then we need to repeat the gate for more times to reach a targeted two-qubit phase.

In Fig. 4.1 we show the time it takes for MATLAB to solve this optimization problem with different system sizes $N = 10, 15, 20, 25, 30$. It seems to follow a power law $t \propto N^6$. This suggests that first designing the laser sequence on a classical computer and then performing the quantum simulation on the ion trap system should be faster than a direct classical simulation of the Ising model for large N, which requires an exponential scaling. However, note that for larger systems it becomes difficult for MATLAB to find a solution to the quadratic constraints in Eq. (4.6), which is required to start the optimization process; so the N^6 scaling may not work for larger N.

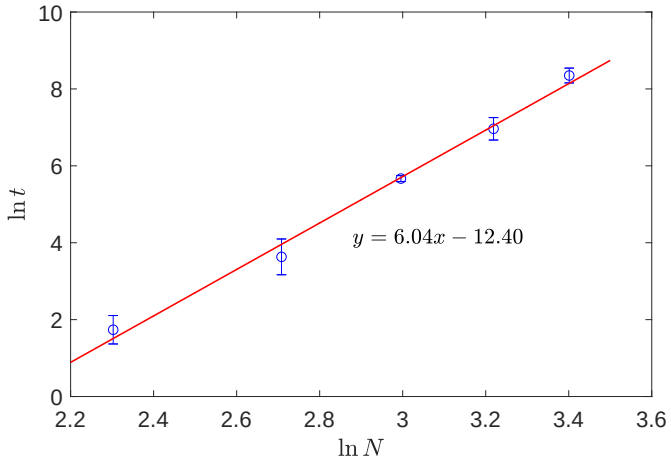

Figure 4.1: Log-log plot for the time t to find a local minimum of Eq. (4.6) vs. the system size N. For each N we randomly generate five $\boldsymbol{J}$ matrices, whose entries are uniformly sampled between $[-1, 1]$, to estimate the average timing and the error bar.

Unfortunately, the effective coupling strength here goes down as $1/N$ because the gate time τ we use is proportional to N. Because the analogue simulation in Sec. 4.1.2 also has a similar problem, it seems this scaling is inevitable if we want arbitrary all-to-all coupling between

the ions. Nevertheless, the digital method should be less vulnerable to errors compared with the analogue simulation because the carrier term and the coupling to the phonon modes are already suppressed in the gate design.

After finding a good solution with small errors, we can use it to simulate an Ising model with arbitrary connectivity by rescaling the laser intensity to match different evolution time, or by repeatedly applying the gates. As is mentioned in the previous subsection, we may also want to vary the Hamiltonian adiabatically. For example we may want to simulate the following Hamiltonian

$$H(t) = \alpha(t) \left(\sum_i h_i \sigma_i^x + \sum_{i<j} J_{ij} \sigma_i^x \sigma_j^x \right) + \beta(t) h_0 \sum_i \sigma_i^z, \tag{4.7}$$

with $\alpha(0) = 0$, $\alpha(T) = 1$, $\beta(0) = 1$, $\beta(T) = 0$ where T is the total evolution time. At $t = 0$ the ions can be prepared in $|\psi_0\rangle = |00\cdots0\rangle$, the ground state of $H(0)$ ($h_0 < 0$). Then if $\alpha(t)$ and $\beta(t)$ changes slowly enough, the system will adiabatically go to the ground state of $H(T)$ after the evolution. To demonstrate the idea of digital simulation, we simply assume $\alpha(t)$ and $\beta(t)$ are linear in time. Let us first consider a simple way of discretization using piecewise-constant $\alpha(t)$ and $\beta(t)$ with M steps

$$\alpha_m = \frac{m}{M}, \qquad \beta_m = 1 - \frac{m}{M} \qquad\qquad (m = 1,\, 2,\, \cdots,\, M), \tag{4.8}$$

and apply a series of gates to the system (see e.g. [100])

$$|\psi_m\rangle = e^{-i\beta_m H_z \delta t} e^{-i\alpha_m H_x \delta t} |\psi_{m-1}\rangle \tag{4.9}$$

where $\delta t = T/M$, $H_x = \sum_i h_i \sigma_i^x + \sum_{i<j} J_{ij} \sigma_i^x \sigma_j^x$ and $H_z = h_0 \sum_i \sigma_i^z$. In the limit of large M,

we expect the discretization error on the final state to be $O(1/M)$, hence $O(1/M^2)$ on the fidelity. Note that at each step the two single-qubit rotation terms can be combined into a single rotation for further simplification.

However, this is not the best way for discretization. Without adding more gates, we can apply second order Trotter expansion [4, 107, 108] to reduce the discretization error:

$$\begin{aligned} U(0,T) =& e^{-iH(t_M)\delta t/2}\left[\prod_{j=1}^{M-1} e^{-iH(t_j)\delta t}\right] e^{-iH(t_0)\delta t/2} + O(\delta t^2) \\ =& e^{-iH_x\delta t/2}\left[\prod_{j=1}^{M-1} e^{-i\beta_j H_z\delta t/2} e^{-i\alpha_j H_x\delta t} e^{-i\beta_j H_z\delta t/2}\right] e^{-iH_z\delta t/2} + O(\delta t^2) \\ =& e^{-iH_x\delta t/2}\left[\prod_{j=1}^{M-1} e^{-i\beta_{j+1/2} H_z\delta t} e^{-i\alpha_j H_x\delta t}\right] e^{-i\beta_{1/2} H_z\delta t} + O(\delta t^2) \end{aligned} \tag{4.10}$$

where we have used the linearity of $\alpha(t)$ and $\beta(t)$ to combine terms, and $\prod$ means multiplying the operators one by one on the left. The first evolution under H_z can be removed because the initial state is an eigenstate. Now the error on the final state is $O(1/M^2)$ and then the infidelity is $O(1/M^4)$. Even higher order Trotter expansions can also be applied to further reduce the discretization error or the required number of steps for a given error tolerance.

Chapter 5

Outlook

Based on what we have seen in this thesis, there seems to be no fundamental limit in conducting quantum computing directly on a large ion crystal. We discuss how high-fidelity entangling gates can be designed in a small ion crystal in Chapter 2. Then in Chapter 3, we show that large ion crystals can still be stable in the RF trap and the motions of the ions can be accurately computed, thus allowing for high-fidelity gate design. Next we show that the crosstalk of the driving on different ions decays cubically with their distance. Therefore, when designing entangling gates for nearby ions in a large crystal, we can ignore all the ions far away and effectively work with a small to medium-sized ion crystal, where the previous scheme can work. Furthermore, these entangling gates can be applied in parallel, which may greatly reduce the circuit depth.

However, many technical problems do exist and may require huge amount of efforts to solve. In Chapter 2 we see that sophisticated control in laser intensity and detuning is needed to improve the gate fidelity; in Chapter 3 the micromotion and soft normal modes arise and require more advanced methods for individual ion addressing. Moreover, even though the effect of micromotion can be included into the gate design using the theoretically computed

phonon modes in the crystal with the corresponding micromotion patterns, what we have not discussed is how sensitive these modes are to the experimental noise and imperfections. How much will the crystal structure and the normal modes change if the RF voltage undergoes, say, 1% variation? Is the gate design robust against these types of fluctuation? Can we calibrate the phonon modes and micromotions in experiments? These may be the topics for future studies.

Finally we briefly mention one possible direction to solve the problem of micromotion. As is mentioned in Chapter 3, the existence of micromotion will increase the time cost in designing the high-fidelity gate (although still within reach), and the large micromotion of the ions in their equilibrium configuration may cause difficulty in focusing the laser beams on them. Now if we use a pulsed laser with a repetition rate equal to the RF frequency, then the ion will be at the same position every time a pulse arrives. In this sense, the micromotion will have no effect on the gate apart from a constant Doppler shift due to the velocity of the ion at the time of the pulse. Currently pulsed laser is already utilized in the experiment of ion trap quantum computing to generate a frequency comb and produce the desired detuning for the Raman transition [29,30]. If the repetition rate of the laser can be synchronized with the RF field, we would expect a great simplification in the design and the implementing of entangling gates in a large ion crystal.

BIBLIOGRAPHY

Bibliography

[1] Y. Wu, S.-T. Wang, and L.-M. Duan, "Noise analysis for high-fidelity quantum entangling gates in an anharmonic linear Paul trap," *Phys. Rev. A*, vol. 97, p. 062325, Jun 2018.

[2] C. J. Trout, M. Li, M. Gutiérrez, Y. Wu, S.-T. Wang, L. Duan, and K. R. Brown, "Simulating the performance of a distance-3 surface code in a linear ion trap," *New Journal of Physics*, vol. 20, no. 4, p. 043038, 2018.

[3] D. P. DiVincenzo, "The physical implementation of quantum computation," *Fortschritte der Physik: Progress of Physics*, vol. 48, no. 9-11, pp. 771–783, 2000.

[4] M. Nielsen and I. Chuang, *Quantum Computation and Quantum Information*. Cambridge University Press, 2000.

[5] A. G. Fowler, M. Mariantoni, J. M. Martinis, and A. N. Cleland, "Surface codes: Towards practical large-scale quantum computation," *Phys. Rev. A*, vol. 86, p. 032324, Sep 2012.

[6] J. I. Cirac and P. Zoller, "Quantum computations with cold trapped ions," *Phys. Rev. Lett.*, vol. 74, pp. 4091–4094, May 1995.

[7] D. J. Wineland, M. Barrett, J. Britton, J. Chiaverini, B. DeMarco, W. M. Itano, B. Jelenković, C. Langer, D. Leibfried, V. Meyer, T. Rosenband, and T. Schätz, "Quantum information processing with trapped ions," *Philosophical Transactions of the Royal Society of London A: Mathematical, Physical and Engineering Sciences*, vol. 361, no. 1808, pp. 1349–1361, 2003.

[8] J. Clarke and F. K. Wilhelm, "Superconducting quantum bits," *Nature*, vol. 453, p. 1031, Jun 2008.

[9] J. Wrachtrup, S. Y. Kilin, and A. P. Nizovtsev, "Quantum computation using the ^{13}C nuclear spins near the single NV defect center in diamond," *Optics and Spectroscopy*, vol. 91, pp. 429–437, Sep 2001.

[10] D. Loss and D. P. DiVincenzo, "Quantum computation with quantum dots," *Phys. Rev. A*, vol. 57, pp. 120–126, Jan 1998.

[11] J. K. Pachos, *Introduction to topological quantum computation*. Cambridge University Press, 2012.

[12] I. Bengtsson and K. Zyczkowski, *Geometry of Quantum States: An Introduction to Quantum Entanglement*. Cambridge University Press, 2006.

[13] M. A. Nielsen, "A simple formula for the average gate fidelity of a quantum dynamical operation," *Physics Letters A*, vol. 303, no. 4, pp. 249 – 252, 2002.

[14] R. Kueng, D. M. Long, A. C. Doherty, and S. T. Flammia, "Comparing experiments to the fault-tolerance threshold," *Phys. Rev. Lett.*, vol. 117, p. 170502, Oct 2016.

[15] A. Y. Kitaev, "Quantum computations: algorithms and error correction," *Russian Mathematical Surveys*, vol. 52, no. 6, p. 1191, 1997.

[16] J. Watrous, "Semidefinite programs for completely bounded norms," *Theory of Computing*, vol. 5, pp. 217–238, 2009.

[17] W. Paul, "Electromagnetic traps for charged and neutral particles," *Rev. Mod. Phys.*, vol. 62, pp. 531–540, Jul 1990.

[18] L. S. Brown and G. Gabrielse, "Geonium theory: Physics of a single electron or ion in a Penning trap," *Rev. Mod. Phys.*, vol. 58, pp. 233–311, Jan 1986.

[19] J. D. Jackson, *Classical electrodynamics*. Wiley, 3rd ed., 1999.

[20] D. Leibfried, R. Blatt, C. Monroe, and D. Wineland, "Quantum dynamics of single trapped ions," *Rev. Mod. Phys.*, vol. 75, pp. 281–324, Mar 2003.

[21] N. McLachlan, *Theory and application of Mathieu functions*. Clarendon Press, 1947.

[22] H. Dehmelt, "Radiofrequency spectroscopy of stored ions i: Storage," vol. 3 of *Advances in Atomic and Molecular Physics*, pp. 53 – 72, Academic Press, 1968.

[23] J. Nocedal and S. J. Wright, *Numerical optimization*. New York : Springer, 1999.

[24] C. J. Foot, *Atomic physics*. Oxford University Press, 2005.

[25] J. I. Cirac, L. J. Garay, R. Blatt, A. S. Parkins, and P. Zoller, "Laser cooling of trapped ions: The influence of micromotion," *Phys. Rev. A*, vol. 49, pp. 421–432, Jan 1994.

[26] R. Blümel, C. Kappler, W. Quint, and H. Walther, "Chaos and order of laser-cooled ions in a paul trap," *Phys. Rev. A*, vol. 40, pp. 808–823, Jul 1989.

[27] X. Zhang, *Quantum Computation and Simulation with Trapped Ions*. PhD thesis, Tsinghua University, Beijing, China, 2016.

[28] J. Zhang, G. Pagano, P. W. Hess, A. Kyprianidis, P. Becker, H. Kaplan, A. V. Gorshkov, Z.-X. Gong, and C. Monroe, "Observation of a many-body dynamical phase transition with a 53-qubit quantum simulator," *Nature*, vol. 551, p. 601, 2017.

[29] D. Hayes, D. N. Matsukevich, P. Maunz, D. Hucul, Q. Quraishi, S. Olmschenk, W. Campbell, J. Mizrahi, C. Senko, and C. Monroe, "Entanglement of atomic qubits using an optical frequency comb," *Phys. Rev. Lett.*, vol. 104, p. 140501, Apr 2010.

[30] S. Debnath, *A Programmable Five Qubit Quantum Computer Using Trapped Atomic Ions*. PhD thesis, University of Maryland, College Park, 2016.

[31] C. J. Ballance, T. P. Harty, N. M. Linke, M. A. Sepiol, and D. M. Lucas, "High-fidelity quantum logic gates using trapped-ion hyperfine qubits," *Phys. Rev. Lett.*, vol. 117, p. 060504, Aug 2016.

[32] J. P. Gaebler, T. R. Tan, Y. Lin, Y. Wan, R. Bowler, A. C. Keith, S. Glancy, K. Coakley, E. Knill, D. Leibfried, and D. J. Wineland, "High-fidelity universal gate set for $^{9}Be^{+}$ ion qubits," *Phys. Rev. Lett.*, vol. 117, p. 060505, Aug 2016.

[33] J. J. Sakurai and J. Napolitano, *Modern quantum mechanics*. Addison-Wesley, 2nd ed., 2011.

[34] N. Goldman and J. Dalibard, "Periodically driven quantum systems: Effective hamiltonians and engineered gauge fields," *Phys. Rev. X*, vol. 4, p. 031027, Aug 2014.

[35] A. Sørensen and K. Mølmer, "Quantum computation with ions in thermal motion," *Phys. Rev. Lett.*, vol. 82, pp. 1971–1974, Mar 1999.

[36] R. Blatt and D. Wineland, "Entangled states of trapped atomic ions," *Nature*, vol. 453, pp. 1008–1015, 2008.

[37] D. Kielpinski, C. Monroe, and D. J. Wineland, "Architecture for a large-scale ion-trap quantum computer," *Nature*, vol. 417, pp. 709–711, 2002.

[38] W. K. Hensinger, S. Olmschenk, D. Stick, D. Hucul, M. Yeo, M. Acton, L. Deslauriers, C. Monroe, and J. Rabchuk, "T-junction ion trap array for two-dimensional ion shuttling, storage, and manipulation," *Applied Physics Letters*, vol. 88, no. 3, p. 034101, 2006.

[39] C. Monroe and J. Kim, "Scaling the ion trap quantum processor," *Science*, vol. 339, no. 6124, pp. 1164–1169, 2013.

[40] Shi-Liang Zhu, C. Monroe, and L.-M. Duan, "Arbitrary-speed quantum gates within large ion crystals through minimum control of laser beams," *Europhys. Lett.*, vol. 73, no. 4, pp. 485–491, 2006.

[41] S.-T. Wang, C. Shen, and L.-M. Duan, "Quantum computation under micromotion in a planar ion crystal," *Scientific reports*, vol. 5, no. 8555, 2015.

[42] G.-D. Lin, S.-L. Zhu, R. Islam, K. Kim, M.-S. Chang, S. Korenblit, C. Monroe, and L.-M. Duan, "Large-scale quantum computation in an anharmonic linear ion trap," *Europhysics Letters*, vol. 86, no. 6, p. 60004, 2009.

[43] W. C. Campbell, J. Mizrahi, Q. Quraishi, C. Senko, D. Hayes, D. Hucul, D. N. Matsukevich, P. Maunz, and C. Monroe, "Ultrafast gates for single atomic qubits," *Phys. Rev. Lett.*, vol. 105, p. 090502, Aug 2010.

[44] P. J. Lee, K.-A. Brickman, L. Deslauriers, P. C. Haljan, L.-M. Duan, and C. Monroe, "Phase control of trapped ion quantum gates," *Journal of Optics B: Quantum and Semiclassical Optics*, vol. 7, no. 10, p. S371, 2005.

[45] W. Magnus, "On the exponential solution of differential equations for a linear operator," *Communications on Pure and Applied Mathematics*, vol. 7, no. 4, pp. 649–673, 1954.

[46] T. J. Green and M. J. Biercuk, "Phase-modulated decoupling and error suppression in qubit-oscillator systems," *Phys. Rev. Lett.*, vol. 114, p. 120502, Mar 2015.

[47] P. H. Leung and K. R. Brown, "Entangling an arbitrary pair of qubits in a long ion crystal," *Phys. Rev. A*, vol. 98, p. 032318, Sep 2018.

[48] G.-D. Lin, *Quantum simulation with ultracold atoms and trapped ions.* PhD thesis, University of Michigan, Ann Arbor, 2010.

[49] Y. Tomita and K. M. Svore, "Low-distance surface codes under realistic quantum noise," *Phys. Rev. A*, vol. 90, p. 062320, Dec 2014.

[50] C. J. Ballance, *High-fidelity quantum logic in* Ca^+. Springer, 2017.

[51] H. Landa, M. Drewsen, B. Reznik, and A. Retzker, "Modes of oscillation in radiofrequency Paul traps," *New Journal of Physics*, vol. 14, no. 9, p. 093023, 2012.

[52] D. H. E. Dubin, "Theory of structural phase transitions in a trapped Coulomb crystal," *Phys. Rev. Lett.*, vol. 71, pp. 2753–2756, Oct 1993.

[53] A. Steane, "The ion trap quantum information processor," *Applied Physics B*, vol. 64, pp. 623–643, Jun 1997.

[54] Q. A. Turchette, Kielpinski, B. E. King, D. Leibfried, D. M. Meekhof, C. J. Myatt, M. A. Rowe, C. A. Sackett, C. S. Wood, W. M. Itano, C. Monroe, and D. J. Wineland, "Heating of trapped ions from the quantum ground state," *Phys. Rev. A*, vol. 61, p. 063418, May 2000.

[55] C. F. Roos, T. Monz, K. Kim, M. Riebe, H. Häffner, D. F. V. James, and R. Blatt, "Nonlinear coupling of continuous variables at the single quantum level," *Phys. Rev. A*, vol. 77, p. 040302(R), Apr 2008.

[56] E. Magesan, J. M. Gambetta, and J. Emerson, "Characterizing quantum gates via randomized benchmarking," *Phys. Rev. A*, vol. 85, p. 042311, Apr 2012.

[57] Y. R. Sanders, J. J. Wallman, and B. C. Sanders, "Bounding quantum gate error rate based on reported average fidelity," *New Journal of Physics*, vol. 18, no. 1, p. 012002, 2016.

[58] M. P. da Silva, "matlab-diamond-norm." https://github.com/BBN-Q/matlab-diamond-norm, 2015.

[59] D. F. Griffiths and D. J. Higham, *Numerical methods for ordinary differential equations: initial value problems*. Springer, 2010.

[60] H. Landa, M. Drewsen, B. Reznik, and A. Retzker, "Classical and quantum modes of coupled Mathieu equations," *Journal of Physics A: Mathematical and Theoretical*, vol. 45, no. 45, p. 455305, 2012.

[61] L. N. Trefethen and D. Bau III, *Numerical linear algebra*. SIAM, 1997.

[62] J. Hoffnagle and R. G. Brewer, "Chaotic transients of two particles in a Paul trap: Interpretation as a boundary crisis," *Phys. Rev. A*, vol. 50, pp. 4157–4169, Nov 1994.

[63] R. Blümel, J. Chen, E. Peik, W. Quint, W. Schleich, Y. Shen, and H. Walther, "Phase transitions of stored laser-cooled ions," *Nature*, vol. 334, p. 309, 1988.

[64] R. Brewer, J. Hoffnagle, R. DeVoe, L. Reyna, and W. Henshaw, "Collision-induced two-ion chaos," *Nature*, vol. 344, p. 305, 1990.

[65] J. W. Emmert, M. Moore, and R. Blümel, "Prediction of a deterministic melting transition of two-ion crystals in a paul trap," *Phys. Rev. A*, vol. 48, pp. R1757–R1760, Sep 1993.

[66] H. Walther, "Phase transitions of stored laser-cooled ions," vol. 31 of *Advances In Atomic, Molecular, and Optical Physics*, pp. 137 – 182, Academic Press, 1993.

[67] V. L. Ryjkov, X. Zhao, and H. A. Schuessler, "Simulations of the rf heating rates in a linear quadrupole ion trap," *Phys. Rev. A*, vol. 71, p. 033414, Mar 2005.

[68] I. M. Buluta, M. Kitaoka, S. Georgescu, and S. Hasegawa, "Investigation of planar Coulomb crystals for quantum simulation and computation," *Phys. Rev. A*, vol. 77, p. 062320, Jun 2008.

[69] J. P. Schiffer, M. Drewsen, J. S. Hangst, and L. Hornekær, "Temperature, ordering, and equilibrium with time-dependent confining forces," *Proceedings of the National Academy of Sciences*, vol. 97, no. 20, pp. 10697–10700, 2000.

[70] A. W. Vogt, "Nonlinear resonances and the melting of Wigner crystals in a Paul trap," *Phys. Rev. A*, vol. 49, pp. R657–R660, Feb 1994.

[71] P. Dawson and N. Whetten, "Non-linear resonances in quadrupole mass spectrometers due to imperfect fields i. the quadrupole ion trap," *International Journal of Mass Spectrometry and Ion Physics*, vol. 2, no. 1, pp. 45 – 59, 1969.

[72] Y. Wang, J. Franzen, and K. Wanczek, "The non-linear resonance ion trap. part 2. a general theoretical analysis," *International Journal of Mass Spectrometry and Ion Processes*, vol. 124, no. 2, pp. 125 – 144, 1993.

[73] R. Alheit, C. Hennig, R. Morgenstern, F. Vedel, and G. Werth, "Observation of instabilities in a Paul trap with higher-order anharmonicities," *Applied Physics B*, vol. 61, pp. 277–283, Sep 1995.

[74] R. Alheit, S. Kleineidam, F. Vedel, M. Vedel, and G. Werth, "Higher order non-linear resonances in a Paul trap," *International Journal of Mass Spectrometry and Ion Processes*, vol. 154, no. 3, pp. 155 – 169, 1996.

[75] K. T. Alligood, T. D. Sauer, and J. A. Yorke, *Chaos: An Introduction to Dynamical Systems*. Springer, 1996.

[76] R. W. Hockney and J. W. Eastwood, *Computer simulation using particles*. Institute of Physics Publishing, 1988.

[77] B. Kehlet and A. Logg, "A posteriori error analysis of round-off errors in the numerical solution of ordinary differential equations," *Numerical Algorithms*, vol. 76, pp. 191–210, Sep 2017.

[78] T. Feagin, "High-order explicit Runge-Kutta methods using W-symmetry," *Neural, Parallel and Scientific Computations*, vol. 20, no. 3-4, pp. 437–458, 2012.

[79] T. Feagin, "High-order explicit Runge-Kutta methods." http://sce.uhcl.edu/rungekutta/, 2009. [Online; accessed 11-November-2017].

[80] J. Thijssen, *Computational Physics*. Cambridge University Press, 2 ed., 2007.

[81] T. Granlund *et al.*, "The GNU multiple precision arithmetic library." https://gmplib.org, 2016.

[82] G. Pagano, P. W. Hess, H. B. Kaplan, W. L. Tan, P. Richerme, P. Becker, A. Kyprianidis, J. Zhang, E. Birckelbaw, M. R. Hernandez, Y. Wu, and C. Monroe, "Cryogenic trapped-ion system for large scale quantum simulation," *Quantum Science and Technology*, vol. 4, no. 1, p. 014004, 2019.

[83] A. J. Daley, "Quantum trajectories and open many-body quantum systems," *Advances in Physics*, vol. 63, no. 2, pp. 77–149, 2014.

[84] J. P. Schiffer, "Order in confined ions," *Journal of Physics B: Atomic, Molecular and Optical Physics*, vol. 36, no. 3, p. 511, 2003.

[85] S. G. Brush, H. L. Sahlin, and E. Teller, "Monte Carlo study of a one-component plasma. i," *The Journal of Chemical Physics*, vol. 45, no. 6, pp. 2102–2118, 1966.

[86] E. L. Pollock and J. P. Hansen, "Statistical mechanics of dense ionized matter. ii. equilibrium properties and melting transition of the crystallized one-component plasma," *Phys. Rev. A*, vol. 8, pp. 3110–3122, Dec 1973.

[87] K. A. Landsman, Y. Wu, P. H. Leung, D. Zhu, N. M. Linke, K. R. Brown, L. Duan, and C. Monroe, "Two-qubit entangling gates within arbitrarily long chains of trapped ions." unpublished.

[88] D. Aharonov, A. Kitaev, and N. Nisan, "Quantum Circuits with Mixed States," in *Proceedings of the Thirtieth Annual ACM Symposium on Theory of Computing*, STOC '98, (New York, NY, USA), pp. 20–30, ACM, 1998.

[89] C. Shen and L.-M. Duan, "High-fidelity quantum gates for trapped ions under micromotion," *Phys. Rev. A*, vol. 90, p. 022332, Aug 2014.

[90] G. B. Arfken, H.-J. Weber, and F. E. Harris, *Mathematical methods for physicists: a comprehensive guide*. Elsevier, 7th ed., 2013.

[91] M. Condon, A. Deaño, and A. Iserles, "On highly oscillatory problems arising in electronic engineering," *ESAIM: M2AN*, vol. 43, no. 4, pp. 785–804, 2009.

[92] E. Ising, "Beitrag zur theorie des ferromagnetismus," *Zeitschrift für Physik*, vol. 31, no. 1, pp. 253–258, 1925.

[93] L. Onsager, "Crystal statistics. i. a two-dimensional model with an order-disorder transition," *Phys. Rev.*, vol. 65, pp. 117–149, Feb 1944.

[94] C. N. Yang, "The spontaneous magnetization of a two-dimensional Ising model," *Phys. Rev.*, vol. 85, pp. 808–816, Mar 1952.

[95] A. M. Ferrenberg and D. P. Landau, "Critical behavior of the three-dimensional Ising model: A high-resolution Monte Carlo study," *Phys. Rev. B*, vol. 44, pp. 5081–5091, Sep 1991.

[96] R. H. Swendsen and J.-S. Wang, "Nonuniversal critical dynamics in Monte Carlo simulations," *Phys. Rev. Lett.*, vol. 58, pp. 86–88, Jan 1987.

[97] U. Wolff, "Collective Monte Carlo updating for spin systems," *Phys. Rev. Lett.*, vol. 62, pp. 361–364, Jan 1989.

[98] S. Sachdev, *Quantum phase transitions*. Cambridge University Press, 2nd ed., 2011.

[99] K. Binder and A. P. Young, "Spin glasses: Experimental facts, theoretical concepts, and open questions," *Rev. Mod. Phys.*, vol. 58, pp. 801–976, Oct 1986.

[100] I. M. Georgescu, S. Ashhab, and F. Nori, "Quantum simulation," *Rev. Mod. Phys.*, vol. 86, pp. 153–185, Mar 2014.

[101] K. Kim, M.-S. Chang, R. Islam, S. Korenblit, L.-M. Duan, and C. Monroe, "Entanglement and tunable spin-spin couplings between trapped ions using multiple transverse modes," *Phys. Rev. Lett.*, vol. 103, p. 120502, Sep 2009.

[102] K. Kim, M.-S. Chang, S. Korenblit, R. Islam, E. E. Edwards, J. K. Freericks, G.-D. Lin, L.-M. Duan, and C. Monroe, "Quantum simulation of frustrated Ising spins with trapped ions," *Nature*, vol. 465, no. 7298, p. 590, 2010.

[103] B. P. Lanyon, C. Hempel, D. Nigg, M. Müller, R. Gerritsma, F. Zähringer, P. Schindler, J. T. Barreiro, M. Rambach, G. Kirchmair, M. Hennrich, P. Zoller, R. Blatt, and C. F. Roos, "Universal digital quantum simulation with trapped ions," *Science*, vol. 334, no. 6052, pp. 57–61, 2011.

[104] R. Islam, C. Senko, W. C. Campbell, S. Korenblit, J. Smith, A. Lee, E. E. Edwards, C.-C. J. Wang, J. K. Freericks, and C. Monroe, "Emergence and frustration of magnetism with variable-range interactions in a quantum simulator," *Science*, vol. 340, no. 6132, pp. 583–587, 2013.

[105] S. Korenblit, D. Kafri, W. C. Campbell, R. Islam, E. E. Edwards, Z.-X. Gong, G.-D. Lin, L.-M. Duan, J. Kim, K. Kim, and C. Monroe, "Quantum simulation of spin models on an arbitrary lattice with trapped ions," *New Journal of Physics*, vol. 14, no. 9, p. 095024, 2012.

[106] C. Figgatt, A. Ostrander, N. Linke, K. Landsman, D. Zhu, D. Maslov, and C. Monroe, "Parallel entangling operations on a universal ion trap quantum computer," *arXiv preprint arXiv:1810.11948*, 2018.

[107] M. Suzuki, "General theory of fractal path integrals with applications to many-body theories and statistical physics," *Journal of Mathematical Physics*, vol. 32, no. 2, pp. 400–407, 1991.

[108] N. Wiebe, D. Berry, P. Høyer, and B. C. Sanders, "Higher order decompositions of ordered operator exponentials," *Journal of Physics A: Mathematical and Theoretical*, vol. 43, no. 6, p. 065203, 2010.